High Resolution Near-Infrared Imaging Observations of the Galactic Centre

vorgelegt von Rainer Schödel

München, den 9.Februar 2004

Tag der mündlichen Prüfung: 3. Juni 2004

1.Gutachter: Prof. Dr. Reinhard Genzel
2.Gutachter: Prof. Dr. Ralf Bender

Stellar Orbits around SgrA*
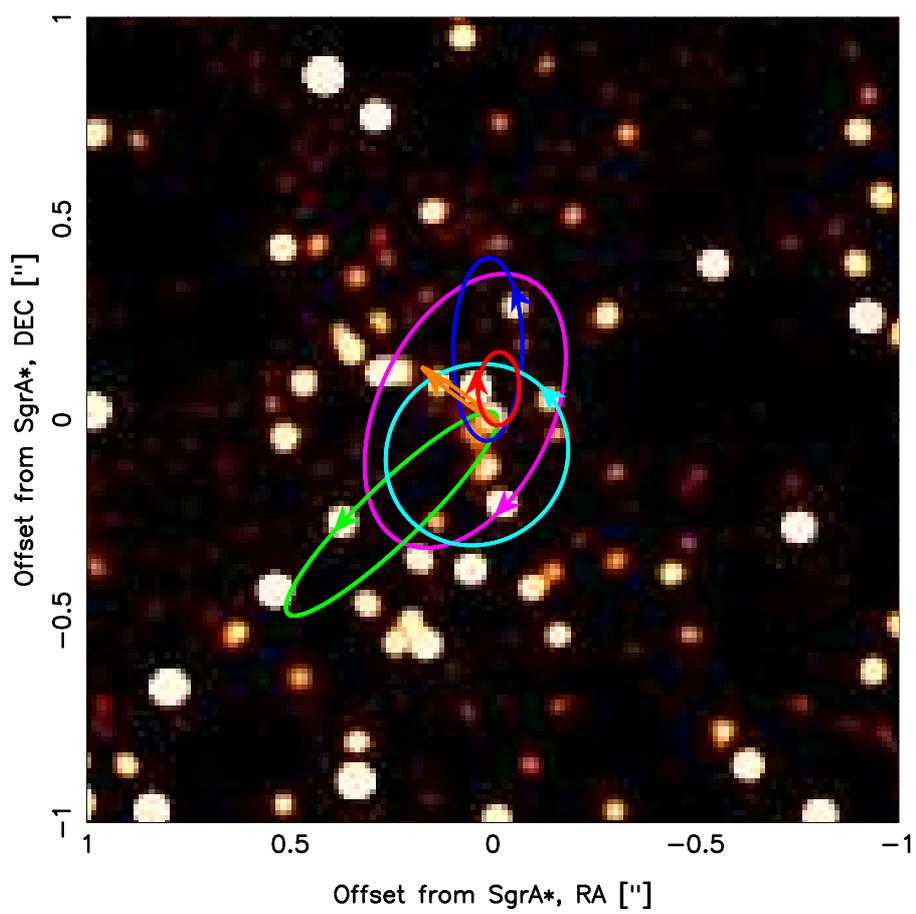
Figure on cover page: Orbits of stars around Sagittarius A*. *Lucy-Richardson deconvolved and beam-restored high-resolution (FWHM$\sim$ 60 milliarcseconds) near-infrared (2.2μm) image of the central $1'' \times 1''$ of the nuclear stellar cluster around the supermassive black hole Sgr A*. The image was obtained with CONICA/NAOS at the ESO VLT in June 2003. On this image Sgr A* can be seen in its flaring state as a point source at the origin of the coordinate system. The Keplerian orbits of six stars, as they were determined in this thesis, are overplotted onto the image. Arrows indicate the locations of the respective stars and their direction of motion.*

Zusammenfassung

Ziel der vorliegenden Doktorarbeit war es, neue Erkenntnisse über die Struktur, Zusammensetzung und Dynamik des zentralen Sternhaufens unserer Milchstraße zu gewinnen. Im Mittelpunkt unserer Analysen stand dabei vor allem die Natur der Konzentration einiger Millionen Sonnenmassen dunkler Materie im Zentrum dieses Haufens, bei welcher es sich vermutlich um ein supermassives Schwarzes Loch handelt. Schon seit Jahrzehnten wurde vermutet, dass die kompakte, nicht-thermische Radioquelle Sagittarius A* (Sgr A*), welche 1974 entdeckt wurde, mit einem solchen Objekt assoziiert ist. In großen Teilen basiert diese Arbeit auf Beobachtungen des galaktischen Zentrums mit der neuartigen Nahinfrarotkamera CONICA und dem dazugehörigen System für adaptive Optik, NAOS, am Very Large Telescope der Europäischen Südsternwarte. Dieses kombinierte System wurde Ende 2001/Anfang 2002 in Betrieb genommen und bietet ideale Voraussetzungen für tiefe, hochaufgelöste Nahinfrarot-Beobachtungen des galaktischen Zentrums.

Ein grundliegendes Problem, welches es zu lösen galt, war die Astrometrie der Aufnahmen des Sternfeldes im galaktischen Zentrum. Ein akkurates astrometrisches System ist eine essentielle Voraussetzung dafür, Sgr A* auf Infrarotbildern zu identifizieren und die relativen Positionen und Bewegungen der Sterne in seiner Umgebung zu messen. Mit Hilfe von SiO Maser Sternen, deren Position durch Radiointerferometrie zu < 1 Millibogensekunde bestimmt werden kann, gelang es uns, die Position der nicht-thermischen Radioquelle Sagittarius A* (Sgr A*), welche mit dem vermuteten schwarzen Loch assoziiert ist, relativ zu den Sternen in seiner Umgebung mit einer Genauigkeit von < 10 mas zu bestimmen.

Durch Sternzählungen in tiefen, hochauflösenden Bildern konnten wir zeigen, dass die Sterndichte zu Sgr A* hin mit einem Potenzgesetz ansteigt, dass der Sternhaufen also einen sogenannten *Cusp* in einem Radius von ca. $1''$ oder 40 mpc um das vermutete schwarze Loch aufzeigt. In einer Distanz < 4 mpc von Sgr A* steigt die Massendichte des Haufens auf über 10^8 M$_\odot$ an. Die Sternpopulation im Cusp zeigt einen Mangel an Riesensternen und an Sternen auf dem horizontalen Ast relativ zum umgebenden Haufen. Hierfür könnten Sternkollisionen und/oder Massensegregation verantwortlich sein.

Die Geschwindigkeitsdispersion der Sterne im Cusp, σ_v, lässt auf eine dunkle, zentrale Masse von $3 - 4 \times 10^6$ M$_\odot$ schließen. Überraschenderweise fanden wir Anzeichen für eine radiale Anisotropie von σ_v. Dies widerspricht unserer Erwartung, dass der zentrale Haufen vollständig relaxiert sein sollte und könnte einen Hinweis auf die Entstehung des Cusps geben, bzw. auf den Ursprung der anscheinend sehr jungen Sterne in der Umgebung von Sgr A*, deren Präsenz gegenwärtig durch kein Modell zufrieden stellend erklärt werden kann.

Durch die lange Zeitbasis von mehr als zehn Jahren, für welche wir die Positionen der Sterne in der Nachbarschaft von Sgr A* messen konnten, gelang es uns, für sechs Sterne individuelle Kepler-Orbits um Sgr A* zu bestimmen. Der Stern S2 weist den am genauesten bestimmten Orbit auf und durchlief das Perizentrum seiner Bahn um Sgr A* im Frühjahr 2002. Dadurch konnten wir zeigen, dass im Zentrum der Milchstraße eine Masse von 3.6×10^6 M$_\odot$ in einem Volumen mit einem Radius von lediglich 0.55 mpc konzentriert ist. Durch diese hohe gemessene Massendichte konnten wir das Neutrinoball-Modell und das Modell eines dichten Haufens aus dunklen astrophysikalischen Objekten als Alternativen zum Schwarzen Loch weitgehend ausschließen. Der Orbit von S2 erlaubte es uns auch, zum ersten Mal die Distanz zum galaktischen Zentrum geometrisch zu bestimmen: 7.9 ± 0.4 kpc in Übereinstimmung mit früheren Schätzungen.

Schließlich konnten wir erstmalig Nahinfrarot-Emission von Sgr A* entdecken. Die Variabilität der Quelle deutet auf einen Ursprung der Strahlung innerhalb von 10 Schwarzschild-Radien um das Schwarze Loch hin. Die Quasiperiodizität, welche wir in zwei Strahlungsausbrüchen fanden, erlaubte es uns, unter der Annahme, dass die Strahlung von Materie in der Nähe des letzten stabilen Orbits eines rotierenden Schwarzen Loches stammt, den Spin des Schwarzen Loches abzuschätzen.

Contents

Chapter 1

Introduction

The discovery of quasars in the second half of the 20th century and subsequent detailed research on these extraordinary objects soon led to the insight that these sources are the objects with the highest average energy output in the universe. Moreover, it was found that quasars produce their intense radiation on very small scales, i.e. are extremely compact sources. It was found that all observations can be explained best by the assumption that quasars are supermassive black holes of up to several billion solar masses located at the centre of galaxies that are accreting matter at a rate comparable to $1 \mathrm{M}_\odot \mathrm{yr}^{-1}$ from their surroundings. While most quasars can be found at redshifts of roughly 2-3, they are much rarer in the local, i.e. present-time, universe.

If supermassive black holes can be observed in the early days of the universe, they must still be present in the present-day universe. In fact, active galactic nuclei (AGN), such as in Seyfert galaxies, observed in the local universe, are considered scaled-down versions of quasars. If one assumes that the reason for the scarcity of quasars in the local universe is that they ran out of fuel, it should be possible to observe these enormous concentrations of dark matter at galactic nuclei via their influence on the dynamics of the surrounding stellar clusters or galactic bulges. Indeed, high-resolution spectroscopic observations with the Hubble Space Telescope and ground based telescopes as well as radio interferometric observations of maser disks have provided considerable evidence for the existence of supermassive black holes at the centre of quiet galactic nuclei, with $30 - 40$ known candidates up to date (Kormendy, 2001, 2003). In the cases of our own galaxy, of M31, and of NGC 4258 the measurements exclude clusters of dark stellar remnants as explanations for the observed dark mass concentrations (Kormendy, 2003).

The centre of the Milky Way is about 100 times closer to Earth than the next major galaxy, M31, and 1000 times closer than the next AGN. Therefore, we can observe the phenomena at the centre of our home galaxy at a level of detail that can never be reached in the case of external galaxies. This makes the Milky Way an ideal candidate for testing the standard paradigm that supermassive black holes reside at the centre of most, if not all, galaxies.

The solar system is located in the galactic plane at a distance of about 8 kpc from the Galactic Centre (GC) (Reid, 1993). Dust clouds in the galactic disk therefore cause an extinction of about 30 magnitudes toward the GC at visual wavelengths. Hence, the GC can only be observed in the radio, infrared and X-ray regimes. Lynden-Bell & Rees (1971) first suggested that the Milky Way might contain a supermassive black hole in its centre. When Balick & Brown (1974) detected the compact non-thermal radio source Sagittarius A* (Sgr A*, naming by Brown, 1982) in the GC, this object soon became the primary suspect for being the manifestation of such a black hole. Subsequent radio interferometric observations showed that the source is very compact, i.e. less than 1 AU in diameter (Rogers et al., 1994; Krichbaum et al., 1998; Lo et al., 1998; Doeleman et al., 2001). Backer & Sramek (1999) and Reid et al. (1999) inferred from multi-epoch observations that Sgr A* has a velocity projected on the

sky of < 20 km/s. Compared to the velocity dispersion in the nuclear stellar cluster of several hundred km/s this means that Sgr A* must have a mass of at least several thousand solar masses.

The standard technique in the quest for testing the black hole hypothesis is measuring the gravitational potential at ever shorter distances to the black hole candidate Sgr A*. The amount of dark mass that is enclosed in a given volume can be determined from the dynamics of gas and stars in the galactic nucleus. First dynamical observations of the enclosed mass in the central parsec suggested the presence of a point-like object of $\sim 3 \times 10^6$ M$_\odot$ at the heart of the Milky Way (see Genzel & Townes, 1987). However, these first estimates still depended sensitively on the motion of ionised gas streamers (Serabyn & Lacy, 1985; Serabyn, 1988), which can be subject to forces other than gravity, such as magnetic fields or stellar winds. Stars, however, would be the ideal test particles for measuring strong, large-scale gravitational fields.

For this undertaking, it was necessary to be able to measure the proper motion velocities of the stars in the GC cluster, i.e. their velocities as seen projected on the plane of the sky. However, this required the capability of measuring their positions with a precision of a few milli-arc-seconds. This became possible with the availability of large near-infrared (NIR) detector arrays in combination with high resolution NIR imaging techniques at the beginning of the 1990's, which opened the way for imaging observations of the nuclear cluster of the Milky Way at the diffraction limit of 4–10 m class telescopes.

High-resolution imaging techniques at NIR wavelengths involve basically two methods, *speckle imaging* and *adaptive optics*. Atmospheric turbulence causes a deterioration of astronomic images so that even under excellent conditions, the achievable resolution of long exposures is not better than about $0.5''$. The *speckle imaging* technique takes advantage of the fact that information at the diffraction limit of large telescopes is conserved if one chooses a short enough integration time, of the order 0.1 s. Series of short speckle exposures can be used for a subsequent restoration of a diffraction limited image with the help of a computer. As for *adaptive optics*, briefly explained, this technique allows measuring and correcting the major atmospheric image distortions in real time. A so-called wavefront sensor (WFS) in combination with a real-time computer serves to analyse the light of a bright star, that is taken as a reference point source, and sends a signal to a de-formable mirror that corrects the wavefronts of the incoming light before it is registered by the detector. The biggest advantage of the AO technique over speckle techniques is that it does not require short integration times of just fractions of a second. Hence, integration times of several seconds up to hours are possible. This significantly enhances the sensitivity of the observations because they are not limited any longer by the read-out noise of the detector.

The NIR speckle camera SHARP (Hofmann et al., 1995), built at the Max-Planck-Institut für extraterrestrische Physik, was the first such instrument that was dedicated to GC observations. It was used at the ESO 3.5 m NTT telescope in La Silla, Chile, and provided the first diffraction limited images of the central parsec of the GC (Eckart et al., 1992). This technology opened the way for measuring stellar proper motions near Sgr A*, the suspected supermassive black hole. Several epochs of observations accumulated indeed strong evidence that the gravitational potential in the central 0.5 pc of the Milky Way was dominated by a point mass of $2 - 3$ million solar masses (Eckart & Genzel, 1996; Genzel et al., 1997, 2000). In 1995, a similar experiment was started by a group at the University of California Los Angeles (UCLA) with the 10 m Keck telescope, using also speckle imaging and later also adaptive optics (AO) techniques. They confirmed the results that were found by the MPE group and also detected the first evidence for accelerations of stars near the suspected supermassive black hole (Ghez et al., 1998, 2000).

At the end of 2001, the ESO VLT unit telescope 4 (Yepun) was equipped with the NIR camera CONICA and the AO system NAOS (Lenzen et al., 1998; Rousset et al., 1998). The combined instruments ("NACO") serve to obtain diffraction limited NIR images on the 8m class VLT telescope. While conventional AO systems rely on guiding stars that are bright at

visible wavelengths for the wavefront sensing, NAOS has the unique feature of an infrared wavefront sensor (IWFS). This means that it can alternatively lock the AO on sources that are bright in the near-infrared regime if no visibly bright star is near the observed target. In the case of the GC, the nearest visible guiding star is more than $30''$ away from the target and rather faint (~ 14 mag). This allows only moderate image corrections under good atmospheric conditions. However, there is a supergiant, IRS 7, with a magnitude of ~ 6.5 in the K band, located less than $6''$ from Sgr A*. IRS 7 is an ideal reference source for NAOS' infrared wavefront sensor. Combined with the location of the VLT in the Chilean Atacama, where the GC passes close to zenith and allows long observations at low airmasses, NACO is the ideal new generation instrument for observations of the nuclear star cluster of the Milky Way.

The work presented here is based largely on the observational data obtained with the new NACO instrument, which have brought significant progress to our knowledge of the nuclear stellar cluster and the nature of Sgr A*. They allowed an examination of the overall structure of the stellar cluster in the central parsec. In combination with a thorough re-analysis of older speckle imaging data, we present observations and analyses on the stellar dynamics near Sgr A*, which provide new and compelling evidence that this source is indeed a supermassive black hole and allow, for the first time, a direct, geometrical determination of the distance to the GC. We conclude with the first observations of a near-infrared counterpart of Sgr A*, strong evidence for accretion and emission processes near the black hole.

Chapter 2

The Central Parsec of the Milky Way

Our home galaxy, the Milky Way, appears to be an ordinary barred spiral galaxy of type Sbc (Kormendy, 2001). The centre of the Milky Way is located at 8.0 kpc from the solar system (Reid, 1993), a value that will be assumed throughout this paper if not explicitly stated otherwise. Due to its proximity, we can study the nucleus of the GC as an exemplary model for other galaxies of similar type. In this chapter, we will briefly review the phenomena at and the properties of the central few light years of the Milky Way as well as of its most peculiar object, the compact radio source and putative supermassive black hole Sagittarius A*. For the corresponding scientific issues we will cite some exemplary works. We will tackle many topics in this chapter, but cannot give a complete review within the framework of this chapter. More detailed information can be found, for example, in the reviews by Genzel, Hollenbach, & Townes (1994); Morris & Serabyn (1996); Genzel (2001) and Melia & Falcke (2001).

2.1   The Nuclear Star Cluster

High-resolution NIR speckle imaging observations at the NTT and Keck telescopes allowed to derive the distribution of stars in the GC that are brighter than $15 - 16$ in the K-band. This included all red and most blue super giants, all red giants, and all main sequence stars earlier than about B2. Although several hundreds of stars have been sampled in the central few arcseconds of the GC stellar cluster in this way, one has to keep in mind that all interpretations derived from these observations are still based on just around 0.1% of the total stellar content of the cluster.

On scales ≥ 0.5 pc, the stars at the centre of the Milky Way are distributed according to a near-isothermal cluster. Surface number density and surface brightness measurements indicate that the stellar volume density decreases with a power law of $\propto R^{-2}$ from projected radii of $100''$ down to about $10''$ (Catchpole, Whitelock & Glass, 1990; Genzel et al., 1996, 2003). Scoville et al. (2003), however, find a much shallower radial density distribution ($\propto R^{-0.5}$). The reason for the differences are still unclear. Inside $\sim 10''$ ($1''$ corresponds to 0.039 pc at the distance of the GC) the number density of stars brighter than K≥ 15 flattens, indicating a core radius of the late type stars of 0.34 ± 0.2 pc (Genzel et al., 1996). Analyses of stellar number counts from speckle imaging indicated that the cluster immediately surrounding Sgr A* might have a smaller core radius of about 0.08 pc (e.g. Genzel et al., 2000) thus providing clues to the existence of a stellar cusp around Sgr A* in the central few arcseconds (Alexander, 1999). Stellar number counts appear to be a more rigorous way of deriving the structure of the central cluster than analyses of the surface brightness distribution because the luminosity in the inner parsec of the GC is dominated by a few dozen bright sources.

13
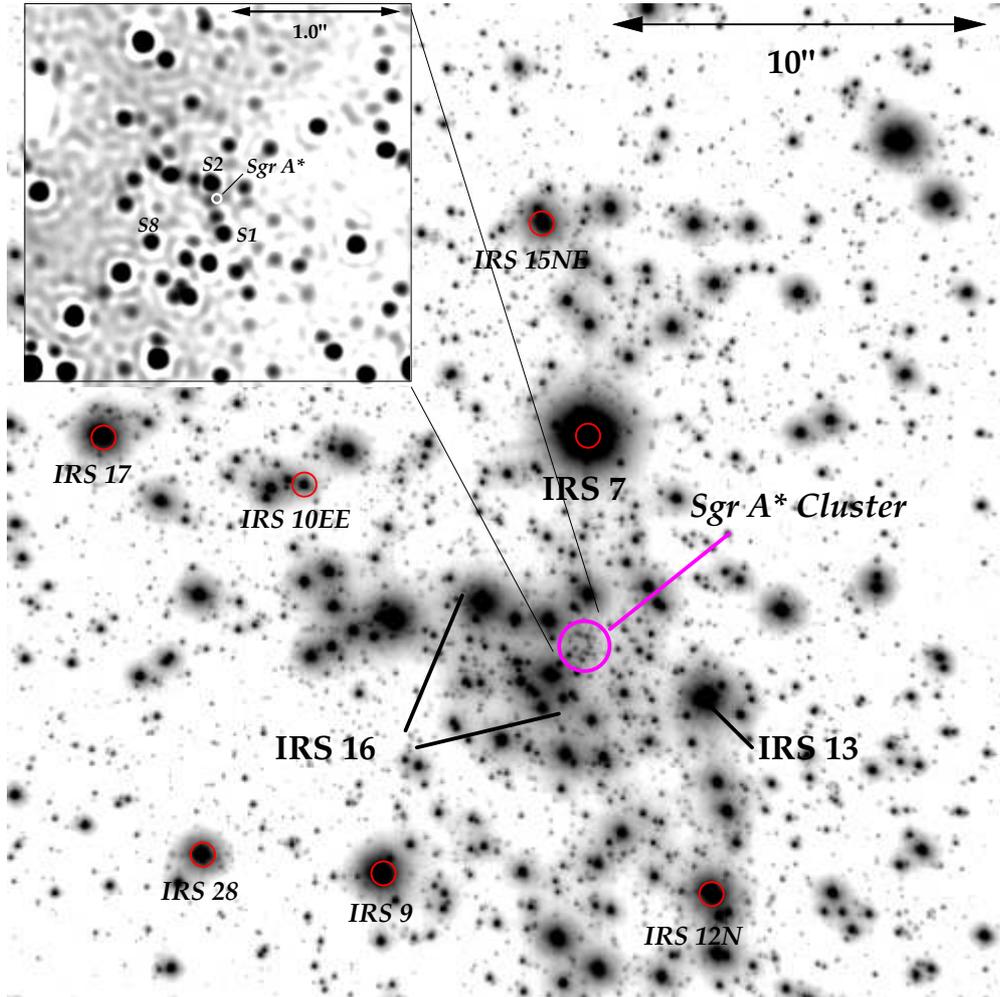
Figure 2.1: **K-band image of the GC stellar cluster.** *This K-band (2.2μm) image was obtained on May 10, 2003, with CONICA/NAOS at the VLT and covers the central $\sim 30 \times 30''$ ($\sim 1.2 \times 1.2$ pc) of the GC. The brightest source near the middle of the image is the late-type supergiant IRS 7 (K$\sim$ 6.5), which was used to lock the AO of NAOS. The IRS 16 and IRS 13 clusters of young, blue HI/HeI emission line stars are marked. Stars marked by circles are SiO maser stars that were used to establish the link between the NIR and the radio astrometry (see chapter 5). A circle in the middle denotes the location of the cluster of stars in the immediate vicinity of Sgr A*, the so called "Sgr A* cluster". The inset in the left upper corner shows a region of $\sim 2 \times 2''$ ($\sim 0.08 \times 0.08$ pc) centred on this cluster. The image was obtained after applying a Lucy-Richardson deconvolution and subsequent restoration to a beam FWHM of $\sim$ 60 mas. The location of Sgr A* is indicated by a white circle. Sgr A* cannot be unambiguously identified on this image. The moderately bright (K$\sim$ 14 − 15) sources S1, S2, and S8 near Sgr A* are labeled with their names. These sources and some sources of similar brightness near Sgr A* are potential O/B type stars.*

This results in a skewed light distribution centered about $2''$ east of Sgr A*. Hence, with the earlier seeing-limited observations of the GC stellar cluster this was interpreted (erroneously)
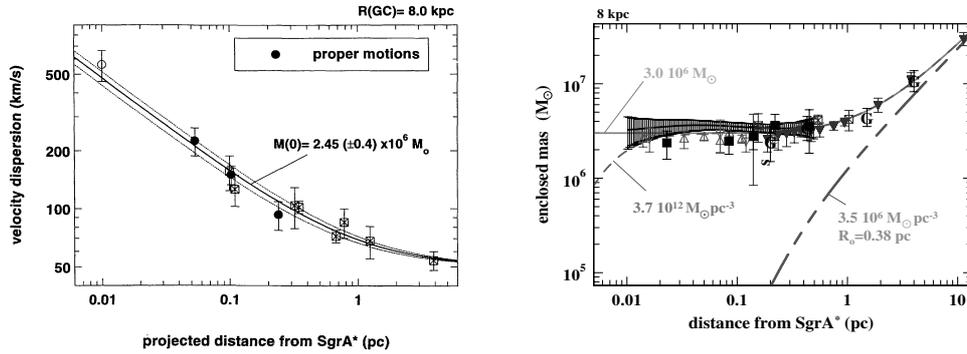
Figure 2.2: **Dynamics of the nuclear stellar cluster of the Milky Way.** *Left hand plot: Velocity dispersion plotted against the distance from Sgr A* as inferred by the evaluation of stellar proper motions in the nuclear cluster of the Milky Way. The Figure was taken from Eckart & Genzel (1997). For details, see their Figure 4. In the inner parsec the velocity dispersion rises proportional $R^{-1/2}$, where R is the distance to Sgr A*, as expected in the potential of a point mass. Right hand plot: Enclosed mass against distance from Sgr A* as inferred by gas and stellar dynamics. The various data points and error bars refer to different data sets and statistical methods. For details on this Figure, see Genzel et al. (2000), Figure 17. The long dash-short dash curve shows the mass of the near-isothermal, visible stellar cluster with a density of $3.5 \times 10^6\,M_\odot pc^{-3}$ and a core radius of 0.38 pc, assuming a law of the form $\rho(r) = \rho_0[1 + (r/r_0)^2]^{-\alpha/2}$ ($\alpha \approx 2$ for an isothermal cluster). The straight line shows a model of this stellar cluster plus a point mass of $3.0 \times 10^6\,M_\odot$. The dashed line is a model of the cluster plus a hypothetical, very dense cluster of central density $3.7 \times 10^{12}\,M_\odot pc^{-3}$ and core radius 0.0058 pc. A plummer model has been assumed for this cluster ($\rho(r)$ defined as above, but with $\alpha = 5$).*

as evidence that Sgr A* could not be a supermassive black hole (Allen & Sanders, 1986).

The most important components of the GC stellar cluster are indicated in Figure 2.1 and are briefly described as follows:

- The brightest source in the central parsec is the red supergiant IRS 7, (class MI, $T_{eff} \approx$ 3500K) about $6''$ north of Sgr A*. It is a long period variable with an apparent average magnitude in K-band of ~ 6.5 (Blum, Sellgren, & DePoy, 1996; Ott et al., 1999).

- The luminosity in the central few arcseconds is dominated by about two dozen hot, massive, bright (K$\sim 9 - 12$), blue stars, which are characterized by strong HI/HeI emission lines. Ott et al. (1999) showed that one of the HeI stars, IRS 16 SW, is most probably an eclipsing binary (period of 9.72 days) with a mass of $\leq 100\,M_\odot$. The HeI stars have surface temperatures of $20000 - 30000$ K and are sources of intense stellar winds. They might be witnesses of a star formation episode between 3 and 7 million years ago (Eckart et al., 1995; Allen, Hyland, & Hillier, 1990; Krabbe et al., 1995; Najarro et al., 1994, 1997). They are mainly concentrated in the IRS 16 and IRS 13 clusters (see Figure 2.1). They are not dynamically relaxed and display a coherent rotation pattern counter to the overall galactic rotation. This could be interpreted as a remnant of the angular momentum of the original gas cloud from which these stars formed (Genzel et al., 2000).

- There is a second component dominating NIR images of the GC stellar cluster. That

is a group of intermediate bright (K∼ 10 − 13), late-type stars. These stars have been identified as stars at the top of the asymptotic giant branch (AGB), which give testimony of another star formation episode about 100 million years ago. The strength of the CO absorption feature decreases in the central few arcseconds around Sgr A*. This may be due to an actual lack of late-type giants there because their envelopes are destroyed by collisions in the dense stellar cluster (Sellgren et al., 1990; Genzel et al., 1996; Alexander, 1999). Alternatively, the presence of luminous, blue stars (the "HeI-stars") in the central few arcseconds might dilute the CO absorption feature (Sellgren et al., 1990; Eckart et al., 1995; Krabbe et al., 1995; Genzel et al., 1996; Haller et al., 1996; Blum, Sellgren, & DePoy, 1996).

- A specific concentration of K $\sim 14 - 15$ stars can be found within about $1''$ of Sgr A* (see small inset in Figure 2.1). Several of these stars exhibit proper motion velocities (i.e. velocities projected on the sky) in excess of $1000 \, \mathrm{kms}^{-1}$ and even show signs of accelerated motion (Eckart & Genzel, 1996, 1997; Ghez et al., 1998, 2000; Eckart et al., 2002). Speckle imaging and adaptive optics spectroscopic observations showed that the so-called "S"-sources in the Sgr A* cluster are blue stars, possibly O or B main sequence stars (Genzel et al., 1997; Eckart, Ott, & Genzel, 1999; Figer et al., 2000; Gezari et al., 2002; Ghez et al., 2003).

- There is the possibility that further O/B main sequence stars can be found among the stars of K $\sim 14 - 15$ at greater distances from Sgr A*. However, because of the strong and highly variable extinction in the central parsec, broad band NIR colors are not sufficient for determining the nature of these stars. So far, no unambiguous evidence has been found of additional O/B type main sequence stars in the central parsec. Most probably, stars of apparent K-magnitudes > 13 in the GC cluster are late type stars, like solar mass M giants or intermediate mass K giants.

- A number of very cool objects with red, featureless spectra can be found mostly associated with the mini-spiral, such as IRS 21, IRS 1W, or IRS 10W. These sources are resolved in high-resolution imaging observations, i.e. they are not point sources (Krabbe et al., 1995; Ott et al., 1999; Tanner et al., 2002). They have been interpreted as deeply dust enshrouded young stars, but more recent observations suggest that they might be rather massive stars experiencing rapid mass loss that plow through the interstellar medium (Tanner et al., 2002), thereby creating bow shocks and appearing as extended sources.

Since stars are not subject to large scale forces produced by interstellar magnetic fields or winds, but only to gravity, they are ideal tracer particles for determining the shape of the gravitational potential in the GC. High-resolution NIR speckle imaging observations, that allow measuring stellar positions to within a few milli-arcseconds, have opened the way for measuring stellar proper motion velocities and accelerations in the nuclear cluster (Eckart & Genzel, 1996, 1997; Ghez et al., 1998; Genzel et al., 2000; Ghez et al., 2000). In agreement with spectroscopic observations of line-of-sight velocities (e.g. Sellgren et al., 1990; Krabbe et al., 1995; Genzel et al., 1996), these experiments showed that the velocity dispersion increases with distance R to Sgr A* as $R^{-1/2}$, such as it is expected for particles on Keplerian orbits in the potential field of a point mass (see left hand plot of Figure 2.2). Measurements from gas and stellar dynamics showed that the enclosed dark mass is constant from distances of 1 pc down to 0.01 pc from Sgr A* (see right hand plot Figure 2.2). The observed accelerations of the innermost stars allowed pinpointing the location of the dark mass (Ghez et al., 2000; Eckart et al., 2002). These dynamical measurements added considerable evidence that Sgr A* is a supermassive black hole of about 3×10^6 M$_\odot$ because they excluded largely the possibility that the observed dark mass could be due to a compact cluster of dark astrophysical objects such as neutron stars or stellar mass black holes.
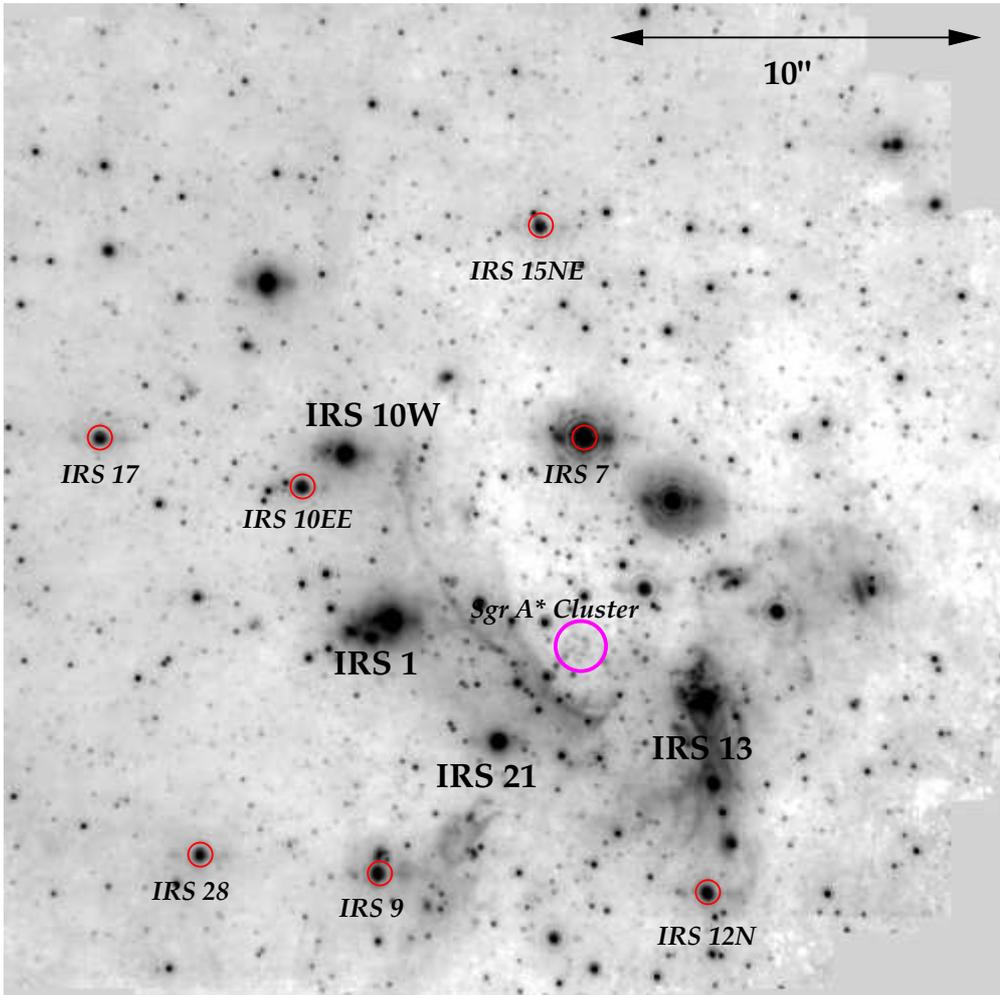
Figure 2.3: **L-band image of the GC stellar cluster** *(same region as shown in Figure 2.1). This L-band (3.8μm) image was obtained on May 10, 2003, with CONICA/NAOS at the VLT. The bright source near the middle of the image is the late-type supergiant IRS 7 (K∼ 6.5), which was used to lock the AO of NAOS. The circle in the middle marks the location of the Sgr A* stellar cluster. Sources marked with upright, bold letters denote cool, deeply embedded, dust enshrouded sources, which are found to be associated with the gas and dust of the mini-spiral. Stars marked by circles and labelled with italic letters are SiO maser stars that were used to establish the link between the NIR and the radio astrometry (see chapter 5). The diffuse NE-SW emission feature near the middle of the image is part of the northern arm of the mini-spiral. The "bar" feature of the mini-spiral is also indicated in the image: It is the diffuse, broad emission feature running NW-SE across the IRS 13 complex.*

2.2 The Interstellar Medium in the Nucleus of the Milky Way

The central parsec is surrounded by an association of several clouds/filaments of dense ($10^4 - 10^7$ cm^{-3}) and warm (several hundred K) molecular gas, usually referred to as the circum

nuclear disk (CND). The gas is generally interpreted to orbit the nucleus in a circular rotation pattern. The CND is very clumpy (volume filling factor $\sim 10\%$) and extends no further than about 7 pc from the center. It has a rather sharp inner edge at a radius of 1.5 pc. Inside this radius there is a cavity, where only atomic and ionized, but hardly any molecular gas can be found. Several streamers of gas and dust appear to be on infalling trajectories from the inner edge of the CND. They are orbiting the center and interact with the intense winds emanating from the stars in the nuclear star cluster. The streamers of ionized gas form the so-called "mini-spiral", the intense thermal radio source Sgr A West. Parts of the mini spiral can be seen in the diffuse emission in the L-band (3.8μm) image of the central parsec shown in Figure 2.3. More details on the interstellar medium in the GC can be found in the reviews by Genzel, Hollenbach, & Townes (1994) and Morris & Serabyn (1996).

2.3   Sagittarius A*

The central, compact, non-thermal radio source of our Milky Way, Sagittarius A*, was discovered by Balick & Brown (1974). Its spectrum is only well known at radio to submm wavelengths, where it is flat to inverted and shows some indication of excess emission at submm wavelengths, the so-called "submm-bump". There is a sharp drop-off of the radiation at infrared wavelengths and there has been no unambiguous detection of Sgr A* at infrared wavelengths until 2003 (Genzel et al., 2003). From its discovery on, the properties of Sgr A* have generally been interpreted in the sense of accretion of hot plasma onto a massive black hole (or alternatively ejection of plasma in a jet). Indeed, modeling shows that the radio emission of Sgr A* must be produced by compressed, hot plasma in a steep potential well (see e.g. Melia & Falcke, 2001). Such a potential cannot be created with a stable cluster of dark astrophysical objects (Maoz, 1998). The recently discovered X-ray flares of Sgr A* (Baganoff et al., 2001) are consistent with the origin of this hard radiation within about 10 Schwarzschild radii of a $3-4$ million solar mass black hole.

Very long baseline interferometry (VLBA) showed, that Sgr A* is very compact, with an upper limit on its size of the order 1 AU (Rogers et al., 1994; Krichbaum et al., 1998; Lo et al., 1998; Doeleman et al., 2001). A lower limit of ~ 0.1 AU on its size can be inferred from the absence of interstellar scintillation at 0.8 and 1.3 mm (Gwinn et al., 1991). For comparison, the Schwarzschild radius, $R_S = \frac{2GM}{c^2}$, of a black hole of 4×10^6 M$_\odot$ is slightly less than 0.08 AU.

Although there appears to be plenty of interstellar gas and dust available for accretion at the GC, Sgr A* radiates far below its Eddington luminosity. This may in part be due to a radiatively inefficient accretion flow onto Sgr A* (for a review of various models see Melia & Falcke, 2001), but must also be related to an overall low accretion rate. Recent detection of linear polarization at submm wavelengths constrain the accretion rate onto Sgr A* to the order of 10^{-8} M$_\odot$yr^{-1} (Aitken et al., 2000; Bower et al., 2003).

Backer & Sramek (1999) and Reid et al. (1999) measured the proper motion, i.e. the motion projected onto the plane of the sky, of Sgr A* compared to extragalactic sources. They found that the motion of Sgr A* is consistent with the projection of the rotation of the sun around the GC. The intrinsic velocity of Sgr A* was found to be ≤ 20 kms^{-1}. In comparison to the fast moving stars in the cluster immediately surrounding Sgr A* this yields a lower limit of 1000 M$_\odot$ on the mass of Sgr A*, adding considerable weight to the claim that this object must be a massive black hole.

Chapter 3

Cleaning and Deconvolution

When an image of some object is produced with any kind of optical system, this image will suffer a certain degradation because of the general limitations of the instrument and because of the influence of numerous external factors. For example, in the absence of an atmosphere or other degrading factors, the image of a point source, such as a very distant star, by an aberration-free telescope with a circular aperture will always be the familiar Airy pattern. This pattern arises because the limited size of the telescope will truncate the information on the spatial frequencies of the object. A perfect point image could only be produced with an inifinitely large aperture. When using ground-based telescopes, the most important additional source of image degradation is the turbulence in the Earth's atmosphere. The consequence of the combined influences of the instrument, the atmosphere, and other external factors is that the image of a point source will be characterised by a specific function, the so-called point spread function (PSF). This function will generally vary with time, e.g. due to temporal variations of the instrument or due to the limited atmospheric coherence time, as well as with the position in the imaging plane, e.g. due to the anisoplanaticity of the atmosphere.

Generally, the observed signal, $g(x, y)$, can be expressed by the convolution of the observed object, $f(x, y)$, with a function describing the PSF, $h(x, y)$, plus an additional term, $c(x, y)$, that includes the remaining degradation effects, such as anisoplanaticity, detector readout noise and other non-linear terms:

$$g(x, y) = f(x, y) \odot h(x, y) + c(x, y) \tag{3.1}$$

The symbol $\odot$ denotes the convolution operator.

There are two ways how one can improve the imaging process. On the one hand, there are technical improvements, such as improving the imaging quality of the telescopes, reducing detector noise, or suppressing the influence of the atmosphere by using techniques such as adapative optics or even launching a telescope into space. On the other hand, in spite of all possible improvements, there will always remain PSF residuals which will for example hamper the detection of faint sources near bright stars or complicate the photometry of sources whose PSFs overlap. Therefore it is always desirable to improve astronomical images further by reducing the degrading influence of the PSF with an appropriate deconvolution algorithm. This "cleaning" of astronomical images can be roughly illustrated by stating that the PSFs of point sources are replaced with Gaussian PSFs that have a FWHM comparable to the diffraction limit of the respective telescope used.

Convolution corresponds to a multiplication in Fourier space. Thus, in the case free of noise and free of non-linear effects such as anisoplanaticity, one would obtain the Fourier transform of the original object distribution by a simple division in Fourier space.

$$F(u, v) = \frac{G(u, v)}{H(u, v)} \tag{3.2}$$

Here, $G(u, v)$, $F(u, v)$, and $H(u, v)$ denote the Fourier transforms of the observed signal, $g(x, y)$, of the object, $f(x, y)$, and of the PSF, $h(x, y)$. u and v are the spatial frequencies corresponding to the x and y coordinates. We have ignored here that $H(u, v)$ will have zero values at high frequencies because a telescope cannot be infinitely large and therefore information at high spatial fequencies will be lost. In practice, one will also encounter additional problems: The term $c(x, y)$ that describes the image degradation through noise or non-linear effects, can never be neglected. Also, the shape of the PSF will never be known with arbitrary accuracy. It is usually approximated analytically or extracted from individual point sources in the observed image.

Because of these limitations, deconvolution is always an ill-posed problem that allows for more than one solution. The existing deconvolution algorithms intend to overcome the difficulties by various approaches in order to find the most probable object distribution. In the following sections we describe some algorithms that were used in the present work.

3.1 Linear Deconvolution

The linear deconvolution departs from the straightforward Fourier space devision suggested by equation 3.2. The linear deconvolution tries to circumvent the problems that the Fourier transform of the PSF is not known to arbitrarily high frequencies and that the noise term becomes dominant at high fequencies by constructing an appropriate filter, a so-called Wiener filter, that suppresses high spatial frequencies. In Fourier space, the reconstruction of the object can then be described as

$$O(u, v) = \frac{[G(u, v) + C(u, v)] \cdot \Phi(u, v)}{H(u, v)}, \tag{3.3}$$

where Φ designates the filter function and C is the Fourier transform of the noise term. The filter is chosen such that the square of the deviations between the reconstructed object $O(u, v)$ and the "true" object $F(u, v)$ is minimised, i.e.

$$\int_{-\infty}^{+\infty} |O(u, v) - F(u, v)|^2 d(u, v) = Minimum \tag{3.4}$$

Using equations 3.2 and 3.3 we obtain

$$\int_{-\infty}^{+\infty} |\frac{[G(u, v) + C(u, v)] \cdot \Phi(u, v)}{H(u, v)} - \frac{G(u, v)}{H(u, v)}|^2 = Minimum \tag{3.5}$$

In order to find the filter $\Phi(u, v)$ that minimises this function, we have to derive this equation with respect to $\Phi(u, v)$ and set the result equal to zero. We point out that because the signal and the noise are uncorrelated $\int_{-\infty}^{+\infty} (G(u, v) \cdot C(u, v)) d(u, v) = 0$.

We finally obtain

$$\Phi(u, v) = \frac{|G(u, v)|^2}{|G(u, v)|^2 + |C(u, v)|^2} \tag{3.6}$$

In practice, we can estimate the spectral energy distribution of the observed signal, $|G(u, v)|^2$, from the spectral energy distribution of the observed PSF, $|H(u, v)|^2$. The spectral energy distribution of the noise, $|C(u, v)|^2$, can be replaced in a good approximation by a delta function, $|\delta(u, v)|^2$. Taking into account that the power spectrum of a function is the product of its Fourier transform with its complex conjugate, we obtain from equation 3.3

$$F(u, v) \approx O(u, v) \approx \frac{G(u, v) \cdot \overline{H}(u, v)}{|H(u, v)|^2 + |\delta(u, v)|^2}, \tag{3.7}$$

where $\overline{H}(u, v)$ denotes the complex conjugate of $H(u, v)$. The noise term $C(u, v)$ in equation 3.3 was neglected when deriving equation 3.7.

Application of Wiener filtering leads to a characteristic "ringing" around point sources in the reconstructed image. The cause for the ringing can be described in a simplified way as follows: Since in practice we cannot know the PSF $H(u, v)$ up to inifinitely high frequencies, we have to cut off $H(u, v)$ at some upper frequencies u and v. In the most simple case, this cutting off is done by multiplication with a boxcar function. The Fourier transform of such a boxcar funtion is a function of the form $\sin(x)/x$ in the image domain. This is the source of the ringing. The ringing can be reduced by avoiding to cut out the PSF with a function with steep flanks.

3.2   Lucy-Richardson Deconvolution

The Lucy-Richardson (LR) deconvolution algorithm is an iterative method based on the scheme for the rectification of observed probability distributions suggested by Lucy (1974). The LR scheme is based on the iteration of three steps. In the first step, the current estimate of the object distribution, $O_k(x, y)$ is convolved with the PSF, $H(x, y)$.

$$\Psi_k(x, y) = O_k(x, y) \odot H(x, y) \qquad (3.8)$$

Subsequently, the obtained image, $\Psi_k(x, y)$, is compared with the observed image, $G(x, y)$.

$$R(x, y) = \frac{G(x, y)}{\Psi_k(x, y)} \odot H(x, y) \qquad (3.9)$$

Here, the convolution with the PSF acts as a low-pass filter that reduces the influence of high frequencies on the result because they are affected much stronger by noise. In the last step, the current object estimate, $O_k(x, y)$, is multiplied with the correction function, $R(x, y)$ in order to obtain the new estimate

$$O_{k+1}(x, y) = R(x, y) \cdot O_k(x, y) \qquad (3.10)$$

Because of equation 3.9, high spatial frequencies will be suppressed, avoiding thus the amplification of noise peaks. As a consequence, however, details of the image that are related to high frequencies (e.g. close double stars) will only be adequately resolved after a sufficient number of iterations has been carried out (in our experience on the order of a few 10^4). The disadvantes of LR deconvolution are the high demand for computing time, its tendency to resolve the diffuse, noisy background into distinct point sources when running a large number of iterations, and the effect that in the case of close sources that differ by several magnitudes the fainter one will be "sucked" up by the brighter one. This leads to characteristic dark areas around bright stars. The latter problem can be minimised effectively by a very accurate determination of the PSF.

3.3   Estimating the PSF

For most deconvolution algorithms such as linear or LR deconvolution one always needs to find an estimate for the image PSF before the deconvolution algorithm can be started. Such a PSF estimate can be obtained from a PSF reference source, such as an isolated star that was observed close in time to the observation of the scientific target and under similar atmospheric conditions. Alternatively, one can try to determine the PSF directly from the observed field. In the case of galactic centre observations, for example, there is a bright (K$\sim$6.5) reference star just $5.5''$ north of Sgr A*. It is more than 5 magnitudes brighter than any other source located within $\sim 2''$ of it and thus is very well suited as a PSF reference. The PSF can also be estimated by taking the average image of several fairly isolated stars in the field of view. In the

case of crowded fields, it is preferable to use the median image in order to avoid the influence of sources close to the PSF reference stars.

In crowded fields that were observed under bad seeing conditions the wings of the point sources may be so extended that it is difficult to extract a PSF even when using the median of many stars. In that case one can try to model the whole PSF or to extract the kernel of the PSF from the observed stellar field and to model just its wings. A Moffat function is usually well suited for this purpose.

Near the completion of this work, we found that the *StarFinder* software package (Diolaiti et al., 2000) [1] is an ideal tool for extracting PSFs in crowded stellar fields. It estimates an initial PSF from the median of several bright, preferably isolated stars chosen by the user. The PSF can then be improved by repeatedly identifying stars in the image and taking them into account when re-extracting the PSF. *StarFinder* can also be used for obtaining fluxes and positions of stars via PSF fitting.

A remaining limitation on the accuracy of the PSF is always the isoplanatic angle. In spite of some ongoing efforts in the community on including the spatial variation of the PSF across an image in deconvolution procedures, no satisfying solution to the problem has been found yet. This means that a certain PSF estimate can only be used for deconvolution of areas of similar size as the isoplanatic patch.

3.4   Iterative Blind Deconvolution

Iterative blind deconvolution (IBD) is an algorithm that reconstructs the object distribution in an astronomical image *and* the PSF at the same time (Jeffries & Christou, 1993). In order to achieve this aim, the algorithm takes advantage of *a priori* information on the astronomical image. Such constraints on the object distribution, $f(x, y)$ and on the PSF, $h(x, y)$, are for example:

1. $f(x, y)$ and $h(x, y)$ must both be positive (Positivity constraint).

2. They must convolve to yield the measured signal.

3. They must occupy finite nonzero regions in the image domain.

4. They must not be the trivial solution of the convolution of the observed signal with a delta funtion.

Other constraints can also be applied. A very useful one is, for example, that multiple images of the same object are constrained to have a common object. Hence, effective use can be made of the multiple images usually delivered by speckle imaging or adaptive optics observing techniques.

In IBD an error metric function is introduced to measure the violations of the above constraints.

$$\varepsilon = E_{im} + E_{conv} + E_{bl} + E_{FM} \qquad (3.11)$$

E_{im} is the image domain error. It can be described by the sum of the squares of the negative pixels in the estimate of the object and of the PSF. E_{conv} is the convolution error. It measures the quadratic deviations of the convolution of the object and PSF estimates from the measured image. E_{bl} is the band-limit error and measures the power that is contained in the PSF estimate at frequencies higher than an appropriate cutoff frequency (because the PSF cannot be known to arbitrarily high frequencies). The Fourier modulus error, E_{FM}, measures whether the estimated object contains information at frequencies higher than the diffraction limited cutoff.

---

[1]*StarFinder* is an IDL code for the analysis of crowded stellar fields, specifically developped for AO imaging. It can be obtained at the *StarFinder* page at the University of Bologna: *http://www.bo.astro.it/~giangi/StarFinder/*.

Convergence is reached via the minimisation of the error metric ε. For this purpose, the algorithm uses the conjugate gradient method as described in Press et al. (1993). On order to apply the conjugate gradient method, the derivative of the error metric with respect to each variable, i.e. each pixel in the object and PSF estimates, has to be calculated (see Jeffries & Christou, 1993).

Every deconvolution algorithm needs some kind of a priori information about the image. The advantage of the IBD algorithm is that it uses very general constraints. The frequent problem of finding an accurate PSF estimate for deconvolution is avoided in IBD. In principle, one can even start with a white noise PSF, although this would be very time consuming. While we have found IBD to work less well on single images, we have found that it can make effective use of multiple images of the same object, which poses tight constraints on the object distribution. In speckle and AO imaging observations it is common to obtain several tens to hundreds of short exposure images of the same object.

As an implementation of the IBD algorithm, we used the publicly available IDAC program code, developed at Steward Observatory by Matt Chesalka and Keith Hege (based on the earlier Fortran Blind Deconvolution code - IDA - developed by Stuart Jefferies and Julian Christou). We would like to refer the interested reader to the IDAC home page *http://babcock.ucsd.edu/cfao_ucsd/idac/idac_package/idac_index.html*.

As for the disadvantages of IBD, using this method effectively requires considerable experience of the user. Also, artefacts in the deconvolved images cannot be completely avoided. Above all, one has to mention the strong demand of computing power. We have found that deconvolution with current average PCs or workstations is not practical for arrays larger than about 256×256, when using several tens of input images.

3.5 Comparison and Combination of Deconvolution Algorithms

In the upper left panel of Figure 3.1 we show a simple shift-and-add[2] (SSA) image of about one hundred 0.5 s-exposure speckle imaging frames of the GC IRS 16 cluster observed with SHARP at NTT in 2001. A linear deconvolution of this image can be seen in the upper right panel. The lower left and right panels show a LR and an IBD deconvolution, respectively, of the SSA image. It can immediately be seen, how deconvolution facilitates the detection of sources that are located in the broad PSF wings of bright stars.

The maps resulting from the different deconvolution algorithms compare very well among each other and with the SSA image. The advantage of deconvolution becomes clear because the deconvolved maps are much richer in detail. In the linearly deconvolved map the "ringing" effect can be seen around the brighter sources. Some artefacts can also be seen around the brighter sources in the LR and IBD deconvolved images, but they are less grave than in the case of linear deconvolution. A typical problem are the blank areas around bright sources, where faint sources cannot be reconstructed reliably. The rings around the brighter sources in the IBD map are probably caused by restricting the initial estimate PSF to a limited size with a circular aperture, i.e. a sharp cutoff at high frequencies.

In the ideal case, one should obtain a map of delta functions after deconvolution of an image containing only point sources. Of course, since the detector image is discreetly sampled in pixels, this is an idealisation. Apart from this we will still find some remnant structure of the point sources. In the case of LR deconvolution, this can e.g. be due to anisoplanacy, when the PSF was extracted not in the immediate vicinity of the field of interest (a very small isoplanatic patch can also be a problem for IBD, of course). We therefore applied a two stage

---

[2]The simple shift-and-add algorithm is commonly used in the reduction of series of speckle or AO imaging frames. Before averaging the individual exposures, they are shifted to the peak of a common reference source. For details, see Eckart et al. (1994).
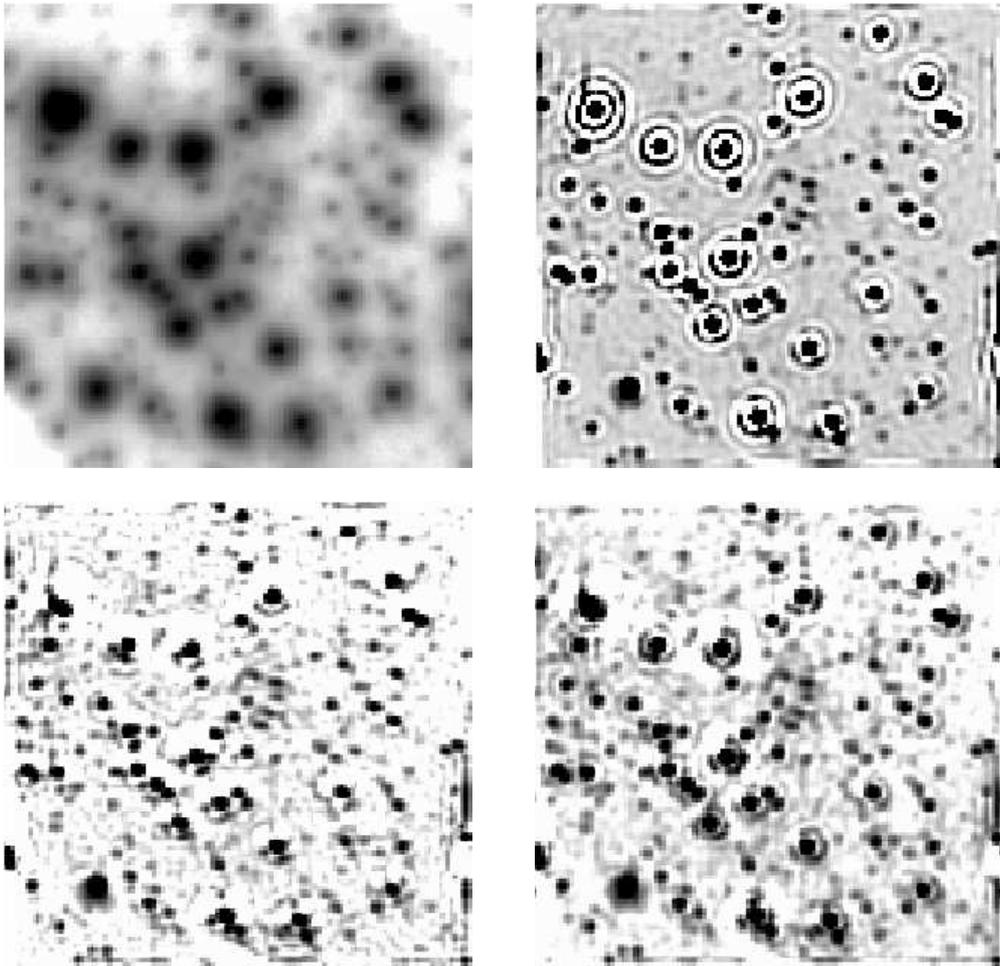
Figure 3.1: **Comparison of different deconvolution methods**. *Upper left panel: SSA image of the IRS 16 cluster as seen by SHARP at NTT In 2001. Upper right panel: Linear deconvolution. Lower left panel: LR deconvolution. Lower right: Deconvolution with IBD (IDAC). The LR and IBD deconvolved maps were smoothed with a Gaussian of FWHM 80 milliarcseconds.*

deconvolution. We resampled the resulting map from a LR or IBD deconvolution to a third of the pixel scale (i.e. one pixel was replaced by 9 pixels), smoothed the resampled image with a Gaussian of $\sim 2/3$ of the FWHM expected from the telescope resolution and determined a local remnant PSF for a region of interest from the median of about five bright sources in this resampled map. In a second step, we then applied a LR deconvolution to the resampled map and smoothed the resulting map with a gaussian of the appropriate FWHM. As a result, close point sources could be separated better than with just a one stage deconvolution. In Figure 3.2 we show the maps as they resulted from such a two stage deconvolution in the case of SHARP/NTT images of the IRS 16 cluster. We compare a LR-LR and a IBD-LR deconvolution. As can be seen, the resulting final maps are in very good agreement. As for the faintest sources, there is a tendency of the LR algorithm to break the noisy background up into point sources. The IBD map has a smoother background. This indicates that it should work better on extended sources.
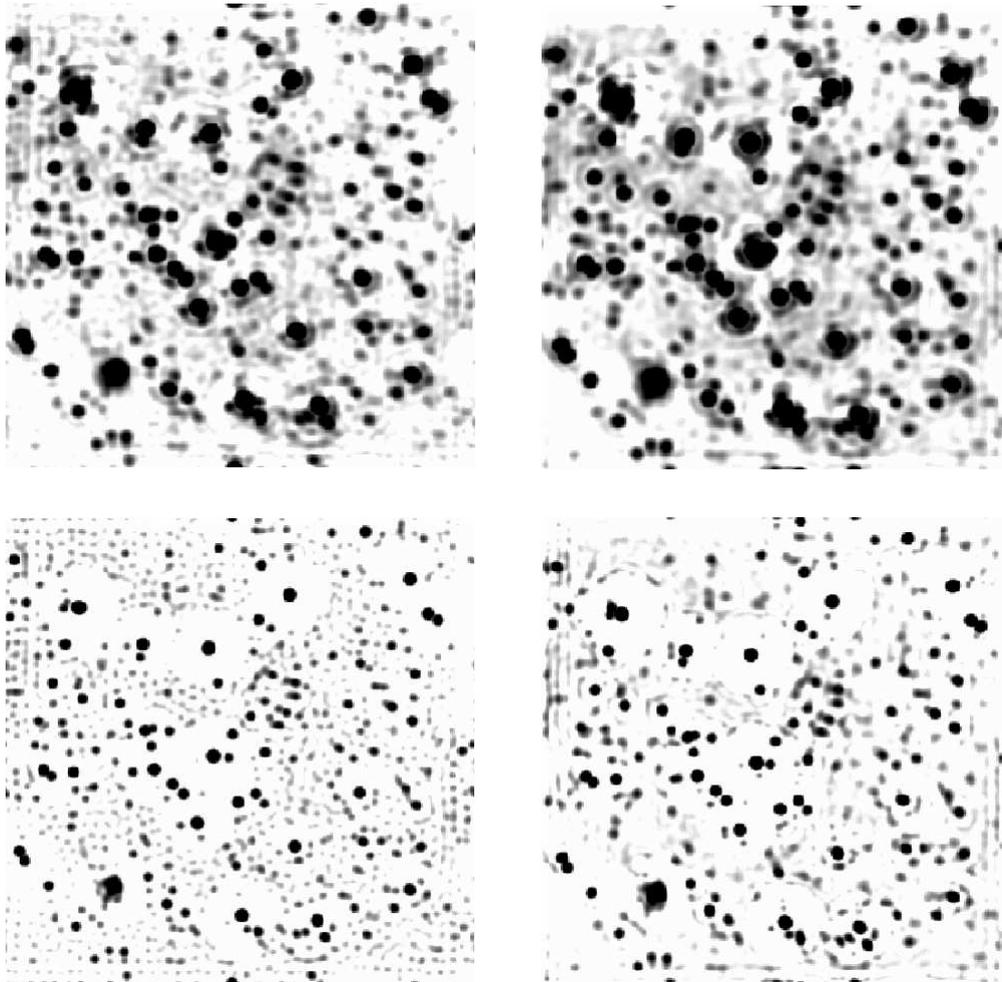
Figure 3.2: **Deconvolution in two stages**. *Upper panels: Resampled and smoothed maps of the IRS 16 cluster as they result from a LR (left) and an IBD (right) deconvolution. PSF residuals can be seen in both maps. This remnant PSF can be constructed from the median of several bright sources and used for a second deconvolution (LR in both cases). The results of this deconvolution can be seen in the lower panels. The final maps were smoothed with a PSF of an appropriate FWHM.*

Chapter 4

Observations and Data Reduction

4.1   The SHARP/NTT Imaging Data Set

The SHARP near-infrared speckle camera was built at MPE for high resolution imaging observations as a guest instrument at the ESO 3.6m NTT telescope at La Silla, Chile (Hofmann et al., 1995). SHARP was equipped with a 256×256 pixel NICMOS array. It covered a wavelength range from 1μm to 2.5μm and had a pixel scale of about 50 mas per pixel. Since 1991 it was used in one or two observing runs each year at the NTT. The excellent atmospheric conditions and the fact that the GC passes close to zenith in La Silla made it possible to use integration times as long as 1 s and still obtain information at the diffraction limit of the NTT in the images. All SHARP imaging data used for the present work were taken in the K-band (central wavelength 2.2μm) with 0.5 s integration time, which was found to be the optimal choice for satisfying the somewhat contrary aims of a high signal-to-noise (S/N) ratio while conserving at the same time information at the diffraction limit of the NTT.

The GC stellar cluster was usually imaged in series of 500 or 1000 exposures. The FOV of SHARP at the NTT was about $13''$. Applying offsets of a few arc-seconds between the imaging series allowed for a $\sim 20''$ field-of-view (FOV) in the final mosaics. The IRS 16 cluster of bright HeI stars and the SgrA* cluster were always contained in the FOV.

The aim of the present work was to obtain deep high-quality maps of the central region within about $1.5''$ of Sgr A*. We therefore selected only the best speckle frames of a given epoch. From the several tens of thousands of individual speckle frames obtained in each observing epoch, we pre-selected ∼1000 high-quality frames automatically. Selection criterion was the number of bright speckles of the dominant star in a frame: Beside the brightest speckle, there should be not more than one additional speckle with more than 10% of the flux of the brightest speckle. From the pre-selected frames we picked by eye several hundred speckle frames with the highest quality. Selection criterion was that the first diffraction ring around the dominant speckle of the brightest stars must be clearly visible in these individual 0.5 s exposures. The visual inspection of the individual frames had the further advantage that frames where occasional hot pixels were present at the location of the SGR A* cluster or where the telescope lost tracking could be removed from the data set. In Figure 4.1 we compare a speckle frame observed under moderate to bad atmospheric conditions (lower left panel: characterised by a low S/N and many speckles per source) to a frame observed under excellent conditions (upper left panel: long coherence time of the atmosphere; first diffraction ring visible around brighter sources).

For every observing epoch, the final selection of highest quality images was divided into ∼ 4 subsets of about one hundred frames each. After combining the frames of such a subset with the simple shift-and-add (SSA) algorithm, the Strehl ratio was found to be of the order 30% in the final images, compared to Strehl ratios of the order 10% in SSA images made from speckle data cubes without frame selection. The difference in quality between average SSA
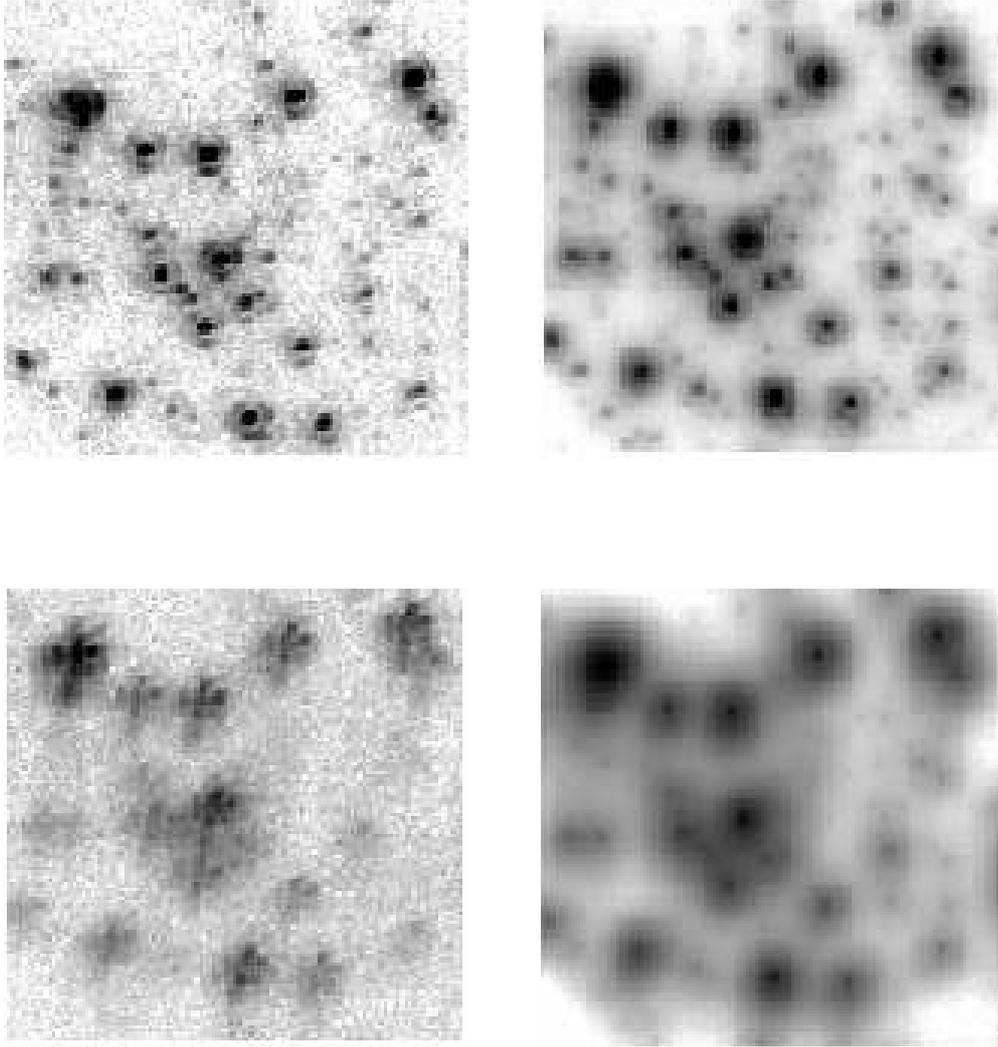
Figure 4.1: **Quality of speckle images.** *Bottom left: Speckle frame obtained under moderate to bad atmospheric conditions. The S/N is low, faint sources are not visible and the brighter sources are broken up into numerous speckles. Top left: Speckle frame observed under excellent atmospheric conditions. The S/N is high and the image is basically a diffraction limited short exposure with the first diffraction rings clearly visible around the brighter sources. The visible stars have K-magnitudes between about 9 and 14. Bottom right: SSA image of an average speckle imaging data cube; Strehl ratio about 15%. Top right: SSA image of a cube of about 100 high quality speckle frames; Strehl ratio of about 35%. Numerous faint sources, which cannot be seen in the bottom right image, can be distinguished in this high-quality image.*

images and SSA images resulting from rigorous selection of the best speckle frames can be seen in Figure 4.1.

We applied Iterative Blind Deconvolution on the sets of high-quality speckle frames. For this purpose we used the publicly available IDAC program code, developed at Steward Obser-

vatory by Matt Chesalka and Keith Hege (based on the earlier Fortran Blind Deconvolution code - IDA - developed by Stuart Jefferies and Julian Christou).The SSA images of the sets of speckle frames were used as initial object estimates. Because of the high demand of computing time for this algorithm, we applied it only to a $\sim 6 \times 6''$ area around Sgr A* that included the IRS 16 complex of bright (K$\sim$10) sources. After convergence of the IBD algorithm, the resulting 3 to 4 object images of every observing epoch were oversampled to a third of the original pixel scale, smoothed and co-added. Such an image is shown in Figure 3.1. As can be seen, there are still some PSF artifacts or residuals common to all sources. Therefore the images were cleaned in a final step with a Lucy-Richardson deconvolution. We produced final maps by restoring the result of the deconvolution with a Gaussian beam of 100 mas FWHM (see Figure 3.2).

As a control of the deconvolution procedure, we also produced maps in a similar way by using the LR algorithm instead of IBD on SSA images of the selected frames. The maps compare very well with the ones produced with the aid of IBD. However, we found that IBD provided maps of practically constant quality for all epochs, while the quality is slightly more variable in case of the LR algorithm. A possible cause for this may be that one needs to use a PSF estimate for a LR deconvolution. We used the bright, isolated source IRS 7 as PSF reference. It is ~ 5 magnitudes brighter than any other star in its immediate surroundings and is thus very well suited as a PSF reference. However, in some cases the PSF reference was not taken simultaneously with the imaging data, in other cases the anisoplanatic angle might have been smaller than the distance from IRS 7 to Sgr A*. Therefore the results of the LR deconvolved maps are of slightly more variable quality than the IBD maps and we decided to use the latter in our further analysis because they guaranteed an equal treatment and quality of all the maps.

In the described way, we obtained high-resolution maps for all epochs, except for 1993 and 2002, where the quality of the imaging data did not allow to select a sufficiently large sample of high-quality speckle frames. The maps are shown in Figure 7.1. The 1992 speckle frames are characterised by a fairly strong readout "waffle" pattern. While the resulting high-resolution map for 1992 compares favourably with the other epochs, the stellar positions may be subject to larger errors for this epoch.

Our method here was optimised for producing deep (K(3-5σ)$\approx$16) diffraction limited SHARP/NTT maps of comparable quality for all observing epochs. This is in contrast to our earlier work, such as Eckart & Genzel (1997). There, deep high-resolution maps were produced only for a few selected epochs. The approach of Ott (2003) was also distinct from the one presented here: They deconvolved and analysed several tens of SSA images for every SHARP observing period in a largely automatised way. While their maps allow to effectively determine proper motions for $\sim$1000 stars in a $\sim 10''$ radius region around Sgr A*, they are generally $\sim$0.5 to 1 magnitude shallower and of more variable quality than the maps used in this work, which serve the purpose to examine the proper motions in the very central, most crowded part of the cluster, and for the weakest sources possible. The Ott (2003) and our approach presented here can be seen as mutually complementary.

In order to verify the SHARP high-resolution maps, we compared them among each other to check whether the identified sources and proper motions were consistent between the epochs. An additional check was the comparison between the IBD and the LR deconvolved maps. For the epochs around 2000, we also compared the SHARP maps with the maps obtained from the Gemini and NACO data sets (see below). In Figure 4.2 we show the the Gemini 2000, the SHARP 2001 (IBD and LR), and NACO 2002 maps, all of them restored to a FWHM of $\sim$100 mas.

June 2001, SHARP, LR June 2001, SHARP, IBD

July 2002, Gemini May 2002, NACO
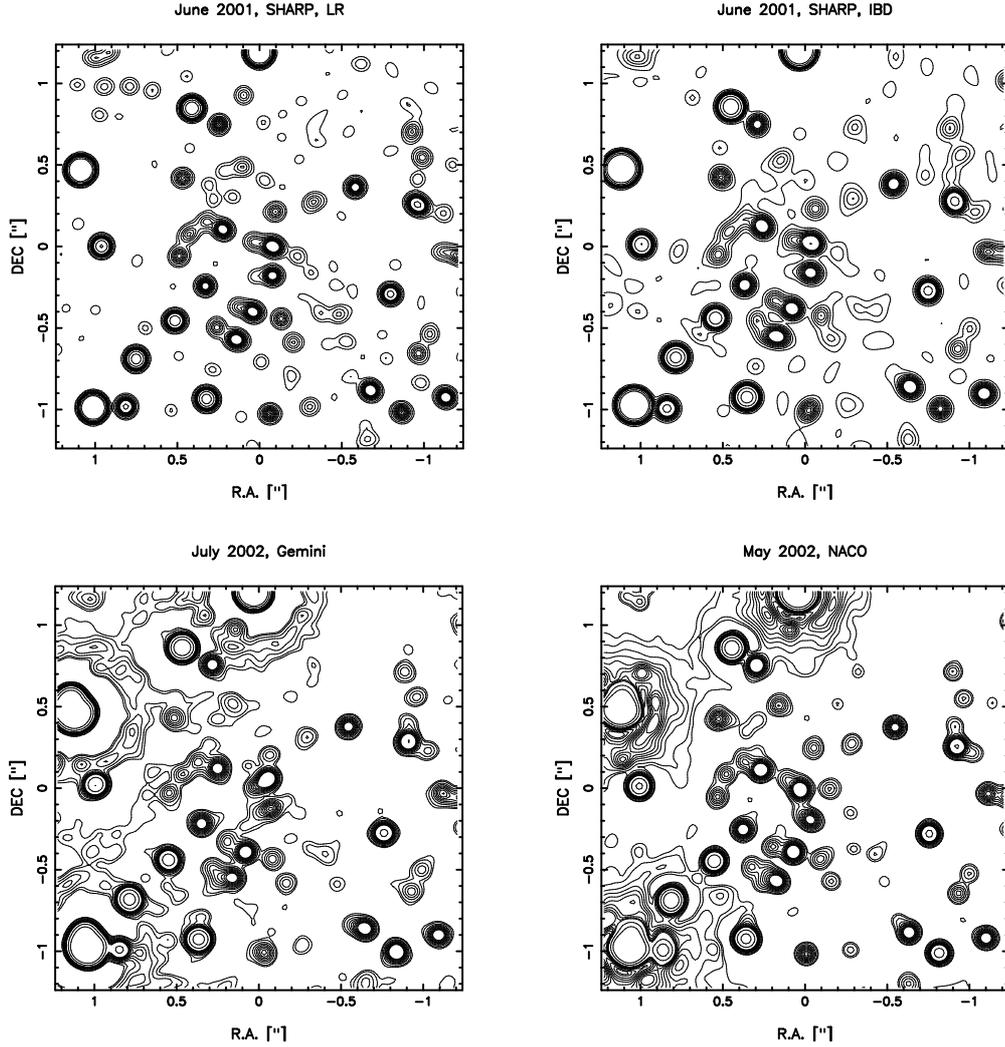
Figure 4.2: **A comparison of high-resolution maps of the central** $\sim 1.2'' \times 1.2''$ **of the GC stellar cluster.** *The restoration beam FWHM was approximately 100 mas in all the images. Upper left: SHARP/NTT 2001, deconvolved with IBD; upper right: SHARP/NTT 2001, deconvolved with LR; lower left: Gemini 2000 (LR); lower right: NACO 2002 (LR). The bright sources at the left and upper edges of the field were saturated in the latter two data sets and show ample deconvolution artifacts in form of rings. Contours were drawn at 10, 20, . . . 90, 100, 200, 400% of the peak flux of S2, the source closest to the centre in all images.*

4.2 Gemini Imaging Data

The Gemini North observatory Galactic Center Demonstration Science Data Set with imaging observations from the year 2000 is publicly available. This data set provides observations of the Galactic Center stellar cluster with the Gemini North telescope, the Quirc near infrared camera and the Hokupa'a AO system. We selected a K'-band (2.12μm) image of 750 s total integration time, observed in July 2000. Since the Hokupa'a AO system was designed for a 4m-class telescope, it could only partially provide the correction needed for the 8m-class Gemini telescope. Moreover, the visible guiding star used for the observations is located at

Filter Name	Central Wavelength [μm]	Width [μm]
H	1.66	0.33
K$_S$	2.18	0.35
L'	3.80	0.62

Table 4.1: *CONICA NIR broad band filters (values taken from the ESO NAOS-CONICA user manual).*

$\sim 30''$ from Sgr A*, so the Strehl ratio of the image is rather low. However, the central sources around Sgr A* are clearly resolved at an estimated resolution of 100 mas.

We extracted a PSF from the median of $\sim$ 15 bright, unsaturated stars in the image. Because the wings of the PSF were very strong, but contaminated by weak sources, we fitted the wings of the PSF with a Moffat function. Subsequently, we created a model PSF by combining the model for the wings with the PSF Kernel obtained by the median of the stellar images. This PSF model was used for a LR deconvolution of the K'-band image, which was re-convolved to a final map with a Gaussian beam of $\sim$100 mas FWHM. We did not use the IDAC algorithm because it works less well if there is only one image of the object available.

4.3 NAOS/CONICA Imaging Data

The GC stellar cluster was observed several times during the commissioning and science verification of the NAOS/CONICA ("NACO") AO system and near infrared camera at the ESO VLT unit telescope 4 (Yepun) in spring/summer 2002. In 2003, several epochs of regular H, K$_S$, and L'-band GC imaging observations were obtained with NACO (See Table 4.1 for the properties of the filters used). For simplicity, we will use the expressions "K-band" and "L-band" in this work because the differences in transmission to K$_S$ and L' are negligible for our purpose. For the observations in the K and H bands, the loop of the AO was closed with the infrared wavefront sensor on the K$\sim$ 6.5 mag supergiant IRS 7, which is located $\sim 5.5''$ north of Sgr A*. Because of instrument restrictions, AO correction for the L-band observations in the 2002 epoch could only be carried out with the visible wavefront sensor, locking on a faint $V \sim 14$ star about $30''$ north-east of Sgr A*.

The NACO observations were made in blocks of several tens of short exposures images, with typical integration times of $\sim$ 15s for H and K-band and 0.2s for L-band observations. The individual frames were corrected for detector bias and dead/hot pixels. Sky images were produced from the median of tens of dithered exposures or from separate sky measurements. The sky background was subsequently subtracted from the images and flat-fields were applied to remove the pixel-to-pixel variations in the detector sensitivity. Sources brighter than $K \approx 10$ were saturated in all H and K band frames with moderate to high image quality. Saturation was less of a problem in the L band, with only the two brightest sources saturated. Table 4.2 provides a summary of NACO GC imaging observations in 2002 and 2003. The Strehl ratios[1] given in the table are approximate values (estimated absolute error $\pm 5\%$). They serve as a measure of the image quality. The performance of the NAOS AO system depends strongly on the momentary atmospheric turbulence, especially on coherence time, but Strehl ratios as high as 50% in H band, $50 - 70\%$ in K band and about 90% in L band can be routinely achieved under good conditions.

---

[1]Briefly stated, the Strehl ratio is the ratio of the peak intensities between the degenerated (i.e. through instrumental and external effects) and ideal (e.g. an Airy pattern) PSFs. It is commonly used in AO to provide a measure for the quality of the image correction.

Date	Filter	Pixel Scale [″/pix]	DIT [sec]	NDIT	N	$T_{i,total}$ [sec]	Strehl [%]
03 Apr 2002	K_s	0.027	0.5	8	10	40	5
03 May 2002	K_s	0.027	20.0	3	20	1200	50
03 May 2002	L'	0.027	0.2	50	20	200	20
24 May 2002	K_s	0.013	15.0	1	60	900	10
30 May 2002	K_s	0.013	15.0	1	90	1350	20
31 May 2002	K_s	0.013	15.0	1	65	975	10
02 Jun 2002	K_s	0.013	15.0	1	45	675	30
30 Jul 2002	K_s	0.027	15.0	4	20	1200	15
20 Aug 2002	L'	0.027	0.2	150	76	2280	50
30 Aug 2002	L'	0.027	0.2	150	75	2250	50
30 Aug 2002	K_s	0.013	15.0	4	20	1200	50
30 Aug 2002	H	0.013	15.0	4	25	1500	30
20 Mar 2003	H	0.013	20.0	1	32	640	50
20 Mar 2003	L'	0.027	0.2	400	12	960	85
09 May 2003	H	0.013	10.0	6	40	2400	55
10 May 2003	Ks	0.027	0.5	120	19	1140	40
10 May 2003	L'	0.027	0.2	300	20	1200	90
10 May 2003	L'	0.027	0.2	300	20	1200	90
13 Jun 2003	Ks	0.013	5.0	3	102	1530	40
13 Jun 2003	Ks*	0.013	20.0	1	64	1280	50
13 Jun 2003	Ks*	0.013	20.0	1	64	1280	50
13 Jun 2003	Ks*	0.013	20.0	1	63	1260	50
13 Jun 2003	Ks*	0.013	20.0	1	60	1200	50
15 Jun 2003	Ks	0.013	20.0	1	172	3440	65
16 Jun 2003	H	0.013	20.0	1	48	960	40
16 Jun 2003	L'	0.027	0.2	300	23	1380	80
16 Jun 2003	Ks	0.013	10.0	2	186	3720	40
21 Jul 2003	H	0.013	20.0	3	72	4320	40

Table 4.2: **GC imaging Observations with NACO in 2002 and spring/summer 2003.** *DIT is the detector integration time. NDIT is the number of sub-integrations that were co-added to a single image by a pipeline. N is the number of such images obtained per observing run. The total integration time, $T_{i,total}$, is given by DIT×NDIT×N. The Strehl ratio is given as an approximate measure of the image quality. The absolute errors of the Strehl ratios were estimated to be of the order $\pm 5\%$. Polarimetric observations are marked with an asterisk behind the filter name.*

IBD was not used on the NACO data. On the one hand, for an effective use of IBD one needs to use several tens of individual NACO frames. However, all short exposure frames were characterised by a detector "waffle" pattern, which could not be entirely removed through bias correction, sky subtraction and flat-fielding. The IDAC program clearly had problems with this pattern and produced noisy maps. On the other hand, IBD needs large amounts of computing time and is not very well suited for large image arrays such as the CONICA detector with 1024×1024 pixels..

Therefore, we produced final long exposure images by co-adding all individual frames with the SSA technique. The waffle pattern was largely suppressed by this procedure. From the final images we then extracted median PSFs with *StarFinder*, which were used for LR or linear deconvolution. In the case of LR deconvolution, final maps were obtained after restoration with a Gaussian beam of ~ 60 mas FWHM in K (~ 40 mas FWHM in H).

Chapter 5

Astrometry

It was the aim of our study to observe and describe the interactions of the nuclear star cluster of the Milky Way with the putative central supermassive black hole Sgr A*. The stellar velocity dispersion of the cluster can be used to determine the amount of dark mass enclosed in a given volume (Eckart & Genzel, 1996; Ghez et al., 1998; Genzel et al., 2000). Stellar accelerations can be used to pinpoint the location of the dark mass (Ghez et al., 2000; Eckart et al., 2002; Sch¨odel et al., 2003). Should Sgr A* be a black hole, one could also try to look for gravitationally lensed stars in order to pinpoint its position and weigh its mass (Alexander, 2001). Establishing an accurate astrometric system in order to know the exact position of the stars relative to Sgr A* is of enormous importance for these purposes. Also, a well constrained position of Sgr A* relative to the surrounding stars facilitates the search for a near-infrared counterpart of that source considerably. In this chapter we will describe how we established an astrometric system for observations of the GC stellar cluster.

5.1 Establishing the Astrometric Reference Frame with SiO Masers

While Sgr A* is one of the brightest radio sources in the sky, it cannot be easily identified in NIR imaging because of its faintness in this wavelength regime and the crowding of stars in its surroundings. Therefore, establishing accurate astrometric positions for the sources observed in NIR images of the GC is an essential task. This can be accomplished by using the positions of SiO maser stars. With the help of radio interferometry, the positions of such stars can be determined with an accuracy of ≤ 1 mas (Menten et al., 1997; Reid et al., 2003). Menten et al. (1997) identified the position of Sgr A* in NIR SHARP images with this method. However, because of the small field-of-view of SHARP they could use only two maser stars for this purpose. Therefore they could just determine the rotation angle and a single pixel scale for their NIR images. For an accurate astrometry, it is highly desirable, however, to measure higher order imaging parameters. This is only possible if one can use a greater number of SiO masers for the measurements.

Reid et al. (2003) combined several epochs of VLA [1] and VLBA [2] observations to determine exact positions and proper motions for seven SiO masers within $15''$ of Sgr A*. We reproduce the positions and proper motions of these stars as given by Reid et al. (2003) in Table 5.1. They represent the basis for the astrometry of our infrared observations. Comparing

---

[1] Very Large Array, a radio interferometer operated by the National Radio Astronomy Observatory in Socorro, New Mexico, USA

[2] Very Long Baseline Array, an interferometer composed of a group of ten radio antennas spread across the USA
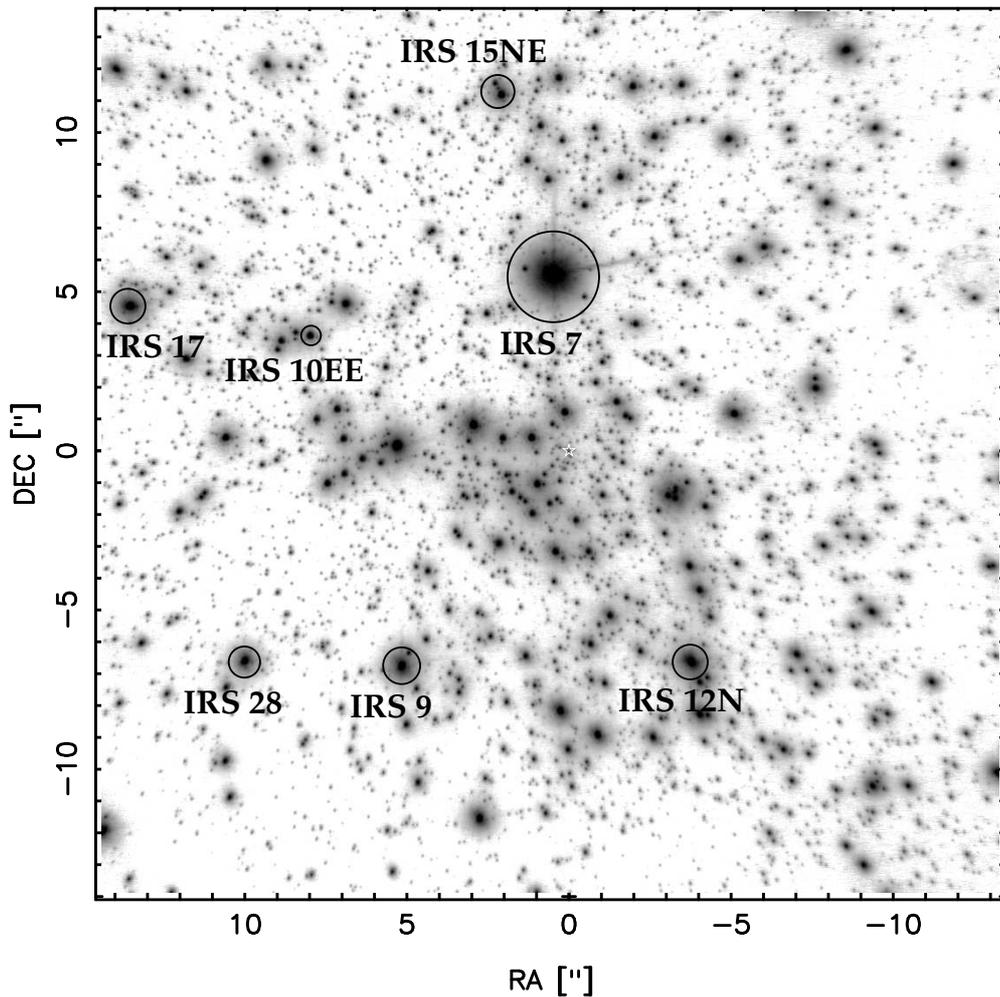
Figure 5.1: **NACO GC K band image from May 2002.** *This image was used to establish the astrometric positions of stars in the infrared frame. The 7 maser sources in the field-of-view are marked by circles. Their positions and proper motions, measured with radio interferometry, are listed in Table 5.1. The position of Sgr A* is marked by an asterisk. Offsets from Sgr A* in arc-seconds are marked on the x- and y-axes, positive to the north and to the east.*

the pixel positions of these maser stars in a NIR image with their offsets in right ascension and declination relative to Sgr A* as measured by radio observations allows us to tie stellar positions in NIR images to the radio astrometric frame.

K-band observations of the GC star cluster with the S27 camera of CONICA/NAOS in May 2002 (epoch 2002.34) provided high quality AO images of this region with a field-of-view containing all seven SiO masers listed in Table 5.1. We show the final mosaic image from May 2002 in Figure 5.1. The SiO masers are marked by circles in this image.

Star	$\Delta\Theta_x$ (arcsec)	$\Delta\Theta_y$ (arcsec)	μ_x (mas y^{-1})	μ_y (mas y^{-1})	Epoch (y)
IRS 9	$+5.6531 \pm 0.0006$	-6.3493 ± 0.0013	$+3.60 \pm 0.53$	$+2.40 \pm 1.13$	1999.24
IRS 7	$+0.0364 \pm 0.0013$	$+5.5461 \pm 0.0043$	-1.57 ± 0.92	-4.54 ± 3.47	1999.55
IRS 12N	-3.2531 ± 0.0003	$-6.8853 \pm .0003$	-0.82 ± 0.22	-2.81 ± 0.26	1997.77
IRS 28	$+10.4694 \pm 0.0010$	-5.7944 ± 0.0022	-0.37 ± 1.30	-2.95 ± 2.27	2000.44
IRS 10EE	$+7.6840 \pm 0.0003$	$+4.2150 \pm 0.0003$	$+0.20 \pm 0.16$	-2.12 ± 0.20	1998.52
IRS 15NE	$+1.2283 \pm 0.0003$	$+11.3249 \pm 0.0004$	-1.66 ± 0.24	-5.96 ± 0.35	1997.54
IRS 17	$+13.1501 \pm 0.0026$	$+5.5651 \pm 0.0025$	...	...	2000.85

Table 5.1: **Positions and proper motions of SiO masers within** $15''$ **of Sgr A*.** *The data were taken from Reid et al. (2003) and are based on several epochs of observations with the VLA and VLBA. $\Delta\Theta_x$ and $\Delta\Theta_y$ are angular offsets, μ_x and μ_y are proper motions, relative to Sgr A*, toward the east and north, respectively, in the J2000 coordinate system.*

5.2 Image Transformation

5.2.1 Transformation Equations

The transformation between the position (x_r, y_r) of a star in a reference frame (such as the astrometrically correct radio frame) and its position (x_i, y_i) in any other image of the same region can be described by the following second order transformation equations:

$$x_r = a_0 + a_1 x_i + a_2 y_i + a_3 x_i^2 + a_4 x_i y_i + a_5 y_i^2$$
$$\text{and}$$
$$y_r = b_0 + b_1 x_i + b_2 y_i + b_3 x_i^2 + b_4 x_i y_i + b_5 y_i^2$$
(5.1)

Here, the terms $a_{0,1,2}$ and $b_{0,1,2}$ describe the linear transformations such as shift, image rotation and scaling, while the remaining terms express second order distortions of the image, such as shear. The available number of reference stars determines up to which order the transformation parameters can be determined. This means that one needs at least six reference stars in order to solve for all 12 parameters of the above equations. In practice it is desirable to solve an overdetermined system of equations, in order to minimise the errors of the resulting parameters. In that case, the system of equations can be solved with the least squares technique.

5.2.2 Extracting Stellar Positions from the NIR Image

The positions of the maser stars in the infrared image were measured by determining their centroid positions within a certain aperture. The centroid position (x_{cen}, y_{cen}) is defined by

$$x_{cen} = \frac{\sum_{aper} x \times I}{\sum_{aper} I}, \quad \text{and} \quad y_{cen} = \frac{\sum_{aper} y \times I}{\sum_{aper} I},$$
(5.2)

where x and y are pixel coordinates and I pixel intensities , and the sum is made over all pixels in the aperture. Since the centroid depends on the size of the aperture used, we repeatedly measured the centroids of the maser stars with different apertures. The results are shown in Figure 5.2, where we plotted the deviation of the maser centroid positions from their average for aperture sizes between 1 and 18 pixels. We also repeated the experiment on different image types, the raw SSA image, a smoothed version of the SSA image (because of correlated detector readout noise visible in the SSA image), an image deconvolved with the Lucy-Richardson algorithm and an image deconvolved with the linear Wiener filter technique. An aperture of seven pixels was found to be a good choice for all cases. We estimated the accuracy of the centroids by comparing the results for apertures between six and 8 pixels. We found that the pixel positions of the masers stars could be determined with an error of ≤ 0.05 pixel, corresponding to about 1.4 mas.
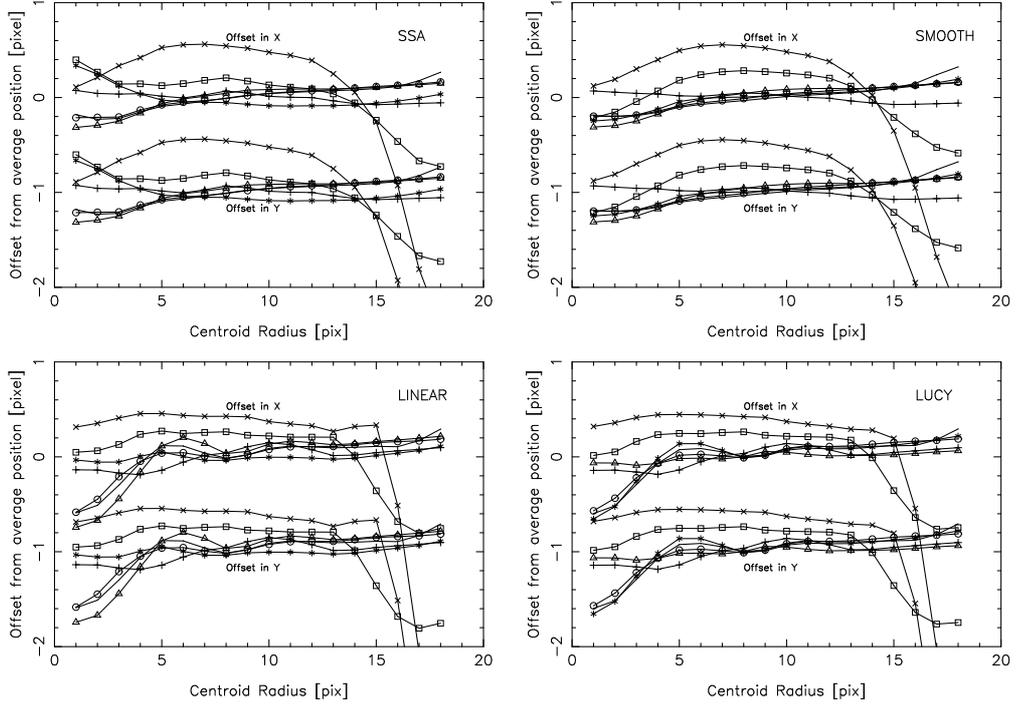
Figure 5.2: **Dependence of measured x and y pixel centroid positions in the May 2002 NACO image on the chosen aperture size.** *Different plotting symbols refer to different maser stars. The positions resulting from averaging over all aperture sizes were subtracted in order to just show the deviations of the pixel positions. y positions are shifted by a value of -1.0.*

5.2.3 Order of the Transformation

In the case of the GC stellar cluster, we could use the measured radio positions of 7 maser stars to solve the system of equations defined by 5.1 for all transformations parameters up to second order. However, since the system will be only marginally overdetermined, we have to check whether the second order parameters calculated in this way are meaningful.

The radio positions of the SiO masers and their uncertainties can be calculated from Table 5.1. For the epoch 2002.34 their uncertainties are generally ≤ 1 mas. Combining the errors of the radio positions and of the extracted pixel positions of the stars quadratically, we arrive at an overall error of ~ 1.7 mas for the maser star positions. In order to estimate the errors on the transformation parameters we set up a Monte Carlo simulation. The positions of the 7 maser stars were varied randomly within ± 1.7 milliarcsecond error boxes before solving for the transformation parameters. After performing several thousand iterations we obtained averages and standard deviations of the transformation parameters. While the linear transformation parameters resulted to be highly significant, with the uncertainties being 2 to 3 magnitudes smaller than the respective average values, the second order transformation parameters had a significance of only about 2σ.

As a further test of the significance of the second order transformation parameters, we used the maser positions from the LR deconvolved (and beam restored) image and repeatedly solved the equation system 5.1, each time using a different subset of six out of seven maser stars. In this way, we also estimated the mean values and standard deviation of all twelve transformation parameters. The results are given in Table 5.2. In some cases the uncertainties of the second order parameters were as large as the corresponding mean values, e.g. in the case of a_4 or b_4.

But some of the second order parameters appeared to have a $\geq 5\sigma$ significancy, such as a_3, a_5, b_3, and b_5.

With the results of these tests, we decided to solve the astrometric equations up to second order because some of the high order terms appeared significant and because it is natural to expected that the optical system of CONICA is not entirely free of distortions – even if they might be small. A higher precision in the astrometry can in principle be obtained with a greater number of maser stars. Doubling their number would for example decrease the uncertainty of the transformation parameters by a factor of the order $\sqrt{2}$.

5.3 Positions and Their Uncertainties

Here, we briefly examine the possible uncertainties of the astrometric positions of Sgr A* and of the surrounding stars. We examine the importance of the order of the astrometric solution (linear or quadratic), of image deconvolution, and of anisoplanatic effects.

5.3.1 The Position of Sgr A* on the NIR Image

In Figure 5.3 we show NACO K-band images of the central $1'' \times 1''$ of the nuclear star cluster for May 2002 and August 2002. The astrometric position of Sgr A* is indicated by a cross with a 30 mas circle. The images show how the bright star S2 passed very close to Sgr A* in spring 2002. Thereby it moved so fast that the change between its positions can be clearly seen between the two epochs, although the images were taken only about three months apart.

In the following, we examine possible sources of uncertainty for the pixel position of Sgr A* on infrared images.

- **Order of the astrometric solution**. We compared the positions of Sgr A* in the infrared image obtained for the two cases of solving the astrometry just for linear terms and of including the quadratic terms. The pixel position of Sgr A* is found to differ by $0.1 - 0.2$ pixels between the two cases. This corresponds to about $3 - 5$ milliarcseconds.

- **Deconvolution**. When comparing the pixel positions of Sgr A* between the cases of linear and LR deconvolution we found an error of < 0.05 pixel or < 1.4 mas. However, we found a significance offset (> 10 mas) of the Sgr A* position between the deconvolved images and the SSA image. This may in part be due to a general shift of the maser star pixel positions due to the influence of the wings of the PSF. We obtained systematic offsets between the maser star pixel positions between the deconvolved and SSA images. Since we know from the dynamical determination of the position of Sgr A* (see chapter 8) that it is almost coincident with the nominal radio position (determined on

Parameter	Value	Error	Parameter	Value	Error
a0	15.4293	0.00439647	b0	-12.6907	0.00186175
a1	-0.0269081	4.68078e-05	b1	-0.00210807	1.98207e-05
a2	-0.00205253	6.65029e-06	b2	0.0268209	2.81605e-06
a3	-9.13362e-08	8.24334e-09	b3	-2.51223e-08	3.49065e-09
a4	-3.74864e-08	5.33297e-08	b4	1.68641e-08	2.25825e-08
a5	1.89892e-08	4.41423e-09	b5	1.0335e-07	1.86921e-09

Table 5.2: **Image transformation parameters for aligning pixel positions in the May 2002 NACO image of the GC stellar cluster with the SiO radio reference system.** *Parameters are as given in equations 5.1. The values of the parameters and their errors were determined by repeatedly solving the system of equations with different subsets of six out of seven maser stars.*
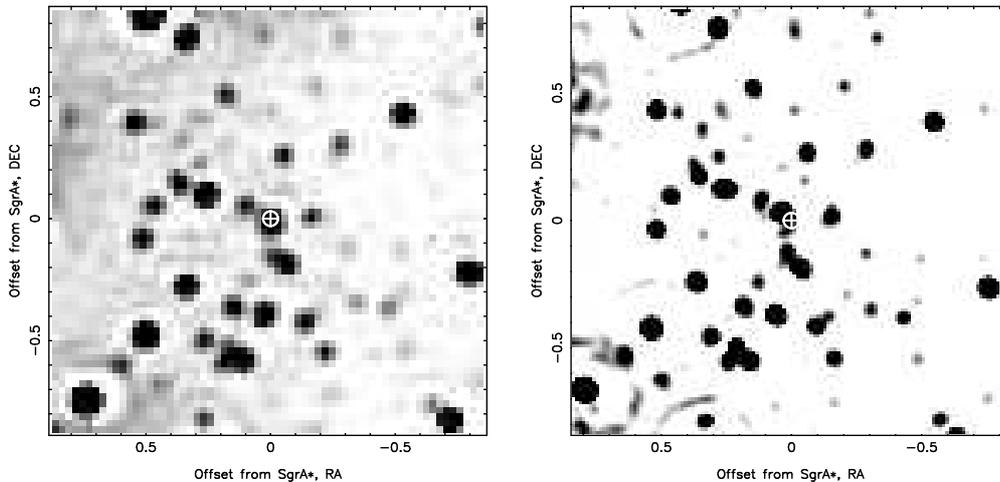
Figure 5.3: **NACO K-band images of the central** $1 \times 1''$ **of the nuclear star cluster for May 2002 and August 2002.** *The astrometric position of Sgr A* is indicated by a cross with a 30 mas circle. The star next to Sgr A* is S2, which passed close to Sgr A* in spring 2002. Its high proper motion is clearly visible when comparing the images taken just three months apart.*

deconvolved images), we conclude that it is important to deconvolve images prior to establishing the astrometry.

- **Anisoplanatic effects.** The anisoplanatic patch is the angle subtended on the sky within which the image distortions caused by atmospheric turbulence are approximately uniform. The field-of-view of the May 2002 mosaic image is larger than the isoplanatic patch. This causes the PSFs of the stars to be asymmetric at distances greater than about $10''$ from the guiding star IRS 7. The PSFs are elongated and pointed toward IRS 7. We extracted five different PSFs by averaging the PSFs of several stars near the centre and near the four corners of the image, respectively (at distances $> 10''$ from IRS 7). The different PSFs are shown in Figure 5.4.The image was subsequently LR deconvolved with the different PSFs and the position of Sgr A* was determined after extracting the centroid positions of the maser stars. The pixel position of Sgr A* was found to vary by not more than 0.2 pixel (~ 5 mas) from its average position.

After quadratically combining the above errors, we concluded that the position of Sgr A* in the NIR image of May 2002 could be determined with an accuracy of about seven milliarc-seconds (mas). Since we saw in the section above that a second order transformation of the positions appeared to be adequate, our estimated error thus is a conservative upper limit. If we thus neglect the error of the order of the astrometric solution, the uncertainty of the position of Sgr A* is ≤ 5 mas. For comparison, Ghez et al. (2003a) obtain a similar accuracy (± 7 mas) for the position of Sgr A*.

5.3.2   Stellar Positions and Their Uncertainties

We do not only want to know the pixel position of Sgr A* on NIR images, but also the offsets in right ascension (RA) and declination (DEC) of the stars in the field from Sgr A*. Here, we examine what kind of errors might affect the astrometric positions of the stars.
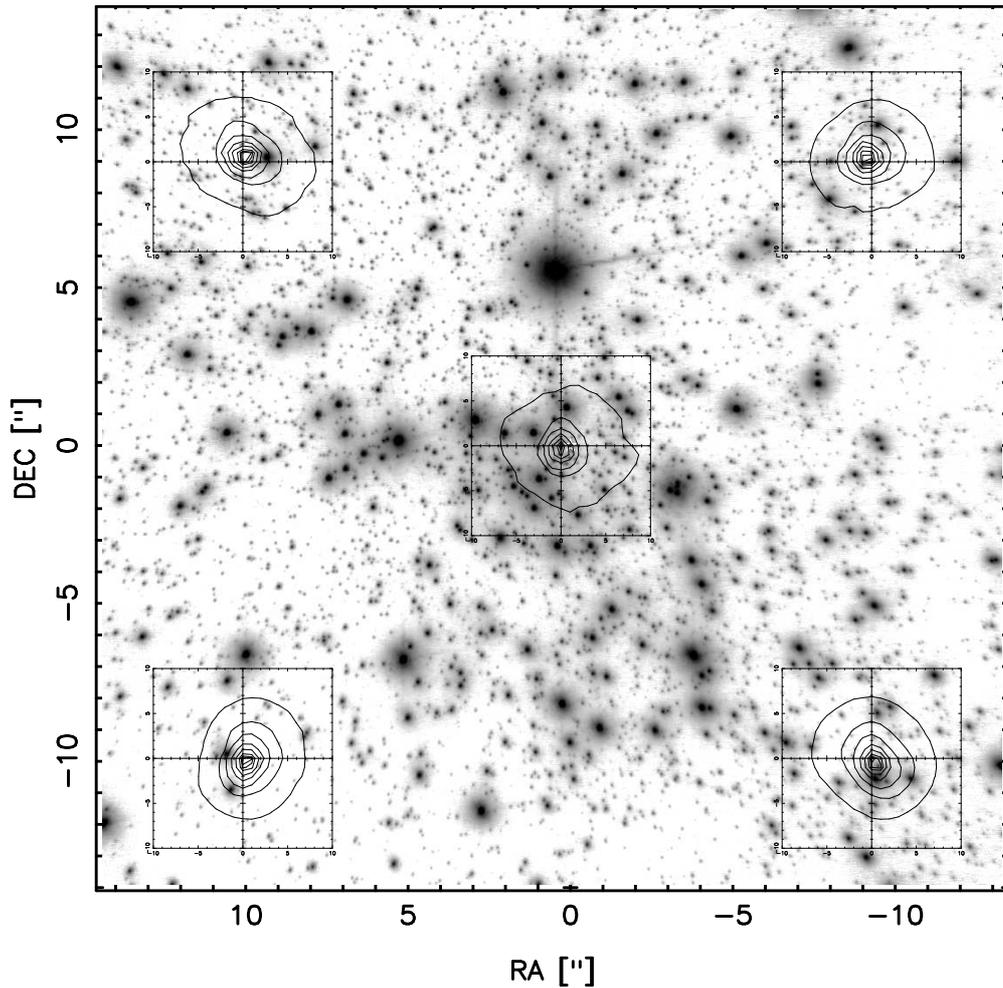
Figure 5.4: **PSFs extracted from the centre and from the four corners (at $> 10''$ distance from IRS 7) of the image shown in Figure 5.1.** *The PSFs of about ten stars were averaged for obtaining the average PSFs for the respective image regions. Contours are drawn at 1, 10, 20, 40, 60, 80, 90, and 95% of the peak flux. x and y coordinates are pixels with a pixel scale of $0.027''/pixel$.*

- **Order of the astrometric solution**. Using the positions of the seven maser stars, we calculated the parameters of the image transformation equations for a linear and for a quadratic solution. Subsequently, we created astrometric maps by calculating the offset from Sgr A* in RA and DEC for each image pixel. Maps of astrometric deviations were created by subtraction of these maps (linear minus quadratic) after correcting for systematic offsets (shifts) of 7 mas in RA and 1 mas in DEC. Figure 5.5 shows the deviations in RA and DEC at each pixel positions. While there can be offsets of the order ≥ 40 mas near the edge of the field, the deviations between the linear and the quadratic solution are not significantly larger than about 10 mas across most parts of the field. In fact, from a comparison between the focus of the orbit of the star S2 with the origin of our astrometric system (i.e. the formal position of Sgr A*; see chapter 8), we know that the stellar positions in the centre of the field (i.e. near Sgr A*) cannot be offset by more

than a few milliarcseconds in each axis. Also, from the discussion above, we know that in spite of their small values at least some of the quadratic transformation terms are significant. This means that our analysis probably overestimates the uncertainties caused by the choice of the order of the transformation.

- **Deconvolution**. To estimate the influence of image deconvolution, we solved the astrometric equations up to second order for images deconvolved with the linear Wiener filter and with the LR method. We created maps with the RA and DEC offsets assigned to each image pixel and created a map of the deviations by subtraction and correcting for systematic shifts of 2 mas in RA and 1 mas in DEC. Figure 5.6 shows the possible deviations of astrometric positions across the field. They are below 5 mas for the entire image. As for a comparison with the positions on the SSA image (not deconvolved), we found that the distortions were of similar order, but that there were rather large overall offsets (of the order 10 to 20 mas), the cause of which could not be found. However, pure overall offsets do not pose any serious problem. Again, from the comparison of the radio astrometry (based on deconvolved images) to the position of Sgr A* based on the orbit of S2 (see chapter 8), we know that our astrometric system is of high accuracy.

- **Influence of anisoplanaticity.** We extracted five different PSFs by averaging the PSFs of several stars near the centre and near the four corners of the image, respectively (at distances $> 10''$ from IRS 7). The different PSFs are shown in Figure 5.4. The image was subsequently LR deconvolved with the different PSFs and stellar positions were determined. Maps were created as described above. The deviations of the astrometric positions between two such maps are shown in Figure 5.7. There were large systematic shifts between the maps (16 mas in RA and 66 mas in DEC), which were corrected before subtracting the two maps. After this procedure, the astrometric deviations were ≤ 20 mas within $\sim 10''$ of Sgr A* which is located near the centre of the image (note the larger field-of-view compared to the previously shown maps). The deviations between the astrometric maps created by deconvolution with PSFs extracted from other image regions were of similar order as the ones shown in Figure 5.7.

Taking all the described effects into account, we conclude that stellar astrometric positions relative to Sgr A* can be extracted with an accuracy of 10 to 20 mas within about $10''$ of Sgr A*. For large field-of-views, deviations may become significant, i.e. larger than ~ 50 mas. In order to achieve a higher accuracy in the astrometry across a large field-of-view, one needs to know the radio positions of more maser stars, preferentially distributed evenly across the FOV.

5.3.3   Astrometry with a Different Reference Epoch

On May 10th, 2003, K-band imaging data were taken with NACO that had a comparable FOV and a better quality (less detector noise, only the two brightest sources saturated) than the May 2002 images. We repeated the astrometry measurements with the maser stars on this 2003 image and concentrated on examining possible anisoplanatic effects.

Again, we used five different PSFs for deconvolution that were extracted from the centre and from the four quadrants of the image. Subsequently, we determined the position of Sgr A* in the resulting five deconvolved and beam restored images, using the positions and proper motions of the seven maser stars as given in Table 5.1. Pixel positions of the masers were determined by measuring their centroids (extracting their positions with *StarFinder* lead to very similar results). The position of Sgr A* in all five cases was coincident within ≤ 0.1 pixel (< 3.0 mas). The proper motion of one of the maser stars (IRS 17) is not known (see Table 5.1). Therefore, we compared the positions obtained by using all seven maser stars to the positions obtained by using just the six masers with known proper motions. The agreement between both cases was again better than 0.1 pixel.
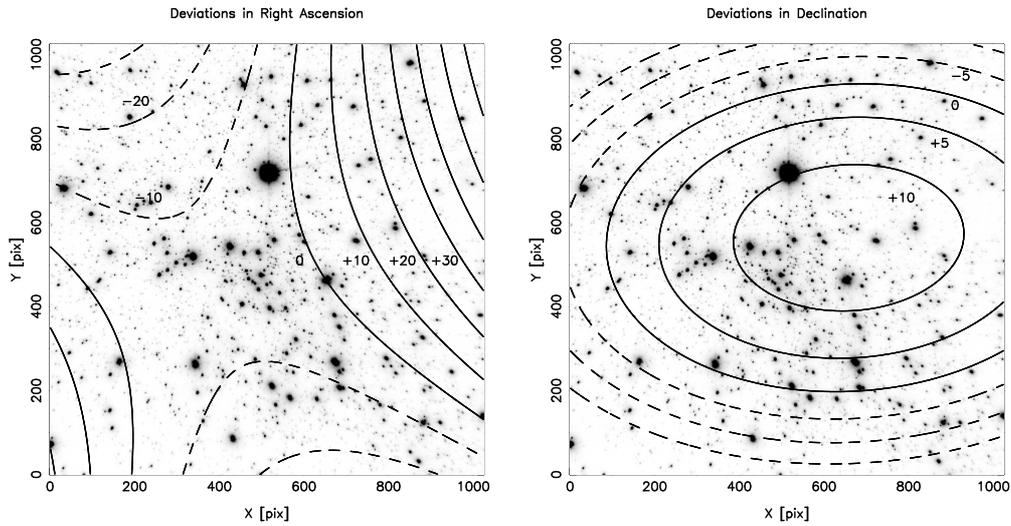
Figure 5.5: **Influence of order of astrometric solution on astrometry.** *Deviations of astrometric positions in RA and DEC between an astrometric solution that takes only linear terms into account and one that uses also quadratic terms. The pixel positions of the image were transformed to offsets from Sgr A* in right ascension and declination. The resulting position maps were subtracted (linear minus quadratic) and corrected for systematic shifts (7 mas in RA, 1 mas in DEC) in order to show the astrometric distortions between the two solutions at different pixel positions of the image.*
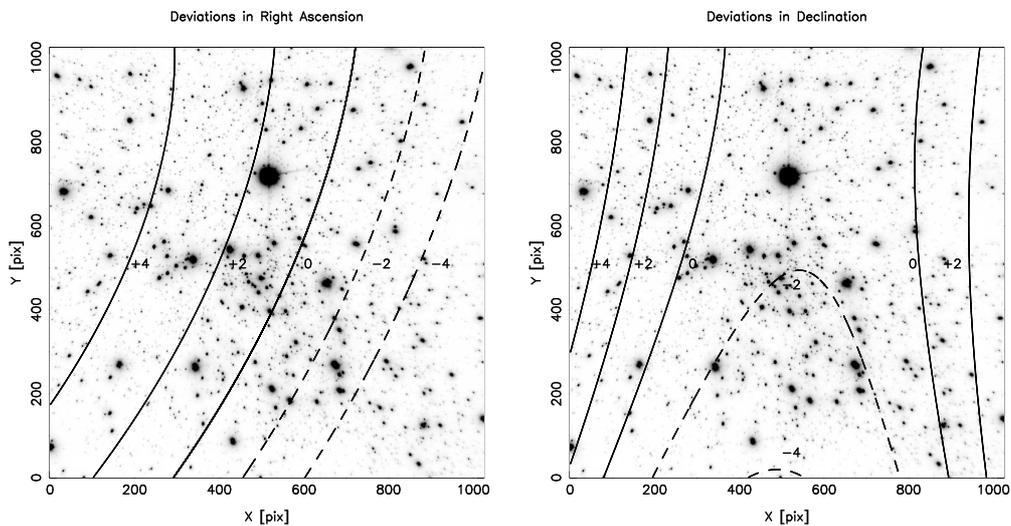
Figure 5.6: **Influence of deconvolution on astrometry.** *Deviations of astrometric positions in RA and DEC between an astrometric solution of the linear deconvolved and the LR deconvolved image. The pixel positions of the image were transformed to offsets from Sgr A* in right ascension and declination. The resulting position maps were subtracted (linear minus quadratic) and corrected for systematic shifts (2 mas in RA, 1 mas in DEC) in order to show the astrometric distortions between the two solutions at different pixel positions of the image.*

Deviations in Right Ascension   Deviations in Declination
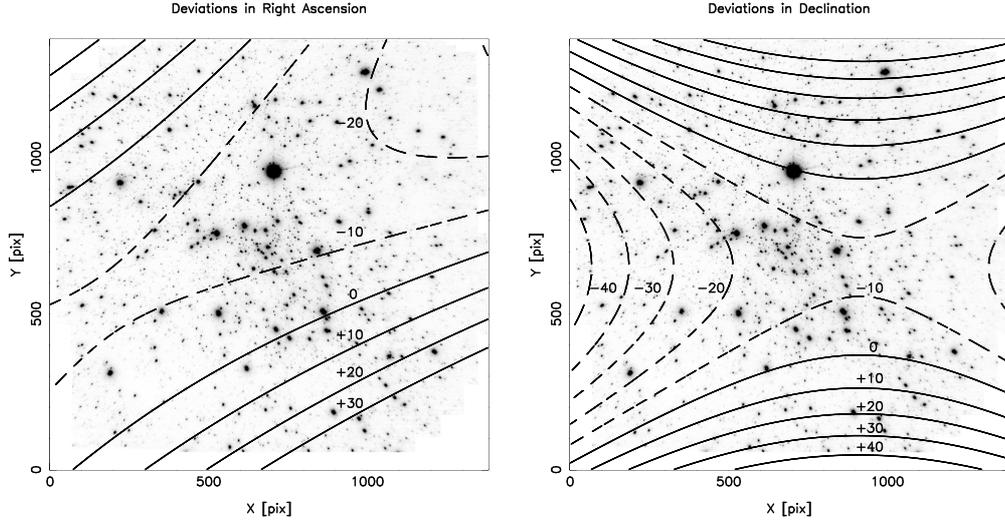
Figure 5.7: **Influence of anisoplanasy on astrometry**. *Deviations of astrometric positions in RA and DEC between images that were deconvolved with PSFs that were extracted from different regions of the field-of-view. The pixel positions of the image were transformed to offsets from Sgr A* in right ascension and declination. The resulting position maps were subtracted (linear minus quadratic) and corrected for systematic shifts (16 mas in RA, 65 mas in DEC) in order to show the astrometric distortions between the two solutions at different pixel positions of the image.*

Also, when creating maps of the deviation of stellar positions between the different deconvolved images across the FOV, we found relative deviations of similar magnitude than in Figure 5.7, i.e. deviations of ≤ 20 mas within $10''$ of Sgr A*. We concluded that anisoplanatic effects at the 2003 epoch were not more important than in the 2002 epoch. As a caveat, one should take into account that seeing conditions (seeing and anisoplanatic angle) appeared to be similar at both epochs. A more comprehensive data base of images with a large FOV (to include the maser stars) at different epochs under varying seeing conditions is needed for a more general statement on the influence of anisoplanasy on astrometry.

When comparing the offsets of individual stellar sources from Sgr A* (e.g. S2 and S8), as determined by the astrometry for the May 2003 epoch with the maser stars, to their positions for the May 2003 epoch that were obtained with the astrometry based on the May 2002 epoch (as described in chapter 7), we found an overall offset of the order 12 mas south in declination. Since the offset was largely consistent for all five images (i.e. the images obtained after deconvolution with the different PSFs), we suppose that the offset is not caused by anisoplanatic effects. A possible source of error might be that the proper motions of the maser stars are not known well enough, but generally, the reason for the discrepancy stays unclear. However, as long as the relative positions of the stars remain within the usual errors, an overall offset is no serious problem and can easily be corrected for.

5.4 Astrometric Positions for All Epochs, Stellar Velocities

Ott (2003) describes how he extracted stellar positions and proper motions from SHARP and NACO GC imaging data at epochs between 1992 and 2002 by using the May 2002 NACO image as a reference image. Briefly stated, the positions of the stars identified in an image of a

given epoch were transformed by a second order transformation onto corresponding positions in the reference image, in our case May 2002, which has a known astrometry. Ott (2003) used about 50 to 200 stars for determining the transformation parameters. Therefore, the transformations between different epochs were of great accuracy.

When using this method to measure astrometric positions in the SHARP 1995 imaging data, it was found that Sgr A* was located about 40 mas east of the position given by Menten et al. (1997). This is in good agreement with measurements of the Sgr A* position by Ghez et al. (2000) and Eckart et al. (2002), who used stellar accelerations for determining the location of Sgr A* and also found a position a few tens of milliarcseconds east of the position given by Menten et al. (1997). The reason for this discrepancy is most probably that there were some image distortions in the SHARP camera. Since Menten et al. (1997) could only use two maser stars for establishing the position of Sgr A*, they could not take image distortions into account.

Once stellar astrometric positions have been established for several epochs, the proper motions of the stars can be determined, i.e. the motions of the stars as they appear projected onto the plane of the sky. In order to accurately measure stellar positions and proper motions for each epoch, this method relies on the crucial assumption that the average motion of all the stars used for the image transformations are isotropic. Only in that case they will cancel out and give accurate results. Generally, the assumption of isotropy of the GC stellar cluster is assumed to be true. It can be tested by using spectroscopically measured stellar velocities. At least the late-type stars appear to be characterised by an intrinsic isotropic velocity dispersion (e.g. Sellgren et al., 1990; Genzel et al., 2000, 2003). Reid et al. (2003) showed that the average proper motion of the seven SiO maser stars (Table 5.1) as derived from the radio observations is close to zero, with an error of about 1 mas/year, which corresponds to about 40 km/s at the Galactic Centre. This provides additional evidence that the assumption of an average zero velocity of the GC stellar cluster projected onto the sky is justified.

In the previous section we examined possible astrometric distortions of our reference image from May 2002. Can such distortions affect the measured proper motions of stars? We saw that, even in the worst cases, the image distortions have gradients of the order $\leq$ 10 mas/100 pixels. A star with a proper motion velocity as high as 1000 km/s moves by roughly one pixel each year. So the error on its position introduced by the combination of its proper motion with the possible image distortions is smaller than 0.1 mas yr^{-1} or 4 km/s. The error will be smaller for slower stars. We conclude that the uncertainties of measured proper motion velocities due to image distortions that were not corrected properly are negligibly small. This means that stellar velocities can be measured across the whole available FOV.

5.5   Mapping out the S27 Camera of CONICA

We used the NACO GC imaging data from May 2002 and another similar data set from May 2003 in order to map out the pixel scales of the CONICA detector with the S27 camera. Both data sets consist of series of K-band images with the S27 camera, with each image having a total integration time of about 60 s. Each image covers a different section of the stellar cluster because random jittering was applied with a jitter box of $\sim 10''$.

We identified the maser stars in each image and extracted their pixel positions. With the radio astrometric positions and proper motions from Table 5.1 we calculated the radio position of each of the maser stars at the given epoch. Using pairs of two maser stars we could thus measure the pixel scales on several hundred base lines across the CONICA detector chip. We show the results of this experiment in Figure 5.8. On the left hand side of the plot we show histograms of the distribution of measured pixel scales. On the right hand side we assigned the measured pixel scales to the midpoints of the corresponding base lines on the chip. The midpoints are marked with squares when the pixel scale is more than 1σ larger than the average pixel scale, with circles when the pixel scale is more than 1σ smaller than the average pixel

Data set	Pixel scale mas/pix	Error mas/pix
May 2002	27.035	0.053
May 2003	27.034	0.090
All	27.035	0.074

Table 5.3: *Average pixel scales of the CONICA S27 camera, measured using SiO maser star radio positions and the pixel positions of the corresponding stars on May 2002 and May 2003 K-band images of the GC.*

scale, and with filled diamonds else. The upper row in the Figure shows the results for the May 2002 data set (300 base lines), the middle row for the May 2003 data set (300 base lines), and the lower row for the combined data sets (600 base lines).

The distribution of the pixel scales closely follows a Gaussian distribution in all cases The pixel scales and errors agree very well between the data sets (see Table 5.3). The average pixel scale of the CONICA S27 camera is 27.04 ± 0.07 mas/pixel. The error corresponds to a 1σ deviation. This means that the total astrometric error for positions measured relative to each other on the chip is $\leq 0.1''$, if one chooses the largest base line, that is the diagonal across the chip.

As for the distribution of pixel scales on the chip, it appears to be fairly homogeneous. No unambiguous evidence for a trend can be seen. Deviations from the average pixel scale are more frequent near the right and lower edges of the detector. This might hint at some image distortion. However, the measurement of these pixel scales all involved the maser source and bright supergiant IRS 7. It is heavily saturated on all images and might deteriorate the accuracy of the measured pixel scales. More measurements are needed in order to characterise the properties of the S27 camera more thoroughly. Generally, we conclude that the instrument produces very small image distortions and is ideal for high precision astrometry.

5.6   Extracting Stellar Positions from NIR Images

After an astrometric reference system has been established, measuring stellar positions in the GC cluster involves

- a) extracting the exact pixel position of a star in a given image

- b) converting the pixel position into offsets from Sgr A* in right ascension and declination.

Both steps are bound to produce a certain positional error. These errors were added quadratically in order to determine the overall error of a stellar position.

We extracted the pixel positions in images either by PSF fitting with the *StarFinder* program or by computing the centroid of a source within given apertures. Errors on the pixel positions were determined by comparing the differences in position between linear and LR deconvolved images or by using different aperture sizes.

In this work we concentrated on the central region of the star cluster around Sgr A* and usually produced high-resolution maps of just a few arc seconds FOV. These maps contained a few tens of bright to moderately bright sources that could be easily observed with SHARP/NTT. We decided to base the astrometry of these maps on the astrometric positions and proper motions of $10 - 20$ stars as determined by Ott (2003), which are based on the astrometric solution presented in this chapter. Since we can calculate the exact astrometric position of these sources for the image of a given epoch, we can subsequently determine the astrometry
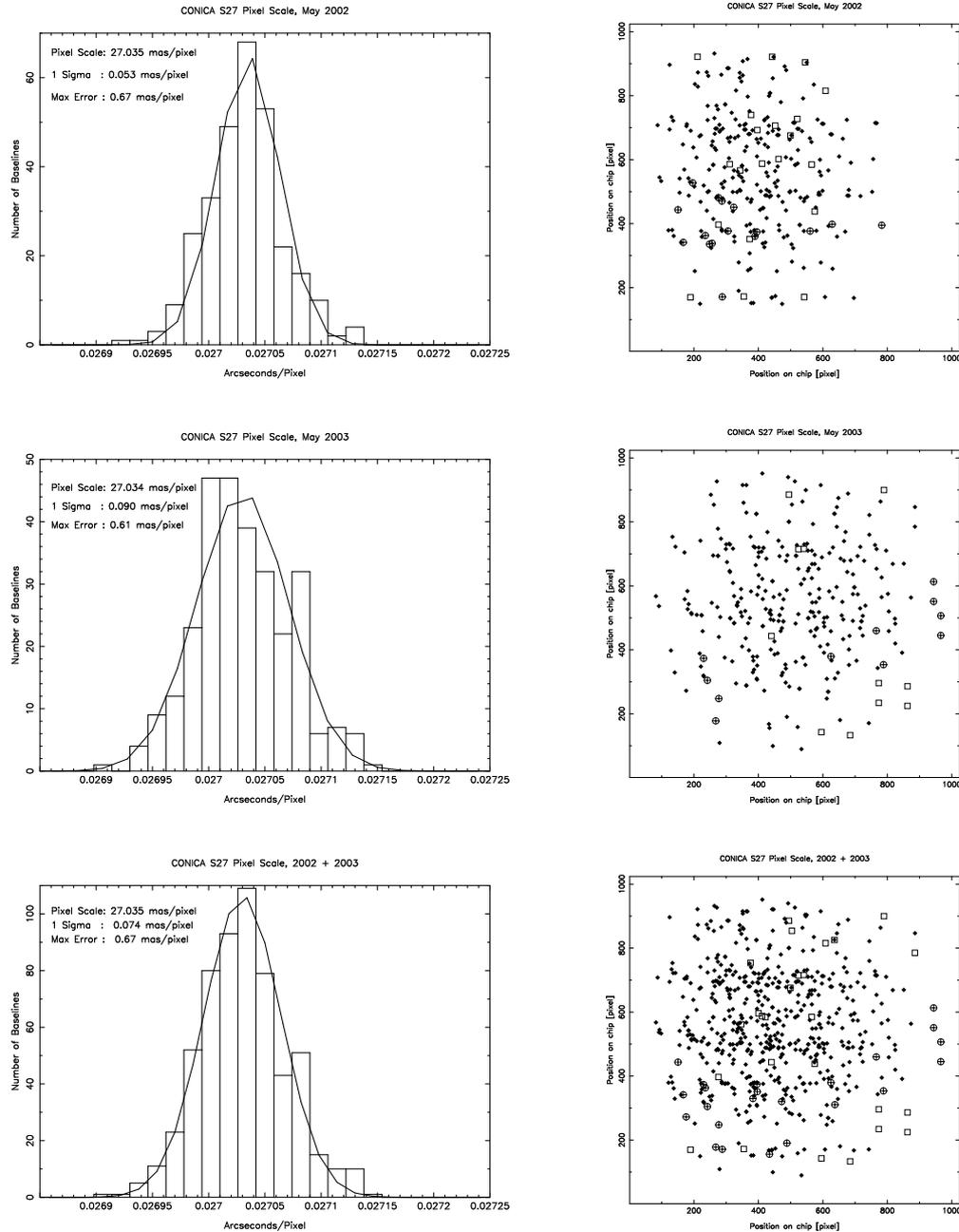
Figure 5.8: **Pixel scales of the CONICA detector with the S27 camera**. *On the left hand side of the plot we show histograms of the distribution of measured pixel scales. On the right hand side we assigned the measured pixel scales to the midpoints of the corresponding base lines on the chip. The midpoints are marked with squares when the pixel scale is more than 1σ larger than the average pixel scale, with circles when the pixel scale is more than 1σ smaller than the average pixel scale, and with filled diamonds else. Upper plots: pixel scales in the May 2002 data set; middle: pixel scales in the May 2003 data set; bottom plots: pixel scales in the combined data set.*

of the remaining sources as described by equations 5.1. By choosing random subsets out of the $10 - 20$ reference stars for the transformations we obtained average astrometric positions and corresponding errors for all sources in a given image.

The pixel position errors and the astrometric errors were usually of the same order. For stars of brightness $M_K \sim 15$ the combined errors for their position at a given epoch amount to ~ 5 mas for SHARP/NTT data and to $1 - 2$ mas for NACO/VLT images.

The question remains of how tightly our reference frame is tied to the central object Sgr A*. The average error in the velocity components of the astrometric reference stars is approximately 26 km/s. They are tied to about 50-200 stars of the stellar cluster surrounding the putative central black hole Ott (2003). The best estimate for the error in the relative motion of our reference frame with respect to the stellar cluster (dynamical centre of $50 - 200$ stars) is ± 8.2 km/s in RA, and ± 8.4 km/s in DEC. We further assume that the stellar cluster is gravitationally bound to the black hole, and that the velocity of the central object, which dominates by far the gravitational potential, is close to zero in this reference frame. We thus expect that the relative motion of our reference frame relative to SgrA* is less than ± 8.2 km/s in RA, and ± 8.4 km/s in DEC. This corresponds to roughly 0.25 mas/yr in both axes (see Eisenhauer et al., 2003). This possible systematic error was not taken into account in our analyses of stellar proper motions in the central cluster. In the worst case (epoch 1994, 8 years time difference to reference epoch 2002), this might introduce an additional positional error of the order 2.5 mas.

Chapter 6

The Cusp of Stars Around Sagittarius A*

In this chapter we will concentrate on the number density distribution and K-band luminosity function of the stars in the GC stellar cluster. Both the density distribution and luminosity function provide critical constraints on the dynamics and evolution of the cluster. Theoretical considerations and models predict the existence of a stellar cusp, i.e. a peak of the stellar density, in a dense star cluster surrounding a supermassive black hole (Bahcall & Wolf, 1976, 1977; Young, 1980; Murphy, Cohn, & Durisen, 1991). The stellar population in such a cusp may be distinct from the population of the surrounding cluster on large scales because processes such as mass segregation and stellar collisions may work very effectively in the dense environment of the cusp. We used deep, high-resolution NACO/VLT observations of the GC, taken during NACO science verification in August 2002 to investigate these questions. Most of the Text and Figures in this chapter have been taken from Genzel et al. (2003).

6.1 Stellar Number Counts and Photometry

6.1.1 Observations and Data Reduction

The observations used for the analysis in this chapter were carried out during science verification with the NAOS/CONICA adaptive optics system/near-infrared camera at the unit telescope 4 (Yepun) of the ESO VLT in Paranal, Chile. H-band (1.65μm) and K_s-band (2.16μm) imaging data were taken on August 29, 2002. Seeing was between $0.5''$ and $0.6''$. The infrared wavefront sensor of NAOS was used to close the feedback loop on the bright supergiant IRS 7 $\sim 5.5''$ north of Sgr A*. The detector pixel scale was $0.0132''$/pixel. The diffraction limited resolution was 40 and 55 mas FWHM in H and K, respectively. The oversampling helped to reduce the saturation of the numerous bright sources in the nuclear cluster. The detector integration time was 15 s. Four individual exposures were combined by a pipeline into one image of 60 s integration time. 25 such images were taken in the H band and 20 in the K_s-band. The individual images were flat-fielded, sky-subtracted and corrected for dead/bad pixels. The final frames were co-added with a simple shift-and-add (SSA) algorithm to final images of 1200 s (K-band) and 1500 s (H-band) total integration time. The Strehl ratio measured on individual sources near the guiding star was $\sim 50\%$ in the K_s-band and $\sim 33\%$ in the H band. Dithering between the exposures resulted in an FOV larger than the $14 \times 14''$ provided by CONICA with the finest pixel scale. From the final mosaic we selected a $\sim 9'' \times 9''$ region with the highest S/N-ratio, approximately centred on Sgr A*. There were numerous ($\sim 40-50$) bright ($K_s < 12$) stars in the FOV, which were strongly saturated in the K_s-band image. Saturation was less severe in the H-band image.

6.1.2 Source Identification and Photometry

In order to facilitate the identification of sources in the extremely dense nuclear stellar cluster and to reduce the influence of the seeing halos of the numerous bright stars, we deconvolved the images prior to number counts and photometric analysis. A PSF was extracted from the images by taking the median of several (more than 10 in the case of the K and H-band images) fairly isolated, bright, but not saturated stars. We deconvolved the images using two methods, a linear Wiener-filter technique (Ott et al., 1999), and the LR algorithm. The delta maps resulting from the LR deconvolution were re-convolved with a Gaussian PSF of the appropriate FWHM for the respective wavelengths. For comparison of the results of the different image processing techniques, Figure 6.1 shows the direct (SSA) image, and the Wiener-filtered/linearly deconvolved and the LR-deconvolved H-band images of the central $\sim 2''$ around the compact radio source Sgr A*. The agreement of sources identified with the different image analysis techniques is generally very good. Only within a few tenths of an arcsec of bright (mostly saturated) stars some deterioration is caused by artefacts such as ringing. In these regions, graininess of the seeing halo, ringing and streaks make source identification of stars 4 or more magnitudes fainter than the bright star unreliable.

We identified point sources and carried out photometry with the FIND procedure from the IDL Astrolib library. The IDL FIND procedure convolves the image with a Gaussian beam prior to searching for local maxima. We found that there was no ideal choice for this parameter. Depending on the exact value of the FWHM parameter, sources would be identified or missed in densely packed regions, while various spurious sources would be detected. We therefore decided to repeat the source detection (and completeness correction, see below) procedure three times, with different values of the FWHM parameter. For construction of the final source lists we compared the lists of sources from the LR and Wiener deconvolved images, eliminating sources that only showed up in one of the lists. For the remaining stars, their photometric values were averaged, with the error taken as the deviation of the two measurements from the average. Figure 6.2 shows plots of the photometric errors vs. magnitude. In regions not too close to bright stars, sources of 19th magnitude were $\sim 5\sigma$ above the background in the deconvolved K-band image, while the H -band image was about 1.5 magnitudes deeper. Spurious sources were detected in the seeing halos of bright stars. This problem was particularly important for the K-band, where numerous bright stars were strongly saturated. Deconvolution techniques also tend to create faint, spurious point sources. We therefore adopted a conservative approach by applying the constraint that genuine stellar sources must be present in both the H- and K-band image. We verified that this procedure effectively excluded spurious detections by comparing the maps of the identified stars with the actual images.

The final lists of sources comprised between 3200 and 4000 stars, depending on the choice of the FWHM parameter, with significantly different source counts only for sources with K$\geq$ 18. After correction for incompleteness (see below), however, the number counts at all magnitudes agreed very well. For the number counts of the luminosity function and of the surface number density presented in this paper, we chose the average of the counts resulting from the different choices of the FWHM parameter. For the errors, we combined quadratically the statistical counting (Poisson) error and the maximum deviation of the counts from their average, which corresponds to a $\sim$10% uncertainty at K$\leq$ 19. We calibrated the photometry in the H and K bands relative to sources in the cluster. The main limitation in identifying appropriate calibration stars resulted from finding stars that were not saturated, but bright enough to be included in the (Blum, Sellgren, & DePoy, 1996) list. Additionally, these stars should be fairly isolated because the Blum, Sellgren, & DePoy (1996) data were seeing limited. By considering these points we tried to minimise possible systematic errors in flux calibration. For the K-band image, we chose four isolated stars with magnitudes between 13 and 14 from the Ott (2003) list (IDs 412, 284, 265, and 239). For the H-band photometry we used the Blum, Sellgren, & DePoy (1996) photometric value for IRS 33N (named IRS A11 in their list). Another point to keep in mind is that the Blum, Sellgren, & DePoy (1996) data were taken in the
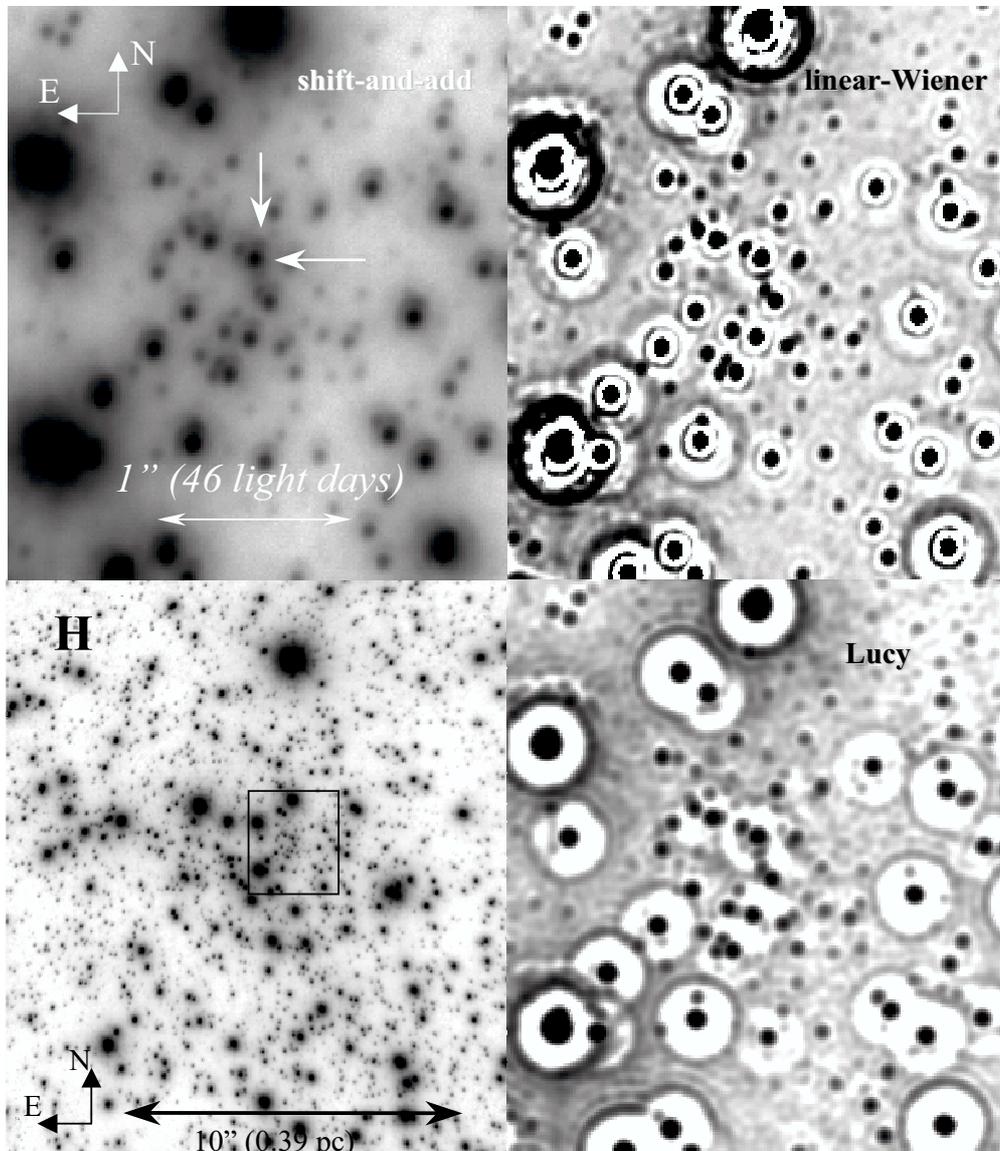
Figure 6.1: **NACO H-band band image of the GC stellar cluster: Comparison of deconvolution techniques.** *The lower left panel shows the August 2002 H-band image of the GC stellar cluster. The upper left panel shows an SSA-image of the central $\sim 2''$ of the cluster around Sgr A*, while the upper right panel shows a linearly deconvolved, and the lower right panel an LR deconvolved and beam restored image of the same region. The same faint sources in crowded regions can be reliably detected in both deconvolved images. Rings around brighter sources are artifacts of the deconvolution techniques.*
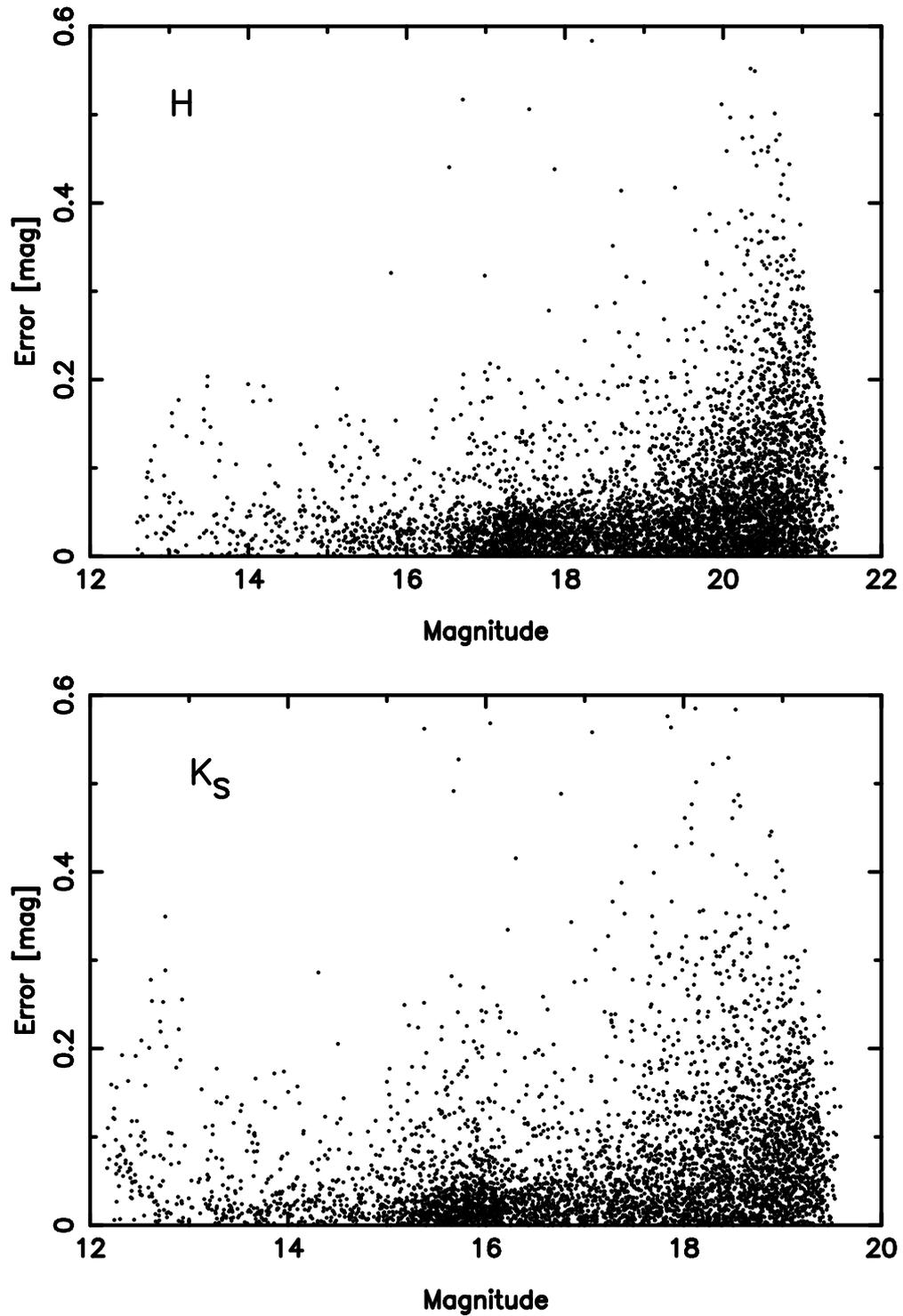
Figure 6.2:   **Photometric error vs. magnitude for H and K-band images.** *Photometric errors (in mag) as a function of magnitude as determined from a comparison of the photometry obtained on LR and linearly deconvolved H (top) and K-band (bottom) images.*

K_{inp}	K_{recov}	σ	Completeness [%]
13	13.05	0.03	99
14	14.04	0.05	98
15	15.04	0.07	95
16	16.04	0.09	88
17	17.04	0.11	79
18	18.01	0.17	63
19	18.91	0.22	32
20	19.76	0.23	4

Table 6.1: **Completeness of the NACO August 2002 K-band image at different magnitudes.** *Average magnitude of recovered sources, sigmas of average magnitudes and overall completeness for given magnitudes.*

K-band, while the observations presented in this paper were made with a K_s band filter. We estimate the resulting relative uncertainties of our photometry to be less than 0.1 mag at K$\leq$ 18 (H$\leq$ 19), while the absolute photometry is uncertain by 0.15 mag in H and K.

6.1.3 Incompleteness Correction

We determined the incompleteness correction for the K-band images with the well known technique of first adding and then again recovering artificial stars. Taking the same PSF as used for deconvolution, we inserted artificial stars randomly into the original stellar field. The image containing the artificial stars was Wiener deconvolved, followed by source identification with the FIND procedure. We did not repeat this procedure with an LR deconvolution because of the enormous amount of computational time needed for this method. The artificial stars were spaced at intervals of $0.5''$, such that their individual PSFs did not interfere with each other. By repeating the same procedure many times with different positions for the artificial stars, we probed the image in a dense $\sim 0.13'' \times 0.13''$ grid. We recorded in completeness maps the probability of recovering a source within $\leq \pm 0.5$ mag of the input magnitude at a given position. As an example, the completeness map for stars of 18th magnitude in the K-band image is shown in Figure 6.3. Its spatial structure of course reflects the distribution of bright stars as it can be seen in the lower left panel of Figure 6.1. Table 6.1 gives the overall completeness as well as the average magnitude and standard deviation of the magnitude of the recovered artificial stars for each magnitude interval. We determined the completeness corrections for all three choices of the FIND FWHM parameter that were used to create the source lists.

6.1.4 Number Counts and K-Luminosity Function

We computed surface number densities by counting the stars in annuli with increasing radius around Sgr A*. We corrected these number counts by dividing by the appropriate incompleteness at that radius and magnitude. In order to avoid completeness corrections significantly larger than a factor of 2 in the innermost annuli, where completeness and number counts are low for faint stars, we only used stars with K-magnitudes brighter than 17 for this analysis. In a second analysis we counted stars within ~ 1" of Sgr A* by eye in the Lucy-Richardson deconvolved H-Band image. This region is devoid of bright stars and the H-band image has the advantage of lower confusion. From the source counts, we also constructed completeness corrected overall K-band luminosity functions (KLFs) for the circular regions within 1.5" and within 9" of Sgr A*.
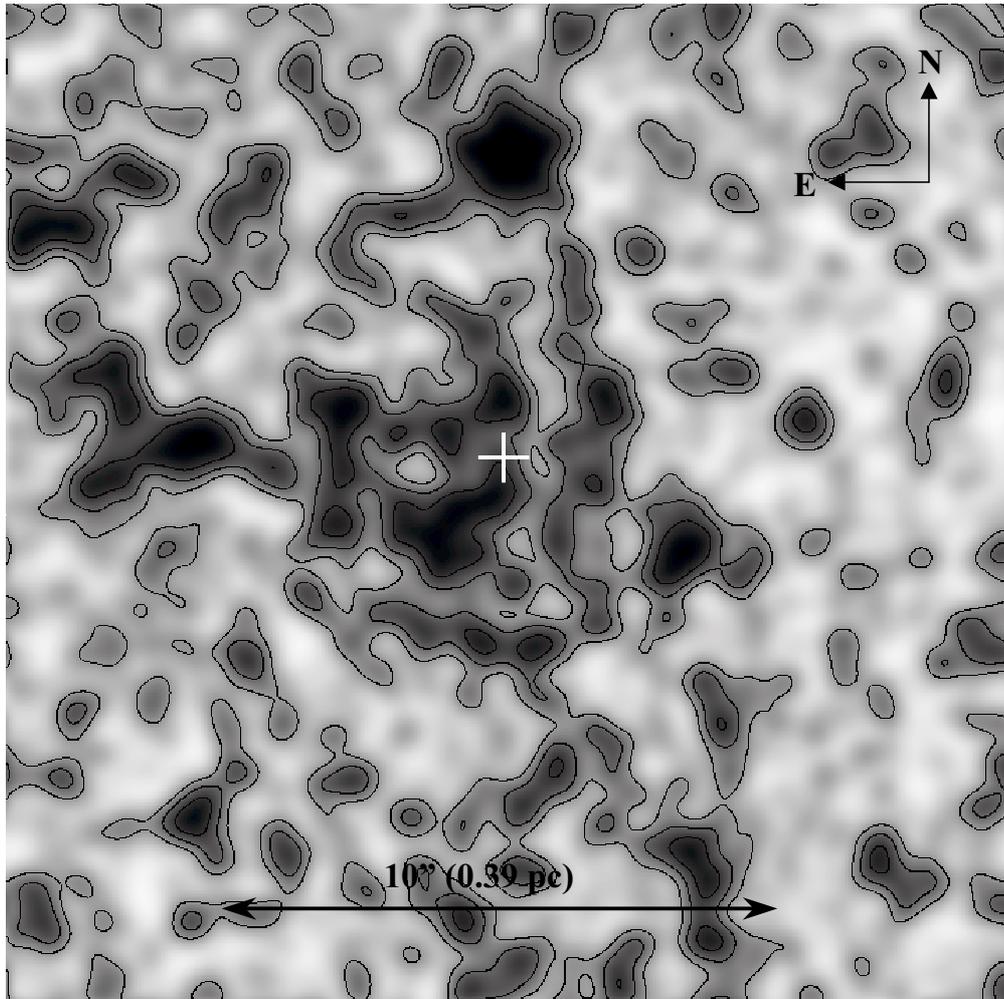
Figure 6.3: **Completeness map of the K-band image at K**= 18**.** *The map shows the probability of recovering an artificial star of magnitude* K = 18 *with an error of* ≤ ±0.5 *mag at a given position in the image. Dark areas indicate the lowest probabilities. The contours outline the 20, 40, and 60% probability levels. Dark areas are dominated by bright stars that make the detection of faint stars in their surroundings difficult.*

6.2   The Central Stellar Cusp

Figure 6.4 is a plot of the binned, stellar surface density distribution of stars as a function of projected separation from Sgr A*. As described in section 6.1.3, we have corrected the observed K≤ 17 counts for incompleteness. For the higher resolution H-band data we plot the observed H≤ 19.8 counts since the incompleteness correction in the central 1.5″ is small and does not significantly vary with position. We also have determined distributions to fainter levels (K≤ 18), with very similar results. However, the incompleteness corrections at those fainter levels become large near the centre and dominate the error budget. The most reliable results are obtained for the magnitude limits taken in Figure 6.4. For extrapolation to larger radii we combined the NAOS/CONICA data with shallower (K≤ 15), but wider field NTT/SHARP number counts (Genzel et al., 2000), appropriately scaled for the best match with the deeper NAOS/CONICA data in the overlap region. The stellar counts for projected distances $p(\text{Sgr A}*) \geq 5 - 10''$ can be reasonably well fit by a flattened isothermal sphere of core radius $\sim$ 0.3 pc (Genzel et al. 1996 and references therein). Within a few arcseconds the new data clearly indicate an excess of faint stars above that of a flat core, already suggested by the earlier SHARP/NTT and Keck data (Eckart et al., 1995; Alexander, 1999). The surface density of faint stars increases with decreasing separation from the radio source. The smoothed, two dimensional distribution of faint stars in the H and K-images (Figure 6.5) visually confirms the existence of this 'cusp' and shows that it is centred on Sgr A* [$(\Delta\text{RA}, \Delta\text{Dec})=(+0.09", -0.15")$], with an uncertainty of ±0.2". This is in contrast to the near-IR light distribution, which is centred on the bright stars in the IRS16 complex. Our data thus resolve the 17 year old puzzle of why Sgr A* is offset from the 2μm emission peak (Allen & Sanders, 1986). The offset is caused by the bright stars in the IRS16 complex, and is not a property of the majority of the faint stars in the overall nuclear cluster.

Following Alexander (1999) we have analysed the surface number density distribution in Figure 6.4 with a broken power-law stellar density distribution, with the simultaneous constraint that the (stellar) dynamical mass is 3.2, 8.4 and $27.3 \times 10^6 M_\odot$ at distances $R = 1.9$, 3.8 and 11 pc from Sgr A* (subtracting from the mass distribution of Genzel et al. (1996) a $2.8 \times 10^6 M_\odot$ central point mass). The resulting fit shown in Figure 6.4 has the following parameters,

$$\rho_\star(R) = 1.2 \times 10^6 \left(\frac{R}{10''}\right)^{-\alpha} \ [M_\odot\text{pc}^{-3}], \qquad (6.1)$$

with $\alpha = 2.0 \pm 0.1$ at $R \geq 10''$, and $\alpha = 1.4 \pm 0.1$ at $R < 10''$. We have also generalised the Maximal Likelihood (ML) analysis of the cusp's slope (Alexander, 1999) to take into account the incompleteness corrections. Because the radius of the extracted NAOS/CONICA field ($\sim 8''$) is smaller than the break radius of $10''$ indicated by the NTT/SHARP data, an ML analysis of the NAOS/CONICA data alone cannot be used for a reliable determination of the parameters of the outer power-law. An analysis of 856 stars in the inner $4''$, where the inner cusp dominates the total counts, indicates an inner power-law cusp with an exponent $\alpha = 1.3 \pm 0.1$, in very good agreement with our analysis of the binned data above. With these parameters the cusp's stellar density is $3 \times 10^7 M_\odot$ pc^{-3} at $R = 1''$, and $7 \times 10^8 M_\odot$ pc^{-3} at $R = 0.1''$. An alternative description of the data in Figure 6.4 may be a localised, Plummer-model like, cusp on Sgr A*, superposed on a larger-scale, isothermal cluster, with a distinct break in between (Mouawad et al., 2003). The present data cannot discriminate between these two possibilities but the estimated stellar densities are similar. The stellar mass contained in the cusp is estimated to vary as $1.3 \times 10^4 \left[\frac{R}{arcsec}\right]^{1.63} M_\odot$.

The analysis we just presented depends critically on the assumption that the ratio of number counts to total stellar mass (mostly in fainter, not directly observed stars) does not vary with radius and environment in the Galactic Centre. This assumption is almost certainly violated at some level, since we argue below that giant late type stars are destroyed and moderately massive stars are created by mergers of lower mass stars in the very dense inner region. However,
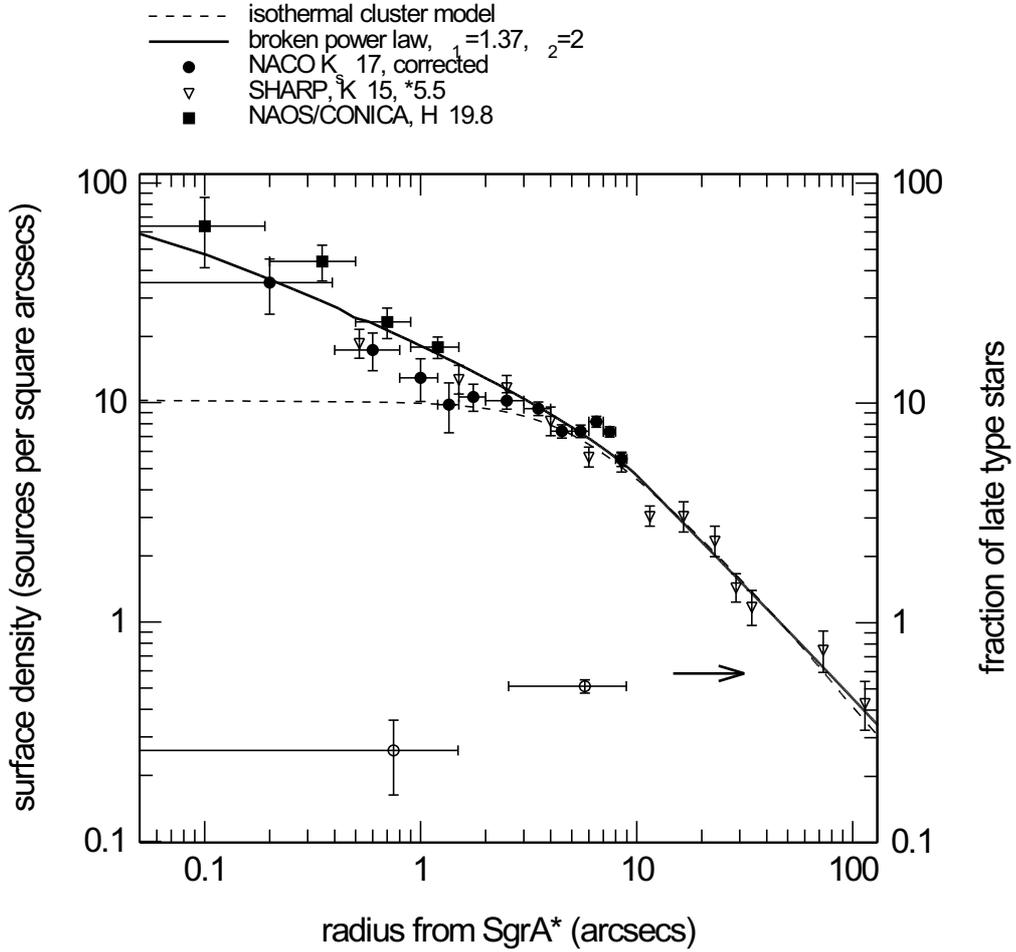
Figure 6.4: **Surface density of stars as a function of projected radius from Sgr A*.**
*Filled circles are NAOS/CONICA counts of all sources present on both H and K maps and
with K≤ 17, corrected for incompleteness by the artificial star technique. Squares with crosses
denote direct H-band NAOS/CONICA counts by eye to H≤ 19.8 near Sgr A*, a region devoid
of bright stars. Downward-pointing triangles denote the SHARP K≤ 15 counts from Genzel
et al. (2000), multiplied by a factor of 5.5 to best match the deep NAOS/CONICA counts in
the overlap region beyond a few arc-seconds from Sgr A*. The dashed curve is the model
of a flattened isothermal sphere of core radius 0.34 pc fitting the counts from SHARP data.
Note that at K∼ 15 the SHARP counts in the innermost region are only 50% complete. The
continuous curve is the broken power-law (α = 2 beyond 10″ and α = 1.4 within 10″)
discussed in the text. Open circles at the bottom of the figure denote the fraction of late type
stars of the total K≤ 15 sample with proper motions and Gemini CO narrow-band indices
(Genzel et al., 2003). All vertical error bars are ±1σ, and denote the total uncertainty due
to Poisson statistics and, where appropriate, due to incompleteness/confusion correction (∼
10%) in each annulus. Horizontal bars denote the width of the annulus.*
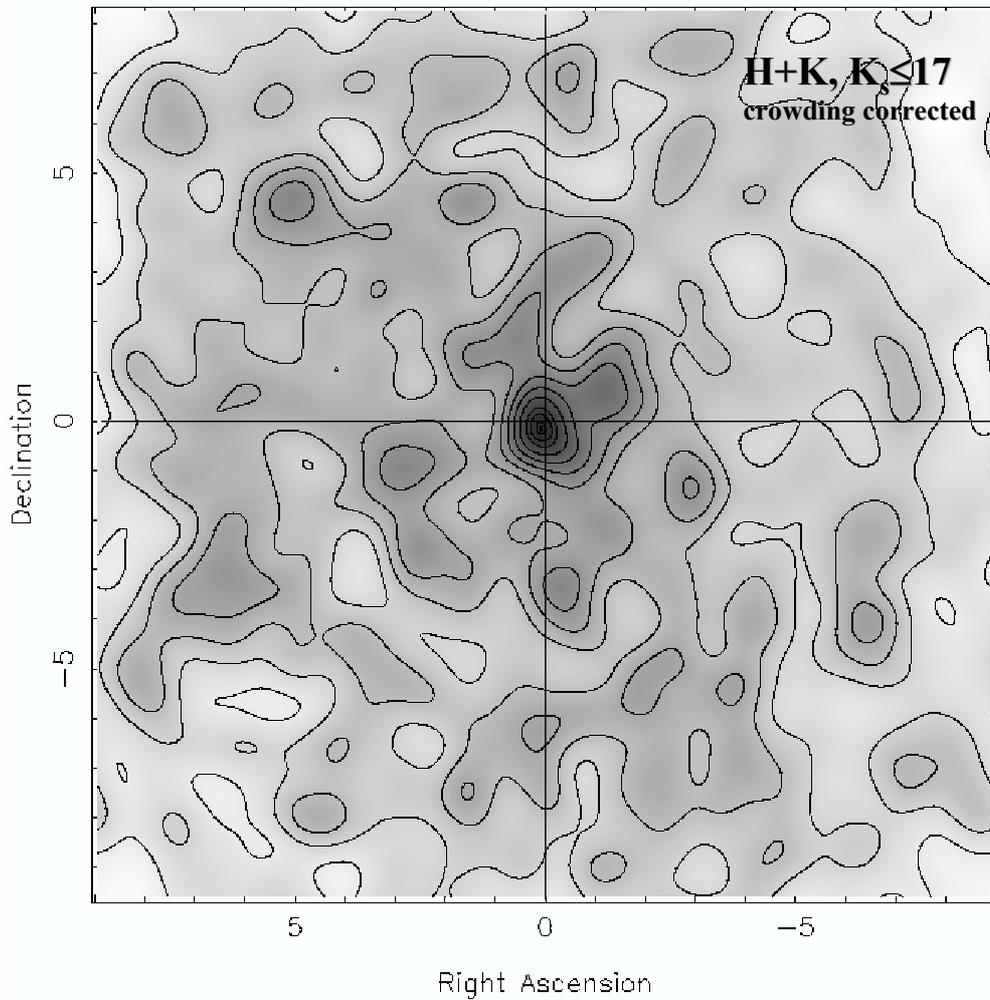
Figure 6.5: **Two-dimensional map of the smoothed surface density of the GC stellar cluster.** *Two-dimensional map (arc-seconds relative to Sgr A*) of the smoothed surface density of NAOS/CONICA sources present on both H and K maps corrected for crowding and incompleteness. For this purpose, the original source list maps of H+K sources in each magnitude bin between K of 13 and 17 were smoothed with a 1″ Gaussian and divided by the incompleteness map. The corrected maps of different magnitudes were then added. Contours are 10, 20,...,90, 95, 99 and 99.9% of the peak surface density. The maximum of the stellar density is at (RA,Dec)=(0.09″, −0.15″) relative to Sgr A*, with an uncertainty of ±0.2".*

we expect that these effects alter mostly the counts of the less numerous, brighter stars and not so much the fainter stars that dominate the counts. At the very least, the radial population changes make the values of the cusp density estimated above quite uncertain. Obviously, spectroscopic observations will be required for studying the properties of the fainter stars as a function of distance from Sgr A*.

Scoville et al. (2003) used Hubble space telescope images at $1.9\mu m$ to analyse the change of the surface brightness distribution of the GC stellar cluster with distance to Sgr A*. Contrary to our surface number density counts, they find a sharp drop-off of the surface brightness inside of $1''$ (see their Figure 12). We think that an alternative interpretation of their surface brightness distribution is, that they find an excess brightness at distances between $1''$ and $4''$. From our work, we know that the stellar population in the cusp differs from that in the overall cluster, which is marked e.g. by the lack of HB/RC stars in the cusp. One must also keep in mind that at distances between about $1''$ and $4''$ the luminosity of the cluster is dominated completely by bright giant stars in the IRS 16, IRS 33, IRS 29, and IRS 13 agglomerations. Scoville et al. (2003) tried to take this fact account by excluding the brightest $20-50\%$ of the pixels in their analysis. However, we feel that it is highly probable that a radial change in the stellar population (i.e. in the content of very bright stars) is responsible for the discrepancy between their results, which are based on lower angular resolution brightness surface measurements, and our results, which are based on higher angular resolution number density counts.

Keeping the caveat of the radially changing stellar population in mind, the observed stellar density distribution is consistent within the uncertainties with the predictions of theoretical models for a cluster of stars surrounding a massive central black hole. These models predict the formation of a power-law cusp. The expected radial slope of the power-law ranges between ~ 0.5 and ~ 2.5, depending on the cusp's formation scenario and on the importance of inelastic stellar collisions. Relaxed, single mass stellar cusps have a steep slope of $\alpha \sim 7/4$ (Bahcall & Wolf, 1976, 1977). Un-relaxed, initially isothermal clusters around an adiabatically growing hole have a shallower slope of $\alpha \sim 3/2$ (Young, 1980). In multi-mass, lower density cusps ($\rho_\star < 10^7\ M_\odot\ pc^{-3}$) the models of Murphy, Cohn, & Durisen (1991) also predict a steep slope ($\alpha \sim 7/4$), while higher density cusps ($\rho_\star \sim 10^8\ M_\odot\ pc^{-3}$) have flatter inner slopes due to the onset of stellar collisions ($\alpha \geq 1/2$). Adiabatic solutions (e.g.Young 1980), that assume that the black hole grows on a time scale that is short compared to the stellar relaxation time scale, do not apply to the Galactic centre, which is estimated to be relaxed (e.g. Alexander 1999) and where the growth time scale of the hole is long (~ 10 Gyr).

6.3   K-Band Luminosity Function of the Central Cluster

Figure 6.6 shows the K-band luminosity function (KLF) for the overall nuclear cluster (upper panel, $p < 9''$) and for the $p \leq 1.5''$ cusp region (lower panel). Figure 6.7 is a colour-magnitude plot of the same region. In both regions we have corrected the counts for incompleteness with the artificial star technique described in section 6.1.3, taking into account the effects of this correction on the error bars. The NAOS/CONICA data are in excellent agreement with the previous Keck and NTT data at the brighter magnitudes, and extend the KLF to our completeness limit of K~ 18. The Galactic centre KLF thus samples all giants and supergiants, as well as the main sequence to spectral type A5/F0 (2 $M_\odot$). Since the NAOS/CONICA counts are incomplete at the brightest magnitudes because of saturation effects, we have combined the NAOS/CONICA counts and the NTT counts to a common KLF shown in Figure 6.6, upper panel.

The overall KLF of the central $p < 9''$ (0.36 pc) region is described to first order by a power law ($d\log N/dK = \beta \sim 0.21 \pm 0.02$). In the range $14 \leq K_s \leq 19$ the overall KLF is similar to, but somewhat flatter than the KLF of the Bulge of the Milky Way several degrees from the centre ($\beta \sim 0.3$: Alexander and Sternberg 1999, Tiede et al. 1995, Zoccali et al. 2003), and the KLF on 30 pc scales around the centre (Figer, 2002). A $\beta \sim 0.3$ power-law is well
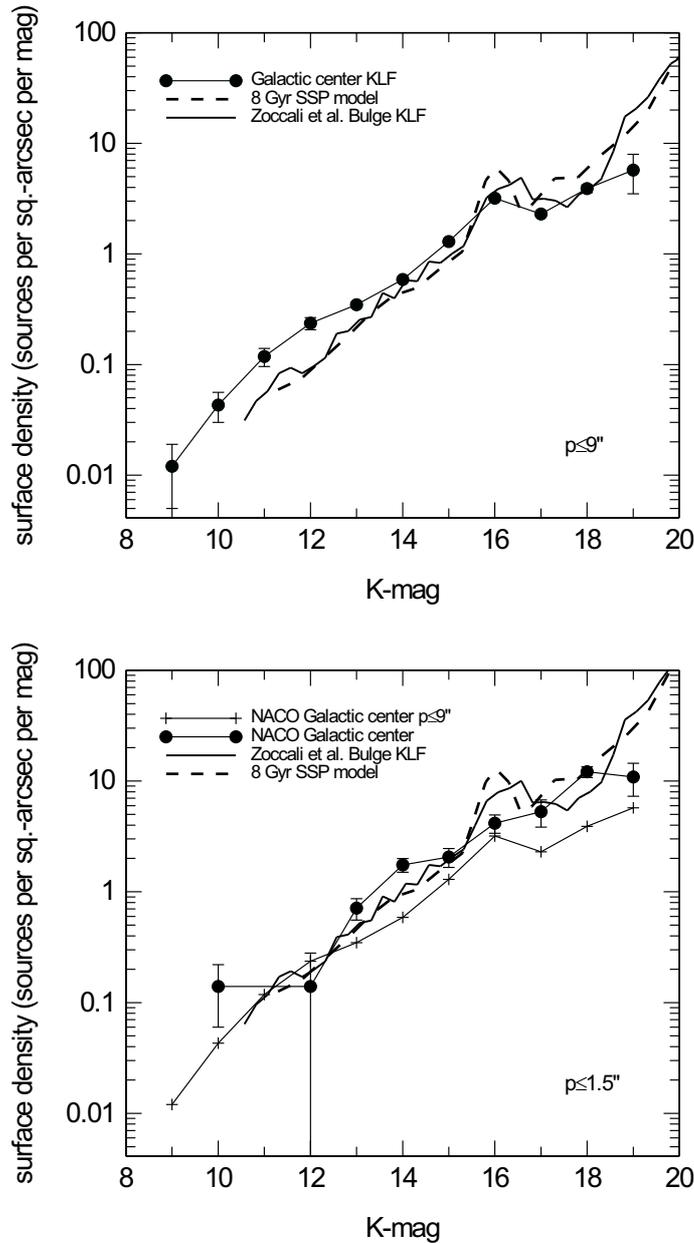
Figure 6.6: **K-band luminosity function of the GC stellar cluster.** *Upper panel: K-band luminosity function (sources per square arc-second per mag) of the central 9″ region (filled circles with 1σ error bars). The KLF points have been corrected for incompleteness as discussed in the text. Errors take into account both the Poisson error, as well as the uncertainty of the crowding/confusion correction (∼10%). The Galactic Centre data points are a combination of the new August 2002, NAOS/CONICA data (for K≥ 12) and of the SHARP/NTT data sets (Ott, 2003), scaled in the 12≤ K ≤ 14.5 overlap region for best match with the CONICA data. For comparison, the continuous curve is the KLF of the Galactic Bulge on scales of degrees and the dashed curve is a single age (8 Gyr) stellar population model of the bulge (from Zoccali et al. 2003), both scaled vertically to match the centre data, and corrected horizontally to the same K-band extinction. The prominent excess hump at K∼ 16 is due to old metal rich, low mass stars on the horizontal branch/red clump. Lower panel: K-band luminosity function (sources per square arc-second per mag) of the central cusp region (filled circles, projected distance to Sgr A* ≤ 1.5″,±1σ error bars). Other symbols and curves are as in the upper panel.*
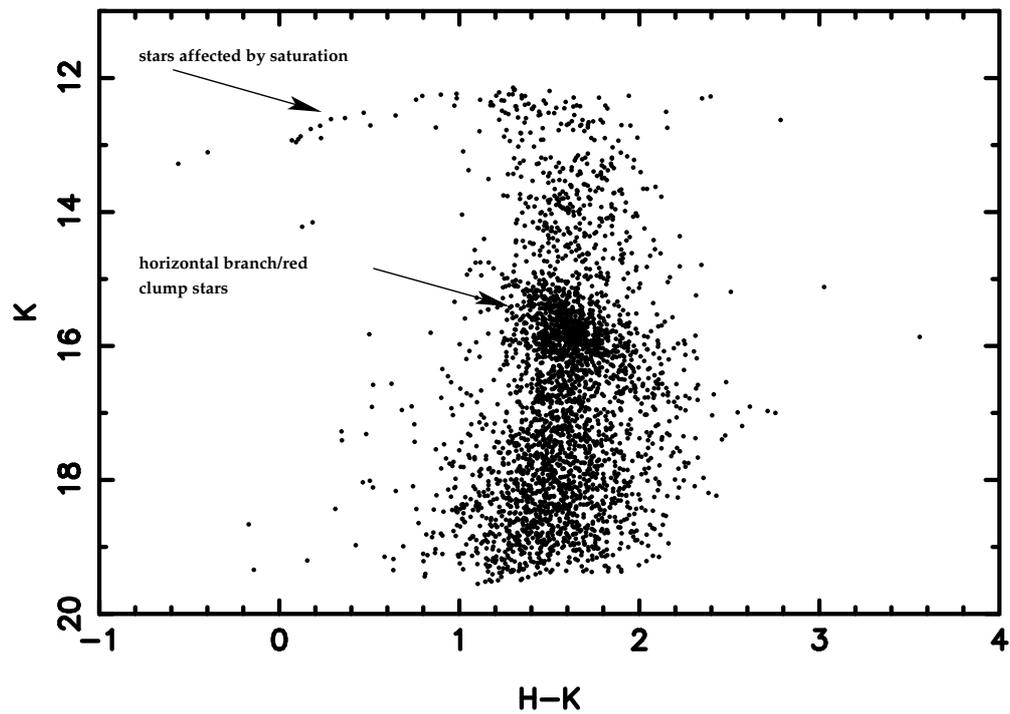
Figure 6.7: **Colour-magnitude diagram of the GC stellar cluster.** *Colour-magnitude diagram for the same* $p \leq 9$" *region as in Figure 6.6, again showing prominently the horizontal branch/red clump stars. Most of the very blue stars in the diagram at K< 13 are probably caused by saturation in the K-band image, which results in their K-magnitudes being underestimated.*

matched by the theoretical KLF of old stellar populations, which reflects the rate of evolution of individual stars along the red giant and asymptotic giant branches. The flatter slope of the Galactic centre KLF compared to the Bulge is mostly caused by an excess of the counts at K$\leq$ 14, by a factor 1.4 to 2. In agreement with earlier discussions (Lebofsky & Rieke, 1987; Blum, Sellgren, & DePoy, 1996a; Davidge et al., 1997), we attribute this bright-end excess to young, early and late type stars. In addition, the $p < 9''$ KLF shows a prominent excess hump centred at $K_s \sim 16$, a factor of two above the power law. This hump is prominent in the Bulge as well, and on 30 pc scales around the Galactic centre when all distributions are adjusted to the same GC extinction ($A_K = 3.2$; Rieke, Rieke & Paul 1989; Raab 2002). The excess can be attributed to old and metal rich, core He-burning horizontal branch (HB)/red clump (RC) stars (Tiede & Terndrup, 1995). These stars have characteristic masses of 0.5 to 0.8 M$_\odot$. The red clump stars can also readily be seen in the colour magnitude plot. The amplitude of the HB/RC excess relative to the numbers of giant stars, that make up the power law component, suggests that the Galactic Bulge on average has close to solar metallicity (Tiede & Terndrup, 1995). In fact, an old (~ 10 Gyr), single age (SSP) model with a bulge metalicity distribution deduced from the colour-magnitude properties of the Bulge gives a fairly good representation of the hump (dashed curve in Figure 6.6, from Zoccali et al. 2002). We thus conclude that the hump in the KLF at K$\sim$ 16 is most likely caused by the presence in the innermost parsec of such old low mass, and metal rich stars. The overall KLF of the Galactic centre thus is dominated by an old cluster with an admixture of bright young stars, in excellent agreement with the spectroscopic information collected over the past decade (e.g. Lebofsky & Rieke, 1987; Krabbe et al., 1995; Blum et al., 1996).

The KLF of the $p \leq 1.5''$ cusp region (lower panel in Figure 6.6) appears to be a featureless power-law. It has a similar slope as the integral KLF ($\beta = $ d log N/dK $\sim 0.21 \pm 0.03$) but the K$\sim$ 16 HB/RC hump appears to be absent. Compared to the $p \leq 9''$ and Bulge KLFs this deficit is significant at the 4 to 5 σ level. Relative to the $p \leq 9''$ KLF, there may also be an excess of stars at $13\leq K_s \leq$15. Hence, the cusp probably lacks old low mass, HB/RC stars. The cusp probably also lacks late type giants. There are indications that there is an excess of early-type stars present in the cusp (Genzel et al., 2003).

We conclude that the content and/or the properties of the stars in the cusp are different from those in the outer regions. The dense cusp may lack old, low mass stars. This could be due to mass segregation effects, which tend to expel low mass stars from the cluster centre. Alternatively in the dense environment low mass stars ascending the red giant branch are stripped of their entire envelopes by physical collisions or close tidal encounters (Alexander, 1999, 2002; Genzel et al., 2003). Losing their envelopes well before their helium cores reach the critical mass for helium ignition, these stars would evolve directly to become helium white dwarfs, skipping the HB/RC phase. This could account for the absence of the HB/RC hump in the KLF and for the lower fraction of red giants in the cusp.

Chapter 7

Proper Motions in the Sgr A* Stellar Cluster

7.1   High Resolution Maps for the Epochs 1992-2003

The elaborate processing of the imaging data as described in chapter 4 provided us with maps
of 60 to 100 mas FWHM resolution for the epochs between 1992 and 2003 (no map for 1993,
two maps for each of the years 1996, 2000, and 2002). The maps are displayed in Figure 7.1.
They show the global evolution of the central cluster of stars near Sgr A* and how the stars
have changed their relative positions considerably during one decade of observations.

From the high-resolution maps, we extracted two sets of proper motion data: One is based
on the imaging data between 1992-2002 and includes the SHARP and Gemini data sets as well
as one NACO/VLT epoch (2002.66). The other set includes five epochs of NACO/VLT H and
K-band imaging data taken between May 2002 and July 2003.

7.2   Stellar Positions, Proper Motions and Photometry

7.2.1   Epochs 1992-2002

As can be seen in Figure 7.1, the source density in the central cluster is very high, so that
because of the high proper motions a star may "merge" at some epoch with another one and
"reappear" at some later epoch. With a baseline that is long enough, however, it is possible to
disentangle these stellar motions. Source identification (and re-identification at a later epoch)
is usually done "by eye". In order to cross-check and support our "by eye" identifications in
the comparably low resolution SHARP/NTT images, we implemented a largely automatised
procedure that, given initial source positions and identifications at one epoch, identified the
selected sources and measured their positions in the maps of all other epochs.

Assuming constant relative fluxes of the stars, the appearance of the stellar cluster at dif-
ferent epochs results just from rearrangements of the stars. If the differences in the positions
of the stars are not too large, which is e.g. the case for two maps from subsequent observing
epochs, this rearrangement can be done automatically with a least squares fit (that also takes
into account an offset in the overall flux and adapts the PSF FWHM to the respective images).
To start the position finding algorithm, we measured the positions and relative fluxes of stars
in the cluster in the NACO August 2002 image, the deepest and highest resolution image in
our data set. From these initial estimates, a model image (using Gaussian PSFs) was created
that was subsequently fit (in a least square sense) to the maps of the stellar cluster from ear-
lier epochs. Hence, the measured positions of the stars at one observing epoch were used as
initial estimates for the positions in the preceding epoch. Nine bright, isolated reference stars
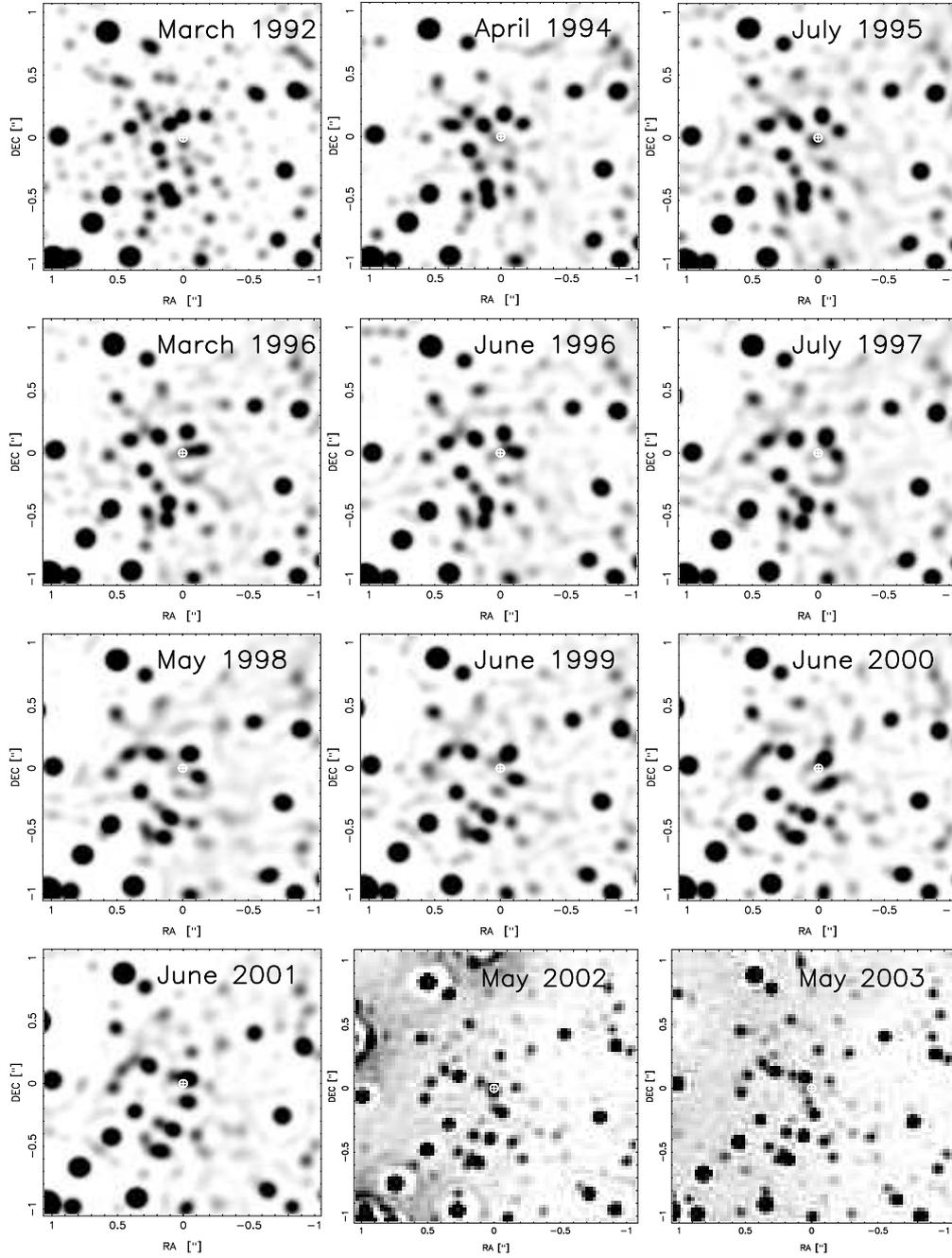
Figure 7.1: **High-resolution maps of the central** $1'' \times 1''$ **around Sgr A*.** *Epochs 1992 to 2001 show maps obtained with SHARP/NTT imaging data. They were created as described in chapter 4. FWHM of the SHARP maps is 100 mas. Epochs 2002 and 2003 are LR deconvolved and beam restored (FWHM of 60 mas) NACO/VLT images. The position of Sgr A* is marked with a white circle of 50 mas radius in all images.*

served for transforming the initial positions into the respective individual image frames with their unique rotation angles and different pixel scales.

We implemented the procedure described above in a series of IDL program codes and extracted the stellar positions in three steps. First, the brighter members of the cluster around Sgr A* were fitted and subtracted from the maps. The procedure was then repeated with fainter stars on the subtracted maps from step one. In a third iteration, final positions were obtained by taking the positions of the brighter and fainter stars measured in steps one and two and fitting them simultaneously to the original maps of all epochs. With this final iteration, we tried to minimise the influence that sources very close to each other have on their mutual positions. Errors on the measured positions were determined by comparing the positions from the fitting procedure with centroid positions measured on the stars with two different apertures sizes and taking the maximum deviation of the centroid positions from the fitted position as an error estimate.

With the positions (in pixels) measured by the procedure described above, the offsets of the stars from Sgr A* in right ascension and declination were determined by using the positions and proper motions of 9 bright, isolated stars in our field of view from the Ott (2003) list (for details on astrometry, please see also chapter 5). The error of this transformation was estimated by repeating it with all possible different sub-sets of eight out of these nine stars. Final errors on the positions were obtained after adding quadratically these transformation errors and the position errors from the centroiding procedure.

We determined stellar proper motion velocities by a linear least squares fit to the time dependent stellar positions. In a final step, we controlled the derived positions and proper motions by comparing model images created with the measured quantities to the observed images at each observing epoch. In a few cases, the automated procedure failed to disentangle the motions of stars that were of comparable magnitudes and at coincident positions at some epochs. In some other cases, very faint stars "merged" with bright stars at some epoch, but it could not be determined reliably when and where they "reappeared". We rejected these sources with ambiguous proper motions from our list.

Based on the entire data set, we thus determined proper motions for 35 stars within $1.2''$ of Sgr A*. The main limitation to our sample comes from the resolution of the SHARP/NTT data. We could measure the proper motion of an additional 11 stars based on the higher resolution Gemini 2000 and NACO August 2002 images. With only two position measurements, however, the velocities of these stars are subject to significantly larger errors.

As an additional cross-check of the measured stellar positions, we compared the time dependent positions of the stars S2 and S8 with the ones published by Ghez et al. (2000), who have used the 10m-class Keck telescope for a very similar proper motion study (see Figure 7.2). In order to take into account the repositioning of Sgr A* by Reid et al. (2003), we applied an offset of $0.040''$ West and $0.009''$ North to the Keck data that we calculated from the differences in the positions of S2 for the 1995 epoch. As can be seen in Figure 7.2, the two groups' results are in excellent agreement.

The final list of stars with their magnitudes, their positions relative to Sgr A* in August 2002, and their proper motion velocities is given in Table 7.2. All velocities were calculated assuming a distance of 8 kpc to the Galactic Centre (Reid, 1993). An additional systematic error of the order ~ 20 kms^{-1} should be taken into account because of possible systematic errors of $\sim 0.003''$ in the stellar positions (see Schödel et al., 2003). The photometry was calibrated by selecting suitable reference stars from the Ott (2003) list. Magnitudes were measured by aperture photometry on the Lucy-Richardson deconvolved CONICA/NAOS image from August 2002, with errors estimated by choosing different aperture sizes. The left panel in Figure 7.3 illustrates the measured stellar proper motions with velocity vectors superposed on a NACO 2002.4 map.

We identified 6 stars which were subject to significant acceleration (deviation from a linear trajectory $> 3\sigma$) and have marked them with an asterisk in Table 7.2. The proper motion velocities given for these stars for the 2002 epoch were derived from linear fits to subsets of
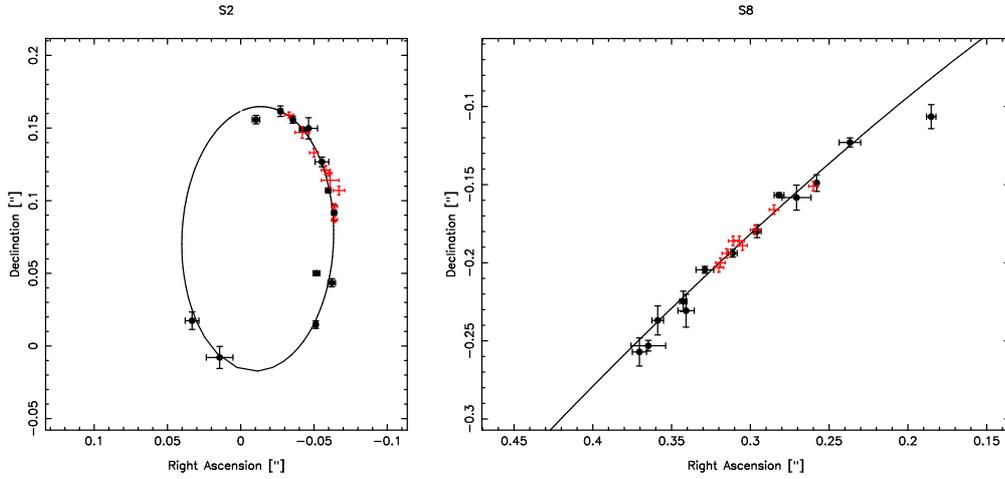
Figure 7.2: **Comparison between SHARP/NTT and Keck positions**. *A comparison between positions of the stars S2 and S8 as measured by our group and by the Ghez et al. (2000) group. SHARP/NTT positions are marked by filled black circles with error bars, Keck positions by red error bars. An offset of 40 mas W and 9 mas N (derived form the difference in position of S2 for the 1995 epoch) was applied to the Keck data in order to take into account the astrometric offset between the data sets. Straight lines mark the orbits fitted to the position of S2 and S8 (see chapter 8). For a colour version of this Figure see Appendix B.*
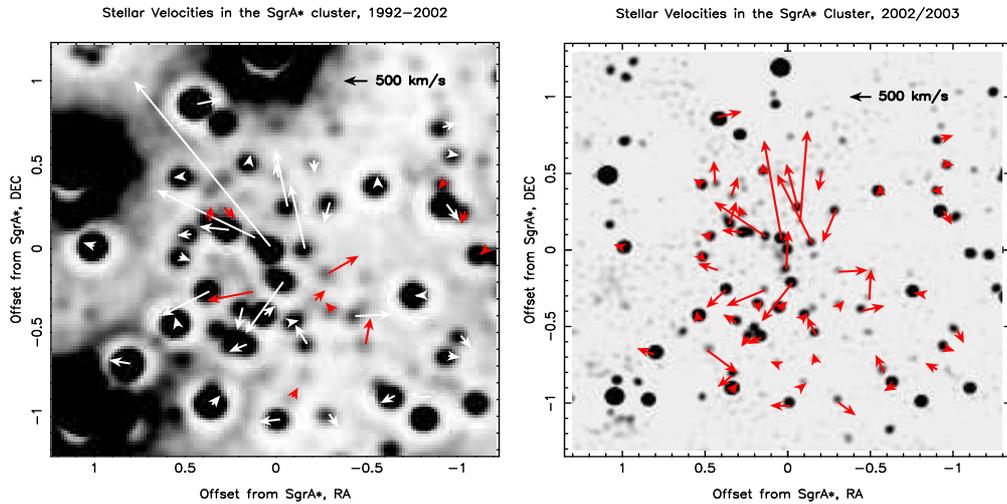
Figure 7.3: **Proper motion of stars near Sgr A*.** *Left panel: Stellar velocities within 1.2″ of Sgr A*, derived from the SHARP/Gemini/NACO data set, superposed on a NACO 2002.4 LR deconvolved and beam restored K-band image. Proper motions of the accelerated sources S1, S2, S8, S12, S13 and S14 are approximate estimates for this epoch. White arrows: Stars with proper motions based on the entire data set. Grey arrows: Stars with proper motions determined from the Gemini 2000 and the NACO August 2002 images only. Right panel: Stellar velocities within 1.2″ of Sgr A*, derived from the NACO 2002/2003 imaging data, superposed on a NACO 2003.35 LR deconvolved and beam restored K-band image.*

the measured positions, i.e. to time spans that were short enough to approximate the motions of the stars by linear trajectories.

As for the naming of some individual sources, S1 through S12 were named in earlier publications about the central cluster, e.g. Genzel et al. (1997). S12 was mentioned by Genzel et al. (1997) as a possible variable source and counterpart of Sgr A*. Ghez et al. (1998) detected this source as well, but excluded the possibility of it being a Sgr A* counterpart because of its large proper motion, which was inconsistent with the expected extremely low proper motion of Sgr A*. Also, the repositioning of Sgr A* by Reid et al. (2003) moved its location ∼ 50 mas East of the position used by Genzel et al. (2000). With our new analysis, based on a much longer time line, we arrive at the following interpretation: S12 (Genzel et al., 1997) was coincident (at the level of the SHARP resolution) with a fainter source, S3, in the 1995 epoch. It passed the peri-centre of its orbit at that time, moving at >1000 km/s . The proper motion of S12 was directed towards the north. In 1998 and 1999 it was located so close to the brighter source S2 that it could hardly be separated with the resolution of SHARP/NTT. S12 "reappeared" north of S2 in 2000. As for S3, we dropped it from our list because we could not determine an unambiguous proper motion for that source. We show maps for the epochs 1995.5, 1996.4, 1999.5, and 2000.5 in Figure 7.4. All stars labelled in these maps (with the possible exception of S3) were subject to significant accelerations as described below.

7.2.2 Epochs 2002 and 2003

The NACO imaging data with their high resolution and high Strehl ratio are of such excellent quality that we could determine reliable proper motions for 55 stars in the central $1.2'' \times 1.2''$ with a time line of just one year (five observing epochs). The NACO images are a factor of two to three deeper and have about twice the resolution of the SHARP data. Unfortunately, the short time base did not yet allow extracting reliable proper motions for the faintest stars in crowded areas. On the other hand, since we limited our analysis to the brighter (K≤ 17) stars and since source confusion with NACO is much lower than with SHARP images, the source identification could easily be done by eye.

Stellar positions and photometry were determined with the program package *StarFinder* [1]. It uses a PSF fitting technique and serves specifically for the purpose of high precision astrometry and photometry in adequately sampled high-resolution (usually AO) images of crowded fields.

With *StarFinder*, we extracted stellar positions and fluxes for each epoch from a linear and a LR deconvolved image. Final fluxes and positions as well as corresponding errors were obtained from averaging the measurements from linear and LR deconvolved images.

The offsets of the stars from Sgr A* in right ascension and declination were determined by using the positions and proper motions of 20 bright, isolated stars in our field of view from the Ott (2003) list. The transformation was repeated about 10 times with different subsets of 11 out of these 20 stars in order to obtain an error estimate. The transformation errors were added quadratically to the errors of the stellar positions extracted with *StarFinder*.

The final list of stars with their magnitudes, their positions relative to Sgr A* in June 2003, and their proper motion velocities is given in Table 7.3. All velocities were calculated assuming a distance of 8 kpc to the Galactic Centre (Reid, 1993). The photometry was calibrated with the magnitudes given by Blum, Sellgren, & DePoy (1996) for the stars, IRS 33SE, IRS 16C, IRS 16NW, and MPE+1.0 − 7.6 (see also Ott et al., 1999). The right panel in Figure 7.3 illustrates the measured stellar proper motions with velocity vectors superposed on a NACO 2003.35 map. The agreement of the measurements between the 1992-2002 and the 2002/2003 data sets is generally good, although discrepancies can be found for some of the fainter sources,

---

[1] StarFinder was developed by Diolaiti et al. (2000). The IDL code can be downloaded, for example, at the StarFinder page at the University of Bologna (http://www.bo.astro.it/∼giangi/StarFinder/).
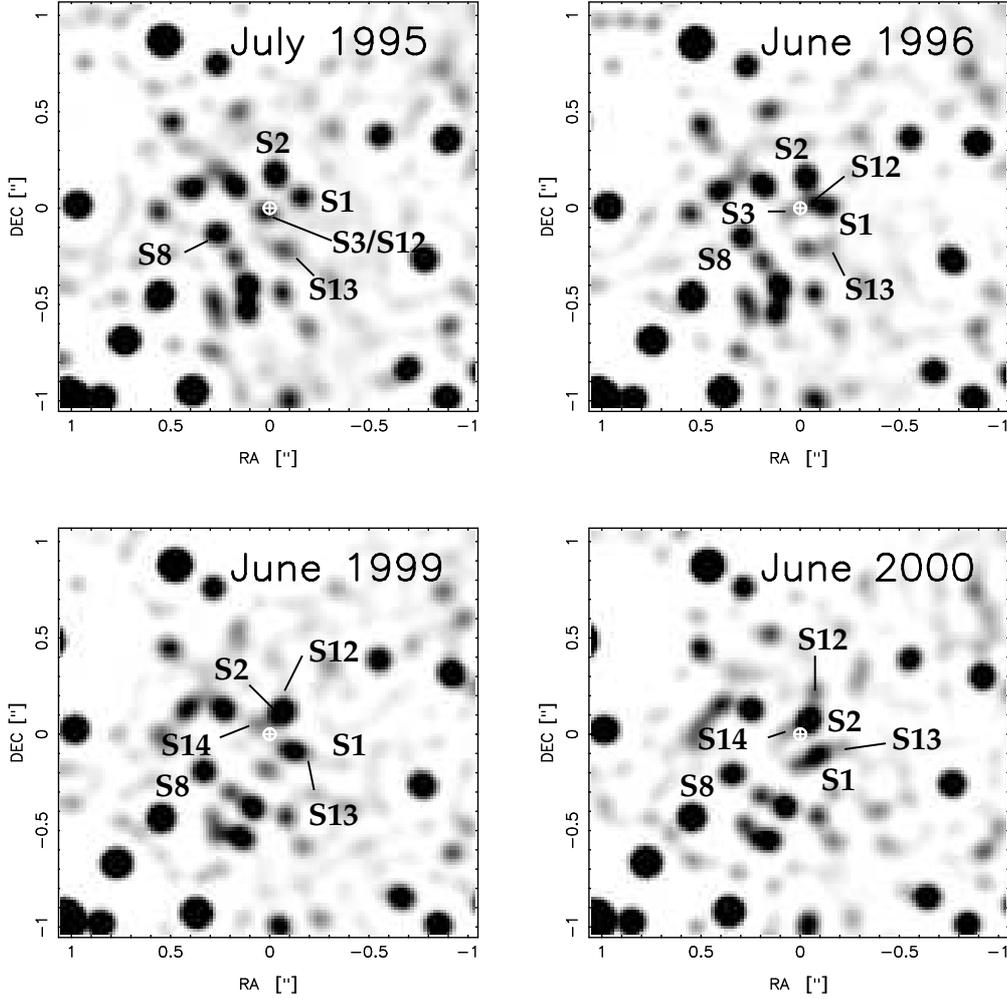
Figure 7.4: **Identification of fast moving stars.** *Identification of the sources S1, S2, S3, S8, S12, S13, and S14 for the epochs 1995.5, 1996.4, 1999.5, and 2000.5. The white circle of ~50 mas radius marks the position of Sgr A*.*

which are more easily identified on NACO/VLT images because of the lower confusion (by factors between four and nine).

7.3   Velocity dispersion and central dark mass

With the proper motions from Tables 7.2 and 7.3 we calculated the enclosed mass with the Leonard-Merritt (LM, Leonard & Merritt 1989) mass estimator. For this purpose we compiled various lists of stellar positions and velocities. We created a long list (LL) with all sources from Table 7.2 and a short list (SL) that excluded the larger error proper motions determined just from the Gemini/NACO images. Additionally, we measured the projected velocities of the accelerated stars at two different epochs in order to take into account the influence of their varying velocities. We thus obtained 4 lists (SL1, SL2, LL1, LL2). Since the 2002/2003 NACO/VLT data set was of homogeneous quality and since it covered such a short time interval, all proper motions could be approximated by linear fits. Table 7.1 lists the calculated values of the enclosed mass, of the radial velocity dispersion, and of the ratio between the projected radial and

List	N	$2/\pi/\langle 1/p \rangle$ ($''$)	M_{LM} $1 \times 10^6 M_\odot$	σ_R km s^{-1}	σ_T/σ_R	β
SL1	35	0.58	3.7 ± 0.9	840 ± 104	0.66 ± 0.12	0.66 ± 0.08
SL2	35	0.67	3.7 ± 0.9	540 ± 67	0.78 ± 0.12	0.49 ± 0.14
LL1	46	0.61	3.3 ± 0.7	745 ± 78	0.68 ± 0.10	0.64 ± 0.07
LL2	46	0.68	3.1 ± 0.7	498 ± 52	0.98 ± 0.14	0.06 ± 0.39
NACO	55	0.62	4.0 ± 0.8	634 ± 67	0.71 ± 0.11	0.60 ± 0.09

Table 7.1: **Table of enclosed mass estimates, velocity dispersions, and anisotropy parameters from proper motions of stars within** $1.2''$ **of Sgr A*.** *From the 1992-2002 data we compiled four lists of stellar proper motions: 2 short lists including 35 proper motions from the entire SHARP/Gemini/NACO data set and 2 long lists (LL) including additionally the (larger error) proper motions of 11 sources solely based on the Gemini July 2000/NACO September 2002 images. For the 6 stars with measured accelerated motion, we determined velocities at two different epochs each and included them in the short and long lists (SL1, SL2, LL1, LL2). The last line of the table refers to the NACO/VLT 2002-2003 data set. N is the number of stars in the respective list, p is the projected distance from Sgr A* (please consult to Bahcall & Tremaine 1981 for the meaning of the expression $2/\pi/\langle 1/p \rangle$), M_{LM} is the Leonard-Merritt mass estimator, σ_R is the projected radial and σ_T the projected tangential velocity dispersion. $\beta = 1 - \frac{\sigma_t^2}{\sigma_r^2}$ is the anisotropy parameter, where σ_t^2 and σ_r^2 are the 3-dimensional tangential and radial velocity dispersions.*

tangential velocity dispersions for all five lists.

Genzel et al. (2000) showed that the LM mass estimate M_{LM} differs from the intrinsic mass M_0 of the central object depending on the anisotropy parameter β and on the power-law slope of the central stellar cluster. This is because the LM mass estimate assumes that we have access to the full radial extent of the stellar cluster, which is not the case for our data set. From Figure 14 of Genzel et al. (2000) we estimate that $0.85 < M_{LM}/M_0 < 1.0$ for $0 < \beta < 0.5$ and a central density slope of $\alpha \approx 1.4$ (see chapter 6 and Genzel et al., 2003). This is an important difference to Genzel et al. (2000), who assumed a power-law slope near -2 for the central stellar cluster. This lead them to the conclusion that under the assumption of an isotropic cluster the LM mass estimator *overestimates* the central mass by $5 - 10\%$, while here we used a different value for the power-law slope and found that the LM mass estimator probably *underestimates* the central mass (in case of isotropy) by a value of around 10%. Taking into account the above range of the correction factor, we estimate a central mass of $3.5 \pm 0.4 \times 10^6 M_\odot$ from the weighted average of the LM mass estimates in Table 7.1.

Earlier statistical mass estimators from proper motion data resulted in systematically lower values for the enclosed dark mass. Using a variety of approaches (e.g. corrected LM mass estimators, Jeans equation modelling) Genzel et al. (2000) obtained masses between 2.6 and $3.3 \times 10^6 M_\odot$. Ghez et al. (1998) give a value of $2.6 \pm 0.2 \times 10^6 M_\odot$, using their Keck proper motion data set and a Bahcall-Tremaine mass estimator (Bahcall & Tremaine, 1981). Chakrabarty & Saha (2001) used a non-parametric approach for determining the central dark mass and derived a value of $2.0 \pm 0.7 \times 10^6 M_\odot$ from stellar proper motions. These values are systematically low when compared to mass measurements using Keplerian orbits of individual stars (see chapter 8). All statistical mass estimators must rely on the assumption that the central cluster of stars was adequately sampled. However, we saw in chapter 6 that there is a central cusp of stars, confined to distances of about $1 - 2''$ from Sgr A*. This means that there is a great number of high velocity stars near Sgr A*, which was not adequately sampled in earlier data sets. Because of the source confusion in the dense central cusp, it is only possible to determine proper motions for a significant amount of stars near Sgr A* if one uses a rather long time base (Sch¨odel et al., 2003) or deep, high-resolution imaging data, such as the NACO/VLT images. If the cusp stars with their high velocities are under-represented in proper motion data

sets, this will lead directly to an under-estimation of the enclosed central mass.

7.4   Anisotropy of the Nuclear Cluster?

With our proper motion data, we looked for possible anisotropy in the velocity structure of the Sgr A* stellar cluster, using $\gamma_{TR} = (v_T^2 - v_R^2)/v^2$ as anisotropy estimator, where v is the proper motion velocity of a star, with v_T and v_R its projected tangential and radial components. A value of $+1$ signifies projected tangential motion, -1 projected radial motion of a star. The properties of the anisotropy parameter γ_{TR} are discussed in detail in Genzel et al. (2000). They show that an intrinsic three-dimensional radial/tangential anisotropy will be reflected in the two-dimensional anisotropy estimator γ_{TR}.

- **1992-2002 data set:** The errors of the proper motions that are based solely on the Gemini 2000 and the NACO August 2002 data are too large for this analysis and were therefore not used. In the upper panel of Figure 7.5 we show a plot of γ_{TR} vs. the projected distance from Sgr A* (epoch 2002.7) for the remaining stars from Table 7.2. In Figure 7.6 we show histograms of γ_{TR} for stars within $0.6''$ (dotted lines), $1''$ (straight lines), and $1.2''$ (dashed lines) of Sgr A*. Since the stars changed their positions during the time span covered by the observations, we calculated the anisotropy parameter for the 2002.5 (middle panel in Fig. 7.6) and for the 1995.5 (upper panel in Fig. 7.6) epochs. In all cases, and at all distances, the number of stars on radial orbits is $2 - 3\sigma$ (assuming Poisson errors) above the number of stars on projected tangential orbits (see also Figure 8 in Genzel et al. 2000, who show histograms of γ_{TR} for clusters with varying intrinsic anisotropy).

- **NACO 2002/2003 data set:** We show a plot of γ_{TR} vs. the projected distance from Sgr A* (epoch 2003.45) in the lower panel of Figure 7.5. The corresponding histogram is displayed in the lower panel of Figure 7.6. This data set also exhibits an excess of radial orbits on the $2 - 3\sigma$ level. Stars on tangential orbits in the inner $0.3''$ appear to be under-represented, as can be seen in the lower panel of Figure 7.5.

From the projected radial velocity dispersions and the ratios of projected tangential to radial velocity dispersions listed in Table 7.1, we can estimate the anisotropy of the stellar cluster with the aid of equation (10) of Genzel et al. (2000):

$$\langle\beta\rangle = 1 - \langle\sigma_t^2\rangle/\langle\sigma_r^2\rangle = 3(\langle\sigma_R^2\rangle - \langle\sigma_T^2\rangle)/(3\langle\sigma_R^2\rangle - \langle\sigma_T^2\rangle) \tag{7.1}$$

Averaging the resulting values of β of the 5 lists in Table 7.1, we find $\langle\beta\rangle = 0.62 \pm 0.04$. Of course, this value has to be taken with a certain caution. While the value of the anisotropy agrees very well for four of the lists, we obtain a value of $\beta \sim 0$ in one out of the five cases. Genzel et al. (2000) also showed that a measurement of β from a small sample of stars can easily be skewed towards positive values. However, their simulations also showed that the probability of measuring $\beta \geq 0.5$ is as low as 25% for a sample of ≥ 30 stars out of intrinsically isotropic or tangentially anisotropic clusters (see their Figure 10).

Additionally, we checked whether any sky-projected overall rotation of the stars can be detected. Like Genzel et al. (2003) we used the normalised angular momentum $J_z/J_z(max) = (xv_y - yv_x)/pv_p$, where x and y are the offsets from Sgr A* in R.A. and Decl., v_x and v_y the corresponding velocity components, and p and v_p the projected distance from Sgr A* and the absolute value of the proper motion velocity. We show the plot of this parameter vs. the projected distance for the epoch 2002.7 in the upper panel and for the epoch 2003.35 in the lower panel of Figure 7.7. We find no significant projected overall rotation of the cluster. However, the lower panel of Figure 7.7 suggests that stars with large $J_z/J_z(max)$ are rare in the inner $0.3''$ of the Sgr A* cluster. This corresponds to our finding an excess of radial orbits in this region.
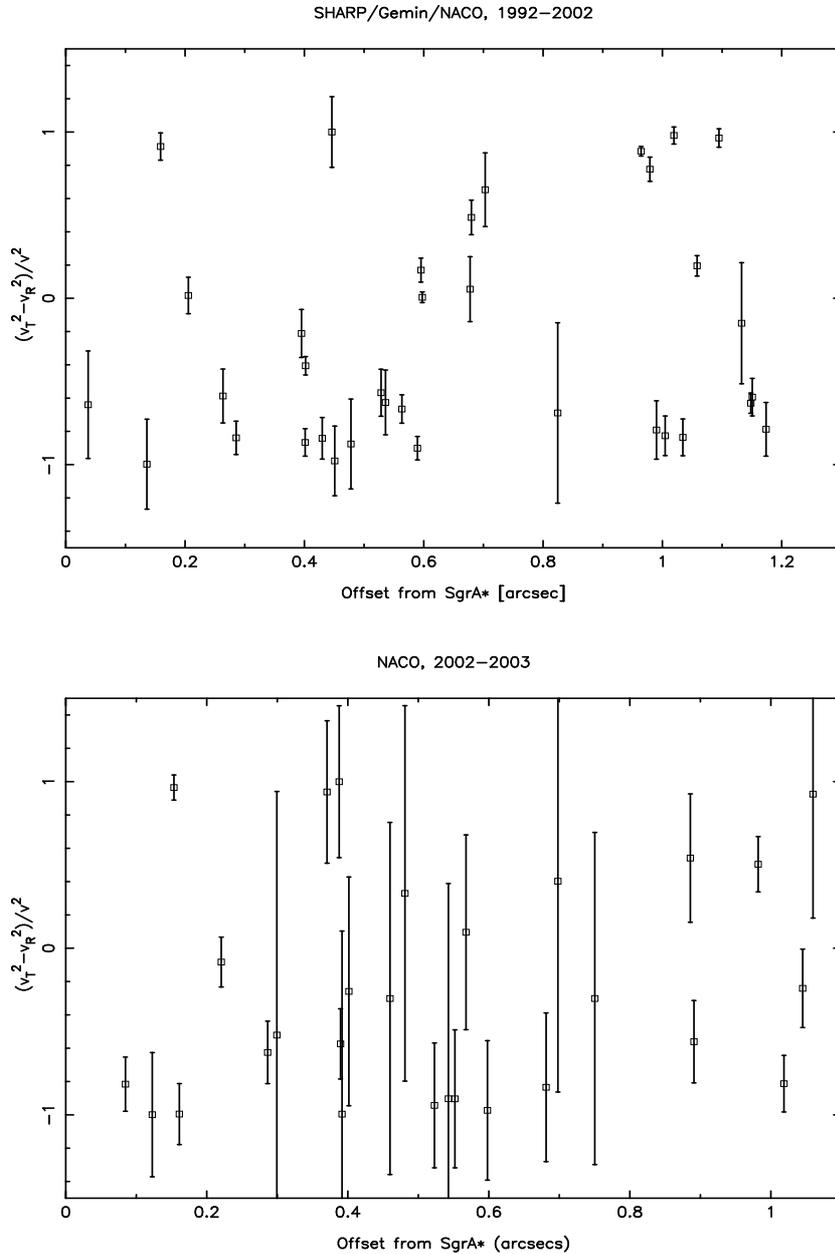
Figure 7.5: **Anisotropy parameters** γ_{TR} **of central cluster stars**. *The anisotropy parameter $\gamma_{TR} = (v_T^2 - v_R^2)/v^2$ vs. projected distance from Sgr A*. v is the proper motion velocity and v_T and v_R are its projected radial and tangential components. Upper panel: Stars from Table 7.2 with the proper motions determined on the base of the entire data set (histogram is for epoch 2002.7). Lower panel: NACO 2002/2003 data set (epoch 2003.45, Table 7.3). In both data sets, the majority of the stars appear to be on radial orbits.*
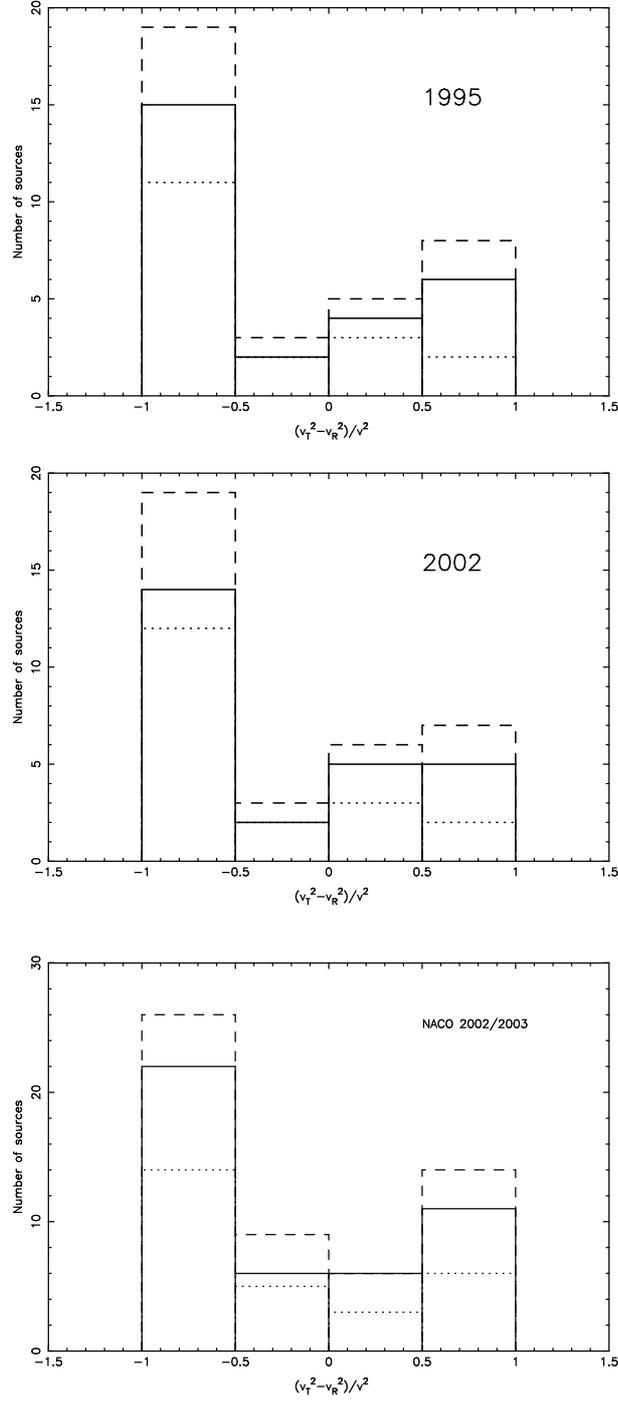
Figure 7.6: **Histograms of anisotropy parameter** γ_{TR}. *Histograms of the anisotropy parameter* $\gamma_{TR} = (v_T^2 - v_R^2)/v^2$. *v is the proper motion velocity and* v_T *and* v_R *are its projected radial and tangential components. Upper panel: 1995.5; middle panel: 2002.7. Dotted lines: Stars at projected distances* $< 0.6''$ *from Sgr A*; solid lines: stars at projected distances* $< 1''$; *dashed lines: stars at projected distances* $< 1.2''$. *Lower panel: Histogram based on the NACO 2002/2003 proper motion data (epoch 2003.45, Table 7.3).*
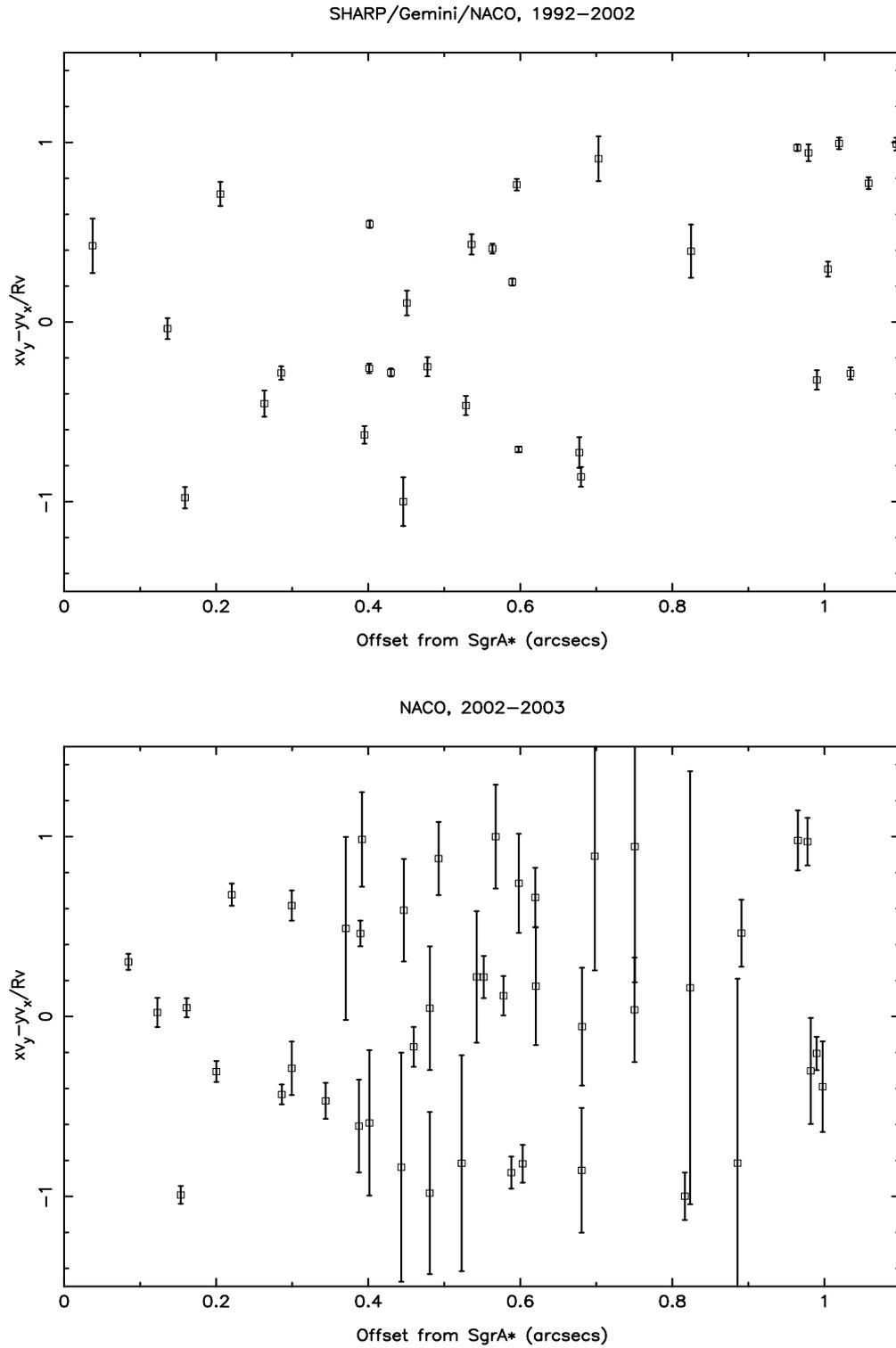
Figure 7.7: **Angular momenta of central cluster stars**. *The normalised angular momentum* $J_z/J_{z,\max} = (xv_y - yv_x)/pv_p$ *vs. projected distance from Sgr A*. Upper panel: SHARP/Gemini/NACO data for the 2002.7 epoch for the stars with proper motions based on the entire ten year data set. Lower panel: NACO 2002/2003 data for epoch* 2003.45.

With densities of the order 10^7 to 10^8 M$_\odot$pc^{-3} in the central arc-second (Genzel et al., 2003; chapter 6), two-body interactions should be comparably frequent and the relaxation time is less than 10^8 yr. In this case we would expect to observe an isotropic velocity field. Therefore, the observed radial anisotropy comes as a surprise. Possibly, only the brighter, potentially young stellar component is un-relaxed and is characterised by radial anisotropy. It is clear that we need a larger and deeper proper motion data base and/or a statistically significant sample of well determined orbits of individual stars before we can definitely exclude isotropy of the overall cluster. But should the radial anisotropy indeed be proven to be true, theoretical and modelling efforts will be needed to understand this property of the Sgr A* stellar cluster. The Sgr A* cluster appears to contain young, O/B-type stars the origin of which cannot be explained satisfactorily by current models. A potential anisotropy of the cluster might well provide clues that might help understanding its formation.

As a bottom line, we can say that the current data definitely exclude tangential anisotropy. Significant tangential anisotropy would be expected in systems with binary black holes (Gebhardt et al., 2003). Stars on highly eccentric orbits would be ejected or destroyed preferentially in such systems.

ID	Name	R (arcsec)	M_K (mag)	dM_K (mag)	ΔR.A (arcsec)	dΔR.A. (arcsec)	ΔDEC (arcsec)	dΔDEC (arcsec)	$V_{R.A.}$ (km s^{-1})	$dV_{R.A.}$ (km s^{-1})	V_{DEC} (km s^{-1})	dV_{DEC} (km s^{-1})
1	S2*, S0-2	0.037	13.9	0.1	0.033	0.005	0.017	0.006	2913	166	3834	42
2	S14*, S0-16	0.136	15.7	0.2	0.118	0.004	0.068	0.004	2106	190	1103	86
3	S13*, S0-20	0.159	15.8	0.3	-0.159	0.004	0.004	0.005	359	91	1483	48
4	S1*, S0-1	0.206	14.7	0.1	-0.039	0.006	-0.202	0.004	801	19	-1183	39
5	S12*, S0-19	0.263	15.5	0.2	-0.064	0.005	0.256	0.005	255	76	1098	52
6	S4, S0-3	0.286	14.4	0.1	0.262	0.004	0.113	0.008	623	17	74	14
7†		0.288	16.5	0.3	0.129	0.006	-0.257	0.007	984	187	-207	207
8†		0.328	16.9	0.3	-0.295	0.004	-0.144	0.002	-633	82	397	51
9†		0.371	16.4	0.3	0.281	0.007	0.242	0.003	-237	135	-246	93
10†		0.375	17.3	0.4	-0.219	0.003	-0.305	0.002	-213	74	225	98
11	S10, S0-6	0.395	14.2	0.1	0.059	0.009	-0.391	0.009	-210	9	193	15
12†		0.399	15.2	0.1	0.362	0.010	0.168	0.007	-12	180	330	185
13	S9, S0-5	0.401	15.1	0.1	0.184	0.004	-0.356	0.005	109	12	-499	11
14	, S0-8	0.402	15.8	0.3	-0.296	0.002	0.272	0.005	121	11	-471	6
15		0.43	17.0	0.4	-0.016	0.002	0.43	0.005	83	6	326	12
16		0.446	15.4	0.2	-0.1	0.007	-0.435	0.006	-105	10	23	12
17	S8*, S0-4	0.451	14.5	0.1	0.37	0.004	-0.257	0.009	536	40	-569	36
18	S6, S0-7	0.478	15.4	0.2	0.47	0.008	0.085	0.007	295	23	-21	14
19†		0.482	16.6	0.3	-0.313	0.01	-0.366	0.003	152	190	175	210
20	S7, S0-11	0.528	15.3	0.2	0.526	0.005	-0.048	0.006	-225	10	-93	12
21		0.536	15.6	0.2	0.148	0.003	0.515	0.003	-29	9	174	10
22		0.563	16.7	0.3	-0.21	0.004	0.523	0.004	-11	7	-290	7
23		0.589	15.7	0.2	-0.169	0.007	-0.565	0.007	244	7	431	9
24	S11, S0-9	0.595	14.4	0.1	0.164	0.009	-0.572	0.005	371	9	-167	12
25		0.598	16.2	0.2	-0.442	0.003	-0.402	0.004	-774	9	40	8
26		0.678	15.1	0.1	0.525	0.006	0.429	0.005	153	11	-20	10
27	W6, S0-12	0.68	14.4	0.1	-0.562	0.003	0.383	0.004	13	9	190	8
28	, S0-13	0.703	13.4	0.1	0.546	0.006	-0.443	0.009	34	13	132	12
29†		0.752	17.0	0.4	-0.496	0.004	-0.565	0.003	-99	64	590	110
30	W9, S0-14	0.825	13.8	0.1	-0.775	0.002	-0.28	0.004	34	6	-2	4
31†		0.887	17.0	0.3	-0.094	0.005	-0.882	0.005	-108	124	209	167
32	, S1-3	0.964	12.3	0.1	0.429	0.006	0.864	0.003	-518	6	115	9
33	W5, S0-15	0.979	13.7	0.1	-0.943	0.004	0.261	0.008	-262	11	-374	16
34	, S1-5	0.99	12.6	0.1	0.348	0.008	-0.927	0.005	-164	13	199	13
35†		1.003	15.6	0.1	-0.924	0.006	0.392	0.004	103	162	-140	144
36	, S1-1	1.005	13.2	0.1	1.005	0.005	0.017	0.004	223	8	73	9
37	, S1-2	1.019	14.9	0.1	-0.019	0.004	-1.019	0.004	453	10	-55	13
38		1.034	16.1	0.1	-0.296	0.003	-0.991	0.004	-193	11	-294	11
39	, S1-4	1.058	12.6	0.1	0.806	0.004	-0.685	0.005	441	8	80	15
40†		1.065	15.8	0.3	-1.042	0.004	0.219	0.003	82	135	-280	111
41	, S1-8	1.095	14.2	0.1	-0.652	0.003	-0.88	0.007	296	8	-162	9
42		1.133	15.7	0.1	-0.984	0.005	0.561	0.007	-102	13	-20	14
43†		1.135	14.8	0.1	-1.135	0.004	-0.029	0.005	37	83	-37	119
44	, S1-7	1.148	15.8	0.1	-1.023	0.003	-0.522	0.005	-212	5	-277	8
45		1.151	15.3	0.1	-0.956	0.003	-0.641	0.006	-236	6	-29	13
46	, S1-6	1.174	15.6	0.1	-0.923	0.007	0.725	0.008	-309	15	107	15

Table 7.2: **List of stars within** $1.2''$ **of Sgr A* as determined from the 1992-2002 SHARP/Gemini/VLT data set.** *The stars are ordered with increasing distance from Sgr A* (third column). Stars marked with an asterisk show accelerated movement. The velocities given for these stars are approximate velocities for the 2002.7 epoch, derived from a linear fit to a subset of the positional data. Positions and magnitudes are for the epoch 2002.66. An additional general ~0.1 magnitude systematic error should be taken into account because of uncertainties in the fluxes of the calibration sources. Proper motions of stars marked with a † are based solely on the Gemini/NACO data subset as described in the text. Names behind a comma in column 2 refer to names assigned by Ghez et al. (1998), except S0-16, S0-19, and S0-20, which refer to Ghez et al., astro-ph/0306130. We estimate an additional systematic error of the order $0.003''$ on the positions at all epochs (see Schödel et al., 2003). That corresponds to an additional error of ~20 km/s in the proper motion velocities.*

ID	Name	R (arcsec)	M_K (mag)	dM_K (mag)	ΔR.A (arcsec)	$d\Delta$R.A. (arcsec)	ΔDEC (arcsec)	$d\Delta$DEC (arcsec)	$V_{R.A.}$ (km s^{-1})	$dV_{R.A.}$ (km s^{-1})	V_{DEC} (km s^{-1})	dV_{DEC} (km s^{-1})
1	S2	0.085	13.9	0	0.038	0.002	0.075	0.002	410	87	2501	118
2	2	0.123	15.5	0.1	0.009	0.003	-0.122	0.002	-49	76	979	100
3	S13	0.153	15.6	0.1	-0.146	0.002	0.046	0.001	819	68	1751	64
4	S14	0.161	15.5	0.1	0.135	0.002	0.088	0.002	1210	73	881	79
5	47	0.2	17.1	0.2	-0.075	0.002	0.186	0.001	-170	132	2330	112
6	S1	0.221	14.4	0.1	-0.024	0.002	-0.219	0.002	709	60	-966	62
7	S12	0.286	15.2	0.1	-0.06	0.002	0.28	0.002	267	55	1106	65
8	53	0.299	16.3	0	0.141	0.002	-0.264	0.002	899	65	-396	87
9	S4	0.299	14.1	0.1	0.276	0.002	0.116	0.002	481	61	51	71
10	46	0.344	16.6	0.1	-0.313	0.001	-0.143	0.002	-672	49	40	66
11	12	0.371	16.1	0.1	0.28	0.002	0.242	0.002	64	65	177	96
12	S10	0.388	13.8	0	0.052	0.002	-0.384	0.002	-195	60	194	63
13	7	0.39	15.3	0	-0.291	0.002	0.259	0.002	310	52	-815	59
14	S5	0.392	15	0.1	0.352	0.002	0.172	0.002	-161	67	565	115
15	S9	0.402	14.8	0.1	0.181	0.002	-0.358	0.002	-32	68	-192	67
16	30	0.444	14.9	0.1	-0.103	0.002	-0.431	0.002	-81	57	85	58
17	50	0.447	99	99	0.428	0.003	-0.13	0.002	451	161	158	93
18	S8	0.46	14.1	0.1	0.377	0.002	-0.264	0.002	454	64	-450	73
19	31	0.481	16.2	0	-0.314	0.001	-0.364	0.001	-106	49	135	60
20	S6	0.481	15.1	0.1	0.473	0.002	0.089	0.002	218	68	52	77
21	48	0.493	16.4	0.1	0.34	0.002	0.357	0.002	-150	67	467	79
22	S7	0.523	14.9	0.1	0.521	0.002	-0.048	0.002	-104	65	-122	76
23	9	0.543	15.3	0.1	0.147	0.002	0.522	0.002	9	63	177	65
24	8	0.552	16.5	0.1	-0.206	0.002	0.512	0.001	81	58	-499	60
25	19	0.568	15.3	0	0.315	0.002	-0.472	0.002	297	74	206	73
26	29	0.578	15.3	0.1	-0.168	0.001	-0.553	0.001	194	52	444	57
27	33	0.588	17.1	0.1	-0.494	0.001	-0.32	0.001	-41	39	752	53
28	S11	0.598	14	0.1	0.165	0.002	-0.575	0.002	311	78	-153	69
29	32	0.603	15.4	0.1	-0.454	0.001	-0.397	0.001	-521	40	127	50
30	49	0.62	16.4	0	0.438	0.002	0.438	0.002	36	75	567	80
31	52	0.62	99	99	0.241	0.002	-0.572	0.002	154	96	-242	73
32	W6	0.681	14.1	0	-0.56	0.001	0.387	0.001	9	47	160	41
33	10	0.681	14.7	0.1	0.526	0.002	0.433	0.002	175	62	129	77
34	S0-13	0.698	13.1	0	0.544	0.002	-0.437	0.002	32	67	153	76
35	27	0.75	16.8	0.1	-0.17	0.001	-0.731	0.001	61	67	224	74
36	54	0.751	17.5	0.1	0.059	0.002	-0.748	0.002	182	110	80	93
37	51	0.816	16.1	0.1	0.484	0.002	-0.658	0.002	-700	86	-566	81
38	W9	0.823	13.4	0	-0.774	0.001	-0.281	0.001	30	36	6	36
39	26	0.886	16.8	0.1	-0.1	0.002	-0.88	0.001	-55	58	50	63
40	24	0.891	15.4	0	0.339	0.002	-0.824	0.002	334	71	-280	84
41	44	0.965	11.8	0	0.419	0.002	0.869	0.002	-559	68	138	69
42	W5	0.978	13.4	0	-0.945	0.002	0.252	0.001	-188	60	-345	32
43	S0-5	0.982	12.3	0	0.342	0.002	-0.921	0.002	-160	75	205	64
44	34	0.99	15.7	0.1	-0.583	0.001	-0.8	0.001	203	46	451	43
45	55	0.998	15.3	0.1	-0.919	0.002	0.388	0.001	207	65	0	41
46	45	1.004	12.9	0	1.004	0.002	0.019	0.002	191	61	66	87
47	25	1.019	14.5	0.1	-0.012	0.002	-1.018	0.001	465	62	8	54
48	28	1.045	15.8	0	-0.309	0.001	-0.998	0.001	-400	52	-324	47
49	S0-4	1.06	12.2	0	0.812	0.002	-0.681	0.002	392	69	155	81
50	35	1.095	13.8	0.1	-0.646	0.001	-0.884	0.001	261	36	-151	39
51	41	1.13	15.3	0.1	-0.983	0.002	0.557	0.001	-95	74	-13	31
52	37	1.157	15	0.1	-0.961	0.001	-0.644	0.001	-201	47	-65	35
53	38	1.157	15.5	0.1	-1.028	0.001	-0.531	0.001	-147	51	-304	36
54	42	1.175	15.2	0.1	-0.925	0.002	0.724	0.001	-304	74	98	37
55	36	1.191	17.2	0.1	-0.9	0.002	-0.779	0.001	270	73	163	55

Table 7.3: **NACO/VLT 2002-2003: List of stars near Sgr A*.** *The stars are ordered with increasing distance from Sgr A* (third column). Positions are for the epoch 2003.45. The photometry of the sources was done for the epoch 2003.353, where bright stars were not saturated and the photometry could be calibrated using reference stars from Blum, Sellgren, & DePoy (1996).*

Chapter 8

Stellar Orbits at the Centre of the Milky Way

After several years of monitoring the proper motion of the stars in the Sgr A* cluster, Ghez et al. (2000) and Eckart et al. (2002) determined the acceleration of three stars, all of them located at projected distances $< 0.5''$ (< 19 mpc) from Sgr A*. They reported preliminary estimates of their orbits, with predicted periods between 15 and several hundreds of years. The next steps were done by Schödel et al. (2002) and Ghez et al. (2003), who determined unique Keplerian fits for the orbit of the star S2 (called S0-2 by Ghez et al.), which had passed through the peri-centre of its orbit in spring 2002. The re-analysis of the SHARP imaging data, within the framework of this thesis, enabled us to determine/constrain the orbits of a total of six stars in the Sgr A* cluster. On the one hand, the orbits of stars close to Sgr A* provide essential information on the nature of this central radio source, such as its mass, exact position and distance. On the other hand, the properties of the orbits of individual stars give valuable insight into the dynamics of the central cluster, which might eventually – when the orbital elements are known for a statistically relevant sample of stars – lead to clues concerning the formation of the Sgr A* cluster.

8.1 Keplerian Orbits

8.1.1 Kepler's Laws of Motion

The trajectories of objects with a non-zero angular momentum in the gravitational field of a point mass or of a spherical body can be described by the laws of planetary motion found by Johannes Kepler (1571-1630). Kepler's famous three laws of planetary motion are:

1. The orbits have the shape of ellipses with the sun in one of the foci.

2. Law of equal areas: The area covered by the motion of the radius vector during a given time interval is independent of the position in the orbit.

3. The cube of the semi-major axis, a, is proportional to the square of the orbital period, T. In case $m \ll M$, where M is the mass of the central body such as the sun and m the mass of the orbiting test particle, e.g. a planet, the mass of the central body is given by the relation

$$M = \frac{4\pi^2 a^3}{GT^2},$$

(8.1)

where G is the gravitational constant.

Kepler's equation establishes the relation between time and the position on the orbit:

$$E(t) - e\sin(E(t)) = M(t) \tag{8.2}$$

Here, e is the eccentricity and $M(t) = 2\pi\frac{t-t_0}{T}$ is the so-called *mean anomaly* (where T is the period of the orbit). The *eccentric anomaly* $E(t)$ then can be used to calculate the time-dependent position on the orbit, via the relations

$$x = r\cos(\nu) \quad = \quad a(\cos(E) - e) \tag{8.3}$$
$$\text{and} \tag{8.4}$$
$$y = r\sin(\nu) \quad = \quad a\sqrt{(1-e^2)}\sin(E), \tag{8.5}$$

where a is the semi-major axis, and r, ν, x, and y are the coordinates in a polar and Cartesian system, respectively, with the sun (or another dominating mass) at the origin of the system. An ample treatment of Keplerian orbits, including instructive figures, can be found e.g. in Montenbruck & Pfleger (2002). Kepler's equation can only be solved numerically. We chose Newton's method for this purpose (Press et al., 1993; Montenbruck & Pfleger, 2002).

8.1.2   Orbital Elements

In the present work, we will analyse observed proper motions of stars in the immediate vicinity of Sgr A* in terms of Keplerian orbits. How well is this justified? It is a well established observation that the gravitational potential in the central 0.5 pc is dominated by that of a point mass (Eckart & Genzel, 1997; Genzel et al., 2000; Ghez et al., 2000; Eckart et al., 2002; Sch¨odel et al., 2002). If we assume that the mass to light ratio within 0.55" of SgrA*, is comparable to that of the outer cluster ($M/L(2\mu m) = 2 \times M_\odot/L_\odot$), the stellar mass in this radius due to the stellar cusp will be ~ 5000 M$_\odot$ and the combined relativistic and Newtonian peri-astron shift of S2 will be of the order ≤ 10 minutes of arc per year (Rubilar & Eckart, 2001; N. Mouawad, 2003, priv. comm.). An analysis of the proper motion data of the star S2 in terms of non-Keplerian orbits shows that at most 10 to 15% of the enclosed dark mass can be extended (N. Mouawad, 2003, priv. comm.). To first order, it is therefore reasonable to analyse the motions of the stars in the Sgr A* cluster in terms of Keplerian orbits.

The trajectory of a test mass m bound in the gravitational field of a body of mass M, with $m \ll M$ can be described by *seven orbital elements*:

- The **period** P of the orbit.

- The length of the **semi-major axis** a.

- The **eccentricity** or ellipticity $0 < e < 1$ of the orbit.

- The time of **peri-centre passage**, T_{peri}.

- The **angle of the line of nodes**, $0° \leq \Omega \leq 180°$. The line of nodes connects the two points of the orbit where it crosses the plane of the sky. The object moves toward the observer when it passes through the *ascending node*. The other node is called the *descending node*. Ω is usually defined east of north and corresponds to a rotation of the projected orbit on the plane of the sky. Changing Ω does not affect the shape of the projected orbit.

- The **angle from** (ascending) **node to peri-centre**, $0° \leq \omega \leq 360°$. ω corresponds to a rotation of the orbit within the orbital plane.

- The **inclination** $-90° \leq i \leq 90°$ is the angle between the plane of the orbit and the plane of the sky. It is measured *positive* when the northern part of the orbit lies *behind* the plane of the sky.
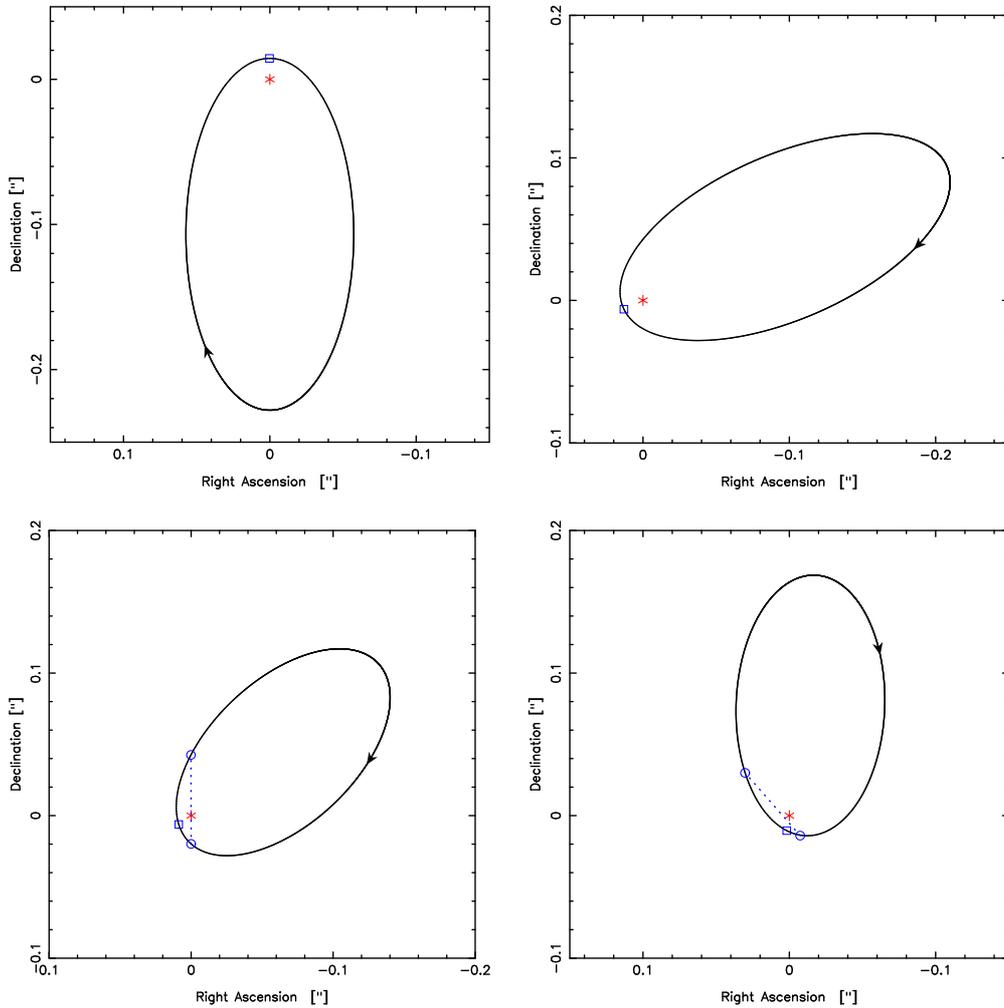
Figure 8.1: **The three angles of orientation of a Keplerian orbit and their subsequent application.** *Left upper panel: Trajectory in the plane of the orbit. Right upper panel: Trajectory in the plane of the orbit, rotated by $\omega = 245.4°$ in the direction of motion. Left lower panel: The same orbit, but with an inclination of $i = -48.1°$, as it is seen projected onto the plane of the sky. Right lower panel: The orbit rotated into its observed position in the plane on the sky. $\Omega = 45.0$ is the angle of the line of nodes (straight, dotted line), measured east of north. In all plots, the focus of the orbit is marked by an asterisk, the peri-centre by a square, and the ascending and descending nodes, connected by the line of nodes (dotted), are marked by open circles. The direction of motion is indicated by an arrow.*

Figure 8.1 illustrates the meaning of the three angles i, ω, and Ω. Starting out from the orbit of S2 as viewed when looking down onto the orbital plane, the Figure shows how the apparent shape and orientation of the orbit, as seen projected onto the plane of the orbit/sky, change through the successive application of ω, i, and Ω.

8.1.3   Fitting Keplerian Orbits

In principle, four positions, measured at sufficiently separated epochs, are sufficient for determining the orbital elements of a star if one assumes the validity of the Keplerian approach. A greater number of measurements is needed in practice, however, in order to perform a least-squares fit and to determine the orbital elements with a meaningful accuracy. Practice also shows that a good Keplerian fit to measured positions can only be achieved if more than half of the orbit has been observed. If this is not the case, it is possible to constrain the orbits by holding one or several parameters fixed during the fitting procedure or by using more elaborate, techniques, such as a simultaneous fit of multiple orbits (see Ghez et al., 2003, astro-ph/0306130).

When analysing stellar orbits around Sgr A*, we are not only interested in the orbital elements of the individual stars, but also in the overall properties of the system. Well determined orbits, as in the case of S2, allow constraining the location of Sgr A* more precisely than the radio measurements (Ghez et al., 2003; Schödel et al., 2003; Eisenhauer et al., 2003). Additional spectroscopic information on line-of-sight velocities allow for a geometric determination of the distance of Sgr A* from the solar system (Eisenhauer et al., 2003). Sufficient information on stellar orbits even allows determining upper limits on the motion of Sgr A* relative to the stellar cluster (see Ghez et al., 2003, astro-ph/0306130).

In the current analysis, we assume that the proper motion of Sgr A* relative to the surrounding stars can be neglected, i.e. that our frame of reference is well tied to Sgr A* (see discussion in the last section of chapter 5 and Eisenhauer et al., 2003). We also assume that the stars act as ideal test particles, i.e. that the masses of the individual stars are negligible compared to the mass of Sgr A*. Since the K$= 14 - 15$ stars in the Sgr A* cluster are most probably O/B-type stars (Genzel et al., 1997; Eckart, Ott, & Genzel, 1999; Figer et al., 2000; Gezari et al., 2002; Ghez et al., 2003), with 10 to 20 solar masses, that are orbiting a dark mass of several million solar masses, this assumption seems well justified.

We calculated the orbital parameters by fitting Keplerian orbits to the observed time-dependent positions in the plane of the sky. The "best" fit was determined in the least-squares sense. For this purpose, we built IDL program codes around the IDL MPFIT/MPCURVEFIT procedures. These procedures use the Levenberg-Marquardt technique to solve the least-squares problem for a given set of data points and for a given function. [1].

An important issue in numerical fits are the values of the starting parameters for the initial function. In case of the stellar orbits, we initially tried to vary all seven orbital elements on adequately spaced grids, thereby using each point in the seven-dimensional grid as a set of starting values for the fitting routine. In case of more than one formal solution, the set of parameters that provides the smallest reduced χ^2 was assumed to be the best set of orbital elements. However, this procedure is intensive in computing time because even for large grid spacings this requires several thousand runs of the fitting routine. After extensive tests we found that it was sufficient to just vary the initial values of the three angles of orientation. With given initial values for these angles, the correct values of eccentricity, semi-major axis, period, and time of peri-centre passage can be easily found by the fitting routine. It is helpful to use the available information on the approximate amount of the central dark mass in order to adjust the relation between the initial values for the period and the semi-major axis with the aid of Kepler's third law.

---

[1]The MPFIT program library has been written by Craig Markwardt and is publicly available at *http://cow.physics.wisc.edu/~craigm/idl/idl.html*

We varied Ω between $30°$ and $150°$, with step sizes of $60°$ and ω between $45°$ and $315°$, with step sizes of $90°$. As for the inclination angle, i, varying it with a step size of $1°$ proved to be a safe value. But in the case of well determined orbits, even just one single initial estimate of i was sufficient. Since the dynamical position of Sgr A* that could be determined from the orbit of S2 constrains the position of the dark mass by a factor of about ten better than the nominal radio position of Sgr A*, we used the focus of the orbit of S2 to fix the position of the foci of the other orbits.

While fairly large portions of their orbits were observed between 1992 and 2003 in the case of the stars S2, S12, and S14, this was not the case for the stars S1, S8, and S13. Only about 1/10th to 1/5th of their orbits were observed in the time span covered by observations. Therefore, when fitting the orbits of S1, S8, and S13, the fitting routine would not converge if we let all seven orbital elements vary freely. Instead, we varied the initial value of i between $1°$ and $89°$ in steps of $1°$ and held this parameter fixed while performing the least-squares fit. From the range of possible solutions, we picked the solution with the smallest χ^2.

8.2 The Orbit of the Star S2

The star S2 passed through the peri-centre of its orbit in spring 2002, approaching Sgr A* to a distance of less than one light day, while moving with a velocity of > 7000 km/s. The peri-centre passage of S2 was covered well by commissioning observations of the GC with NACO at the VLT. This enabled Sch¨odel et al. (2002) to determine the orbit of S2 and to infer a dark mass of $3.7 \pm 1.5 \times 10^6$ $M_\odot$ that must be enclosed within a volume of less than one light day radius. They concluded that Sgr A* must be a supermassive black hole because in the light of their results all alternative explanations were extremely unlikely.

Sch¨odel et al. (2003) and Ghez et al. (2003) refined the analysis of Sch¨odel et al. (2002) and showed that the focus of the orbit of S2 is located within a few milli-arcseconds of the nominal radio position of Sgr A*. This adds considerable weight to the assumption that the non-thermal radio source Sgr A* is a manifestation of the supermassive black hole. In this work we present the orbit of S2 as it was determined from the measured positions of S2 as described in chapter 4. These are the same measurements as used by Sch¨odel et al. (2003) and Eisenhauer et al. (2003). Eisenhauer et al. (2003) included 5 spectroscopic measurements of the line-of-sight velocity of S2 in their analysis (see their paper for details). Their result was determined within the framework of this thesis and represents our most recent analysis of the orbit of S2.

We show the best-fit orbit and the measured time-dependent positions of S2 in Figure 8.2 and the corresponding plot of measured and calculated line-of-sight velocities vs. time in Figure 8.3. We list the values of the orbital parameters in Table 8.1 along with the corresponding values given by Ghez et al. (2003) and Sch¨odel et al. (2002). The reduced χ^2 of our fit to the orbit is smaller than one. This indicates that the errors of the measurements were overestimated. Therefore, we rescaled the errors such that an overall reduced χ^2 of one resulted from the fit. The un-scaled errors are given in parentheses. All parameters derived for the orbit of S2 by the different authors agree very well within their errors.

There are currently five epochs of measurements of the line-of-sight velocity of S2 available (see Eisenhauer et al., 2003). Including these measurements allows to solve for the distance of Sgr A* from the solar system when fitting the orbit of S2. The distance to Sgr A* (and therefore to the GC) resulting from the orbit of S2 is 7.94 ± 0.38 kpc. This is the first direct geometrical determination of the distance to the GC. It agrees very well with the value of 8.0 ± 0.5 kpc determined by Reid (1993) by a combining various indirect methods. Through its influence on the calibration of standard candles, such as RR Lyrae, Cepheids and giants, the GC distance is a fundamental parameter for determining the structure of the Milky Way and for establishing the extragalactic distance scale. With the aid of instrumentation such as the integral-field spectrometer SPIFFI/SINFONI at the ESO VLT, available in the near future, it
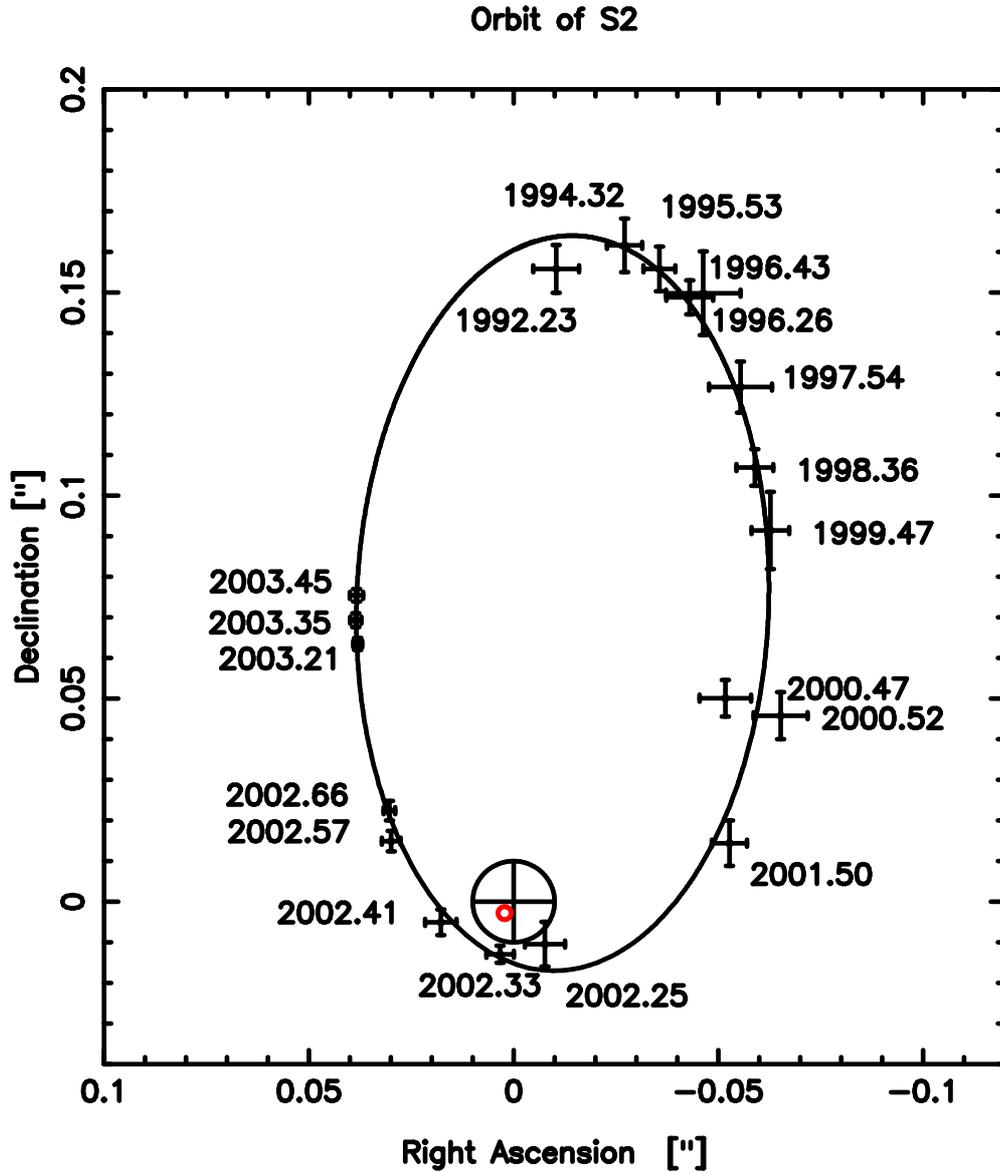
Figure 8.2: **Orbit of the star S2 around Sgr A*.** *Best-fit orbit and measured time-dependent positions of the star S2 as determined in this work. The positions are marked by the crosses of their errors bars. All positions are given relative to the radio position of Sgr A*, which is marked by a cross and a 10 mas error circle. The small red circle inside the radio error circle is the 1σ error circle of the focus of the orbit as determined by the Keplerian fit.*

will become possible to measure the line-of-sight velocities of several additional stars orbiting Sgr A*. This will allow to determine the GC distance with an uncertainty of the order 1% (see also the discussion in Salim & Gould, 1999).

Our best-determined value of the enclosed mass is $3.6 \pm 0.6(0.3) \times 10^6$ M$_\odot$. Here, the uncertainty takes into account the error of the distance measurement (the error for a fixed distance of 7.94 kpc is given in brackets). The derived enclosed mass agrees very well with the value $3.5 \pm 0.4 \times 10^6$ M$_\odot$ estimated from velocity dispersions with the LM mass estimator in chapter 7.
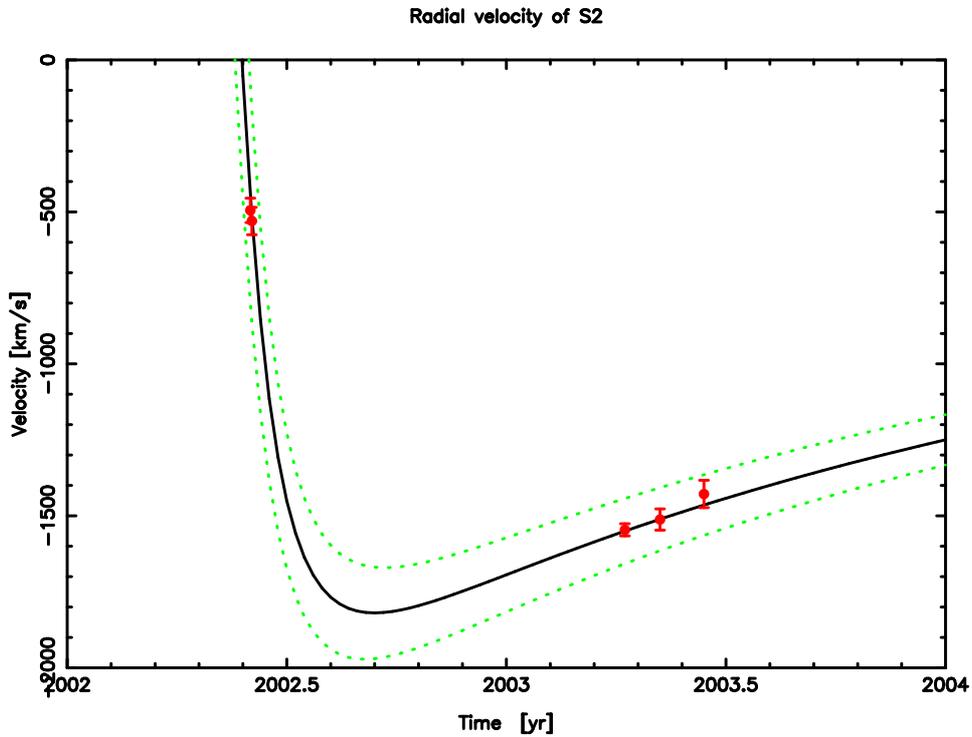
Figure 8.3: **Line of sight velocity of S2 along its orbit.** *Black line: Time-dependent line-of-sight velocity of S2, calculated from the best-fit orbit. Dotted green lines: Uncertainty of calculated line-of-sight velocity. Measured line of sight velocities are indicated by red filled circles and their error bars. Measurements in 2002 taken from Ghez et al. (2003), from 2003 from Eisenhauer et al. (2003). For a description of the various measurements of the line-of-sight velocity, see Eisenhauer et al. (2003). For a colour version of this Figure see Appendix B.*

We compare the orbit and measured positions of S2 from this work with the results of Ghez et al. (astro-ph/0306130) in Figure B.2 in Appendix B. The orbits were aligned by taking the difference between the S2 positions for 2002.3 as they result from the orbital parameters of this work and from Ghez et al. (astro-ph/0306130). We chose the 2002.3 epoch, because the uncertainties of the calculated positions of S2 are lowest around 2002.3, where the orbit is constrained very well and has the highest curvature. The measured positions from the Keck group (green crosses) were taken from Ghez et al. (2003). We did not include the 2003 position from Ghez et al. (astro-ph/0306130) because it could not be extracted with sufficient accuracy. from the corresponding plot. The orbits and positions agree well within their uncertainties. Most remarkably, the positions of the two foci differ by less than 1 mas, with a combined uncertainty of < 3 mas. The uncertainties were added quadratically (this is why the focus of astro-ph/0306130, given with an error of 1.5 mas there, appears to have a larger uncertainty). The NTT/SHARP positions between 1998 and 2001 appear to be located a few milli-arc-seconds further east than the Keck positions. A possible cause might be the lower resolution of NTT and the confusion of S2 with S14 or other sources at this epoch. Measurements in 2004/2005 should be able to settle the discrepancy.

Hence, the position of the dynamical centre of the orbit is offset by just a few milli-arc-seconds from the nominal radio position of Sgr A*. This adds strong weight to the assumption

that Sgr A* is coincident with the dark mass. Note that from the orbital solution the position of Sgr A* can be constrained by almost an order of magnitude better than from the radio positioning.

8.3   Other Stellar Orbits Around Sgr A*

Besides S2, we were able to determine or constrain the orbital elements for five additional stars near Sgr A*. The orbit of S2, which is by far the best known one, provides the valuable information of the dynamical position of the dark mass. This helps considerably in constraining the orbits of other stars because the uncertainty of the dynamical position of Sgr A* is about one magnitude smaller than the uncertainty of its radio position. Hence, we adopted the position and uncertainty of the dynamical centre of the orbit of S2 (as given by the offsets from the nominal radio position, listed in columns one and two of the first line for S2 in Table 8.1) as focus for the determination of all other stellar orbits. From here on, if not stated otherwise, we will assume a GC distance of 7.94 kpc, as determined from the orbit of S2.

- **S14:** S14 is a comparably faint star (K $\approx$ 15.7) that was confused with or close to brighter stars, such as S4 or S2, at many epochs. Therefore its positions in the SHARP/NTT images were difficult to determine. After preliminary fits of the orbit, we discarded positions that were more than 3σ off the best-fit orbit and iterated the fitting procedure. This left us with just two SHARP positions, for the epochs 1999 and 2001. The fit is clearly dominated by the much higher precision NACO/VLT images from 2002 and 2003. The orbital elements and their formal fit errors are listed in Table 8.1. In order to estimate the influence of the uncertainty of the position of the focus, we repeatedly fitted the orbit with 400 random offsets of the focus within its 1.2 mas error circle. The average and standard deviations of these 400 fits are listed in the second line for S14 in Table 8.1. The errors due to the uncertainty of the focus position are clearly much smaller than the formal fit errors in column one.

- **S12:** The star S12 passed through peri-centre already in 1995.5. However, it was close to the brighter stars S1 and S2 during large parts of its orbit. Therefore, it was difficult to disentangle its trajectory from the confused sources of the Sgr A* cluster. This became only possible with a sufficiently large portion of its orbit observed (Scḧodel et al., 2003). The result of the orbital fit tells us that it must have been almost coincident with S4 in the 1992 epoch. Photometric measurements support this assumption because S4 is 0.5 mag brighter in the 1992 image, consistent with the sum of the fluxes of S4 and S12. However, we did not use the 1992 position for the orbital fit. The orbital elements and their formal fit errors are listed in Table 8.1. In order to estimate the influence of the uncertainty of the focus, we repeatedly fitted the orbit with 400 random offsets of the focus within its 1.2 mas error circle. The average and standard deviations of these 400 fits are listed in the second line for S12 in Table 8.1. As in the case of S14, we see that the errors due to the uncertainty of the focus position are significantly smaller than the formal fit errors.

- **S1:** In the time between 1992 and 2003, we could observe only about 10% of the orbit of S1. However, it passed through peri-centre at about the middle of this interval, which allows a reasonable fit to the orbit. However, the fitting routine would not converge when we let the inclination vary freely. Therefore, we had to hold the inclination fixed and changed it in steps of $1°$ and obtained a whole range of solutions, with the reduced χ^2 varying by $\leq 6\%$. In Table 8.1, we list the orbital elements of the solution that gives an enclosed mass of 3.6×10^6 M$_\odot$, as determined from the orbit of S2. In the second line for S1 in Table 8.1, we list the orbital elements for the three solutions that result in enclosed masses closest to 3.3, 3.6, and 3.9×10^6 M$_\odot$, corresponding to the 1σ

errors of the enclosed mass as determined by the orbit of S2. Various tests showed that the errors due to the uncertainty in the focus position can be neglected compared to the formal fit errors and to the errors that result from the uncertainty of the enclosed mass.

- **S13:** Here, as in the case of S1, we held the inclination fixed and changed it in steps of $1°$. We obtained a whole range of solutions, with the reduced χ^2 varying by $\leq 5\%$. In Table 8.1, we list the orbital elements of the solution that gives an enclosed mass of $3.6 \times 10^6 \, \mathrm{M}_\odot$. In the second line for S13 in Table 8.1, we list the orbital elements for the three solutions that result in enclosed masses closest to 3.3, 3.6, and $3.9 \times 10^6 \, \mathrm{M}_\odot$, corresponding to the 1σ errors of the enclosed mass as determined by the orbit of S2. The errors due to the uncertainty in the focus position can be neglected compared to the formal fit errors and to the errors that result from the uncertainty of the enclosed mass.

- **S8:** The orbit of S8 was the most difficult orbit to fit because only about a tenth of its orbit was observed and neither the peri- nor the apo-centre passage fell into the period of observations. Here, as in the case of S1, we held the inclination fixed and changed it in steps of $1°$. We obtained a whole range of solutions, with the reduced χ^2 varying by $\leq 5\%$. In Table 8.1, we list the orbital elements of the solution that gives an enclosed mass of $3.4 \times 10^6 \, \mathrm{M}_\odot$. We could not obtain an orbit with a higher enclosed mass. The fitting routine could not provide any well defined formal errors for any of the fits. All formal errors were at least one magnitude larger than the corresponding parameters. In the second line for S8 in Table 8.1 we list the orbital elements for the three solutions that result in enclosed masses of 3.4, 2.9, (higher inclination than the first orbit) and $3.1 \times 10^6 \, \mathrm{M}_\odot$ (smaller inclination than the first orbit). The errors due to the uncertainty in the focus position can be neglected compared to the formal fit errors and to the errors that result from the uncertainty of the enclosed mass.

8.4   Properties of the Orbits

Keplerian orbits could be fitted well to all six stars with significant acceleration in our data sets. This confirmed again the validity of the assumption of a point mass that dominates the potential in the central 0.5 pc of the Milky Way. All six stars appear to be tightly bound to the central mass, with semi-major axes < 20 mpc (with the possible exception of S13). Alexander (1999) derived the following relation from the Jeans equation for the case of a stellar cusp with isotropic density and isotropic velocity dispersion, that is gravitationally dominated by a central point mass:

$$\frac{v_c^2}{\sigma^2} = 1 + \alpha \tag{8.6}$$

Here, v_c is the circular speed and σ the velocity dispersion at a given distance from the central point mass, while α is the slope of the central cusp. This implies that for $\alpha > 0$ at a given location in the cluster $\sigma < v_c$. Hence, the steeper the cusp, the higher will be the fraction of stars at a given location that are tightly bound to the central point mass. In chapter 6, we found for the central stellar cusp around Sgr A* a slope of $\alpha \sim 1.4$. Assuming a Maxwell-Boltzmann velocity distribution, with the escape velocity defined by $v_e = \sqrt{(2)} v_c$, this means that 99% of the stars in the cusp must be bound to the central black hole. This agrees well with our finding that all stars with measured accelerations are tightly bound to the central point mass.

In a spherical system of test particles orbiting a point mass we expect that the number of particles with eccentricities in the range $(e, e + de)$ is proportional to ede (Binney and Tremaine, p. 282, problem 4-22). We show the corresponding cumulative distribution function in Figure 8.6 (dotted line). It is skewed towards high eccentricities: 75% of the stars have $e > 0.5$, 19% have $e > 0.9$ and 10% have $e > 0.95$. In the case of radial anisotropy (see chapter 7), we expect even more stars on highly eccentric orbits because stars with specific

	Offset RA (mas)	Offset Dec. (mas)	Central Mass ($10^6 M_\odot$)	Period (yr)	Peri-Centre Pass. (yr)	Ecc.	Line of Nodes (deg)	Inclination (deg)	Node to Peri-Centre (deg)	Semi-Major Axis (mpc)	Peri-Centre Sep. (mpc)
S2	2.3 ± 1.2(1.6)	−3.1 ± 1.2(1.6)	3.6±0.3(0.4)	15.56±0.35(0.47)	2002.331±0.012(0.016)	0.881±0.007(0.009)	45.0±1.6(2.1)	-48.1±1.3(1.7)	245.4±1.7(2.3)	4.63±0.10	0.55±0.03
	0.0 ± 2.9	0.8 ± 2.0	4.0±0.3	15.02±0.72	2002.34±0.01	0.88±0.01	45.4±1.7	-46.4±1.7	247.1±2.3	4.68±0.17	0.58±0.04
	n.a.	n.a.	3.7±1.5	15.2±1.0	2002.30±0.05	0.87±0.03	36.0±9.0	±46.0 ± 4.0	±250.0 ± 5.0	4.62 ± 0.58	0.60 ± 0.17
S14	n.a.	n.a.	4.4±11.0	14.6±14.1	2000.8±0.6	0.87±0.23	55.9 ± 6.3	±83.1±3.4	204.0±47.5	4.8 ± 2.3	0.6 ± 1.1
	n.a.	n.a.	4.5 ± 0.2	16.0 ± 2.7	2000.9 ± 0.1	0.89 ± 0.04	56.3 ± 0.8	±83.0 ± 0.3	207.0 ± 7.0	5.0 ± 0.5	0.2 ± 0.4
S12	n.a.	n.a.	3.2±1.5	46.2 ± 8.7	1995.5 ± 0.06	0.79 ± 0.03	168.7 ± 1.8	±56.6 ± 2.7	26.7 ± 4.6	9.2 ± 0.8	1.9 ± 0.3
	n.a.	n.a.	3.2 ± 0.05	45.7 ± 1.2	1995.4 ± 0.02	0.790 ± 0.005	168.7 ± 0.2	±56.6 ± 0.2	26.2 ± 0.9	9.1 ± 0.1	1.9 ± 0.05
S1	n.a.	n.a.	3.6 ± 2.0	87.8 ± 18.8	1997.9 ± 2.6	0.33 ± 0.08	155.2 ± 5.6	±56.0 ± 0.0	266.4 ± 26.1	14.7 ± 1.7	9.9 ± 1.7
	n.a.	n.a.	$3.6^{4.2}_{3.2}$	$87.8^{70.1}_{114.8}$	$1997.9^{1997.7}_{1998.0}$	$0.33^{0.22}_{0.44}$	$155.2^{155.2}_{155.3}$	$56.0^{58.0}_{54.0}$	$266.4^{264.8}_{267.2}$	$14.7^{13.2}_{16.8}$	$9.9^{10.3}_{9.4}$
S13	n.a.	n.a.	3.6 ± 1.3	44.3 ± 6.5	2005.8 ± 0.4	0.41 ± 0.04	84.9 ± 46.6	±20.0 ± 0.0	251.8 ± 32.7	9.3 ± 0.6	5.5 ± 0.5
	n.a.	n.a.	$3.6^{3.9}_{3.4}$	$44.3^{39.7}_{838.8}$	$2005.8^{2006.3}_{2002.1}$	$0.41^{0.39}_{0.69}$	$84.9^{92.8}_{69.1}$	$20.0^{7.0}_{42.0}$	$251.8^{253.2}_{223.7}$	$9.3^{8.5}_{70.6}$	$5.5^{5.2}_{7.1}$
S8	n.a.	n.a.	3.4 ± ∞	90.5 ± ∞	1987.6 ± ∞	0.96 ± ∞	151.9 ± ∞	±52.0 ± 0.0	151.0 ± ∞	14.7 ± ∞	0.6 ± ∞
	n.a.	n.a.	$3.4^{2.9}_{3.1}$	$90.5^{116.3}_{97.6}$	$1987.6^{1982.7}_{1987.8}$	$0.96^{0.61}_{0.97}$	$151.9^{127.7}_{155.1}$	$52.0^{77.0}_{46.0}$	$151.0^{212.8}_{150.7}$	$14.7^{16.4}_{14.9}$	$0.6^{6.4}_{0.4}$

Table 8.1: **Parameters of individual orbits near Sgr A*:** *The eleven columns list the orbital parameters and their uncertainties for the stars S2, S14, S12, S1, S13, and S8. All values are given for a GC distance of 7.94 kpc (Eisenhauer et al., 2003).* **S2:** *The three lines list in order the parameters of the orbit of S2 as determined by (Eisenhauer et al., 2003), Ghez et al. (2003), and by Schödel et al. (2002). The errors in line one result from rescaling the errors of the input measurements such that the reduced χ^2 of the fit equals one. The un-scaled errors are given in parentheses. The first two columns list the offsets of the focus of the orbit from the nominal radio position of Sgr A*. They are measured positive to the East and North. The offset of the focus of the orbit as determined by Ghez et al. (2003, astro-ph/0306130) was computed by comparing the offsets of S2 from Sgr A* (and their uncertainties), calculated with the respective orbital elements, at the epoch 2002.3. The uncertainties are larger because they result from quadratically adding the uncertainties of both solutions.* **S14 and S12:** *The first line lists the orbital elements and their formal fit errors. The second line lists the averages and standard deviations of the parameters resulting from 400 repeated fits with random offsets of the focus within the error circle of the focus of the orbit of S2.* **S1 and S13:** *The first line lists the orbital elements of S1 and their formal fit errors for a central mass of $3.6 \times 10^6\ M_\odot$. The second line lists the elements of orbital fits for central masses approximately $1\sigma = \pm 0.3 \times 10^6\ M_\odot$ higher (superscript) or lower (subscript values) than the central mass determined from the orbit of S2.* **S8:** *The first line lists the orbital elements of S8 and their formal fit errors for a central mass of $3.4 \times 10^6\ M_\odot$. This is the highest mass for which the fitting routine converged. The routine could not determine well defined formal errors. The second line lists the elements of the orbital fits from line one (values in the middle) and for two alternative fits, at higher and lower inclinations, with central masses of 2.9 (superscript values) and $3.1 \times 10^6\ M_\odot$ (subscript values).*
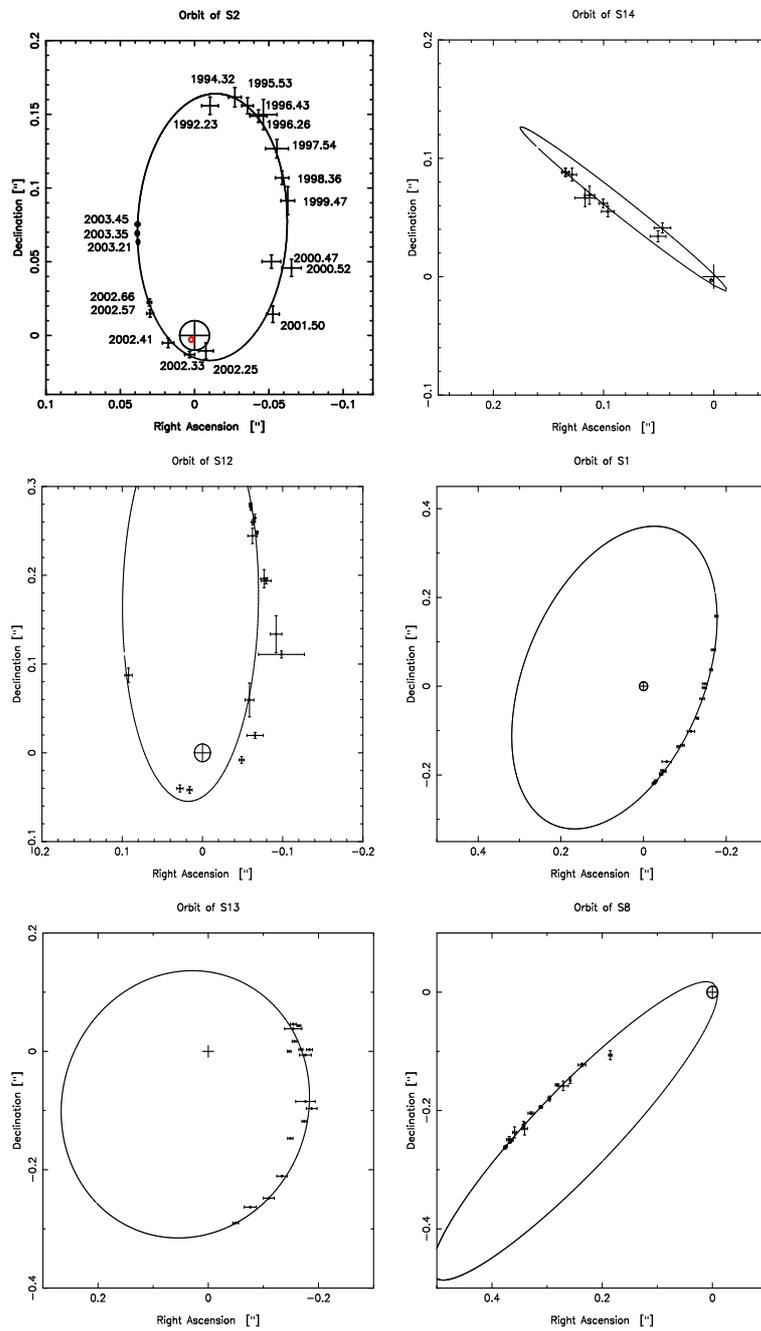
Figure 8.4: **Orbits of individual stars around Sgr A*.** *This plot shows all six orbits of stars around Sgr A* determined in this work. The best fit orbits are over-plotted onto the measured positions and their uncertainties.*
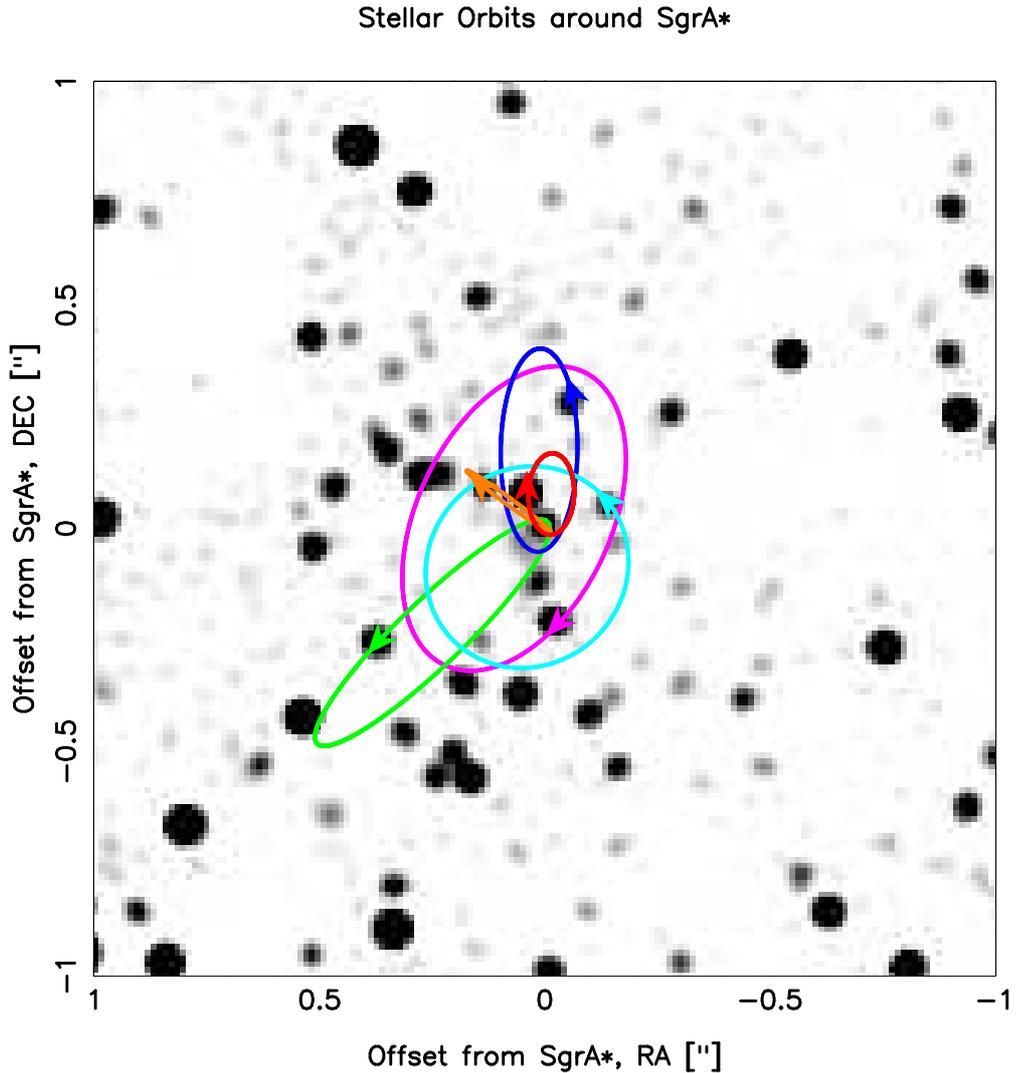
Figure 8.5: **Orbits of stars around Sgr A*.** *Lucy-Richardson deconvolved and beam-restored high-resolution (FWHM~ 60 milliarcseconds) near-infrared (2.2μm) image of the central $1'' \times 1''$ of the nuclear stellar cluster. The image was obtained with CONICA/NAOS at the ESO VLT in June 2003. On this image Sgr A* can be seen in its flaring state (see chapter 10) as a point source at the origin of the coordinate system. The Keplerian orbits of six stars, as they were determined by a decade of continued observations, are over-plotted onto the image. Arrows indicate the locations of the respective stars and their direction of motion. A colour version of this image is shown in Appendix B.*

energies E in an interval $(E, E + dE)$ would have a lower average angular momentum than in the isotropic case. Similarly, we expect a flatter distribution in the case of tangential anisotropy.

In Figure 8.6, we also plotted the cumulative distribution function of the orbital eccentricities that we determined for the stars S1, S2, S8, S12, S13, and S14. For S1, S13, and S8 we chose the eccentricities and their errors from the respective second lines in Table 8.1. Unfortunately, due to the small number of orbits and the large uncertainty in the majority of the determined eccentricities, no clear statement can be made about the isotropy/anisotropy properties of the Sgr A* stellar cluster. On the one hand, one can regard the observed eccen-
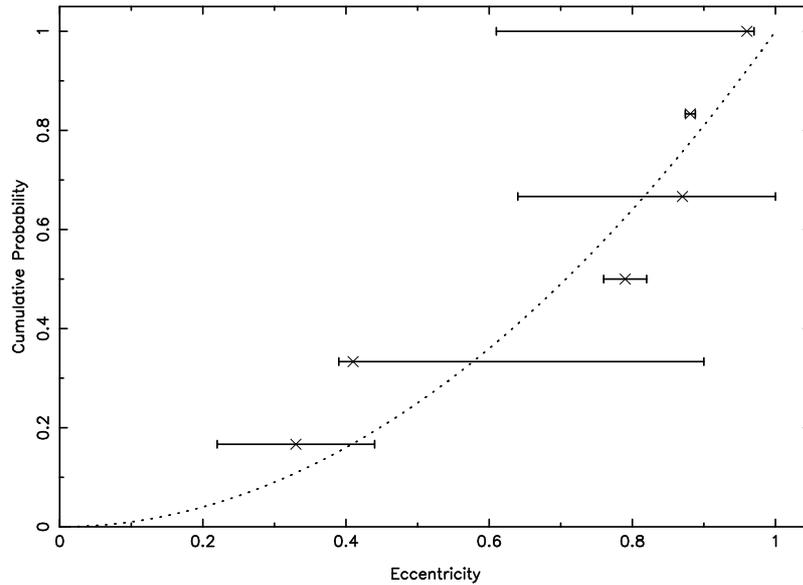
Figure 8.6: **Cumulative distribution function of eccentricities.** *Dotted line: Cumulative probability distribution function of the eccentricities of test particles orbiting a point mass in a spherical, isotropic system. The crosses and their error bars mark the eccentricities measured for the 6 stars S1, S13, S12, S14, S2, and S8 (starting with the lowest eccentricity).*

tricities to be in agreement with an isotropic cluster. On the other hand, one might interpret the steepness of the observed distribution function as a hint toward radial anisotropy. More data are clearly needed.

8.5   On the Possible Eccentricity Bias of the Detected Orbits

In the previous section we saw that we could learn about the anisotropy characteristics of the dense stellar cluster surrounding Sgr A* from the measured eccentricities of the observed orbits. However, at this point the question arises whether there is a bias to detect preferentially circular or highly eccentric orbits.

When observing stellar proper motions/accelerations there is always a given lower limit for the detectable acceleration imposed by the limitations of the telescope, instrument, and generally by the observing technique (e.g. time sampling). Consider two stars on Keplerian orbits of equal energy (equal semi-major axis) around a black hole. The one on the more eccentric orbit will spend less of its time near the black hole where its acceleration is detectable, and its eccentricity will therefore have a smaller probability of being measured. This effect biases the detected eccentricities towards smaller values. On the other hand, as long as $\alpha < 2$ the number of cluster stars per interval da increases with a, where a is the semi-major axis (Appendix eq 4). These more numerous high-a stars can have large detectable accelerations only if their eccentricity is high enough to take them close to the black hole. This effect biases the detected eccentricities toward higher values. Thus, there are two competing trends that may introduce a bias into the measured eccentricity distribution.

In order to obtain a rough quantitative estimate of the possible bias, we modelled families of Keplerian orbits with fixed eccentricities and specific energies. We let their inclination angle i and the angle from node to peri-centre ω (i.e. the rotation of the orbit in the plane of the orbit) vary on grids. ω was varied between 0 and 2π in equal steps of $\pi/6$, while $sin(i)$ was varied in equal steps of 0.1 between -0.9 and 0.9. For each of the individual orbits we calculated the

fraction of the orbital period that the acceleration as seen projected onto the plane of the sky stayed above a given threshold value. We interpreted this fraction as the probability of detecting the given orbit. We chose as detection threshold a minimum acceleration of 1 mas yr^{-2}, a value slightly lower than the lowest detected acceleration in our data sample (star S8). By averaging the probabilities over all angles i and ω, we obtained the overall detection probabilities for orbits with a given semi-major axis a and a given eccentricity e. We assumed an isotropic cluster and that the probability distribution function for e was independent of a. We assumed a time sampling of two observations per year.

That leaves creating an adequate distribution of semi-major axes. We chose a minimum semi-major axis corresponding to an orbital period of $\sim$5 yr, which we consider a realistic value for our data sample. The upper limit for the distribution of semi-major axes is chosen to be 1 pc, roughly the distance over which the black hole dominates over the mass of the stellar cluster. The energy distribution function near a massive black hole has the form

$$f(\epsilon) = A\epsilon^p \quad n_* \propto r^{-3/2-p} \quad p = \frac{M}{4M_2} \tag{8.7}$$

if the stellar population consists of a spectrum of masses $M_1 < M < M_2$, where $\epsilon = -v^2/2 + GM_{BH}/r$ is the specific energy of the star and $f_M \equiv 0$ for $\epsilon < 0$ (Bahcall & Wolf 1977; see also Appendix A). n_* is the stellar number density. The distribution function of semi-major axes $n(a)$ for a given cusp model is then $n(a) \propto a^{1/2-p}$ (see appendix A). We created distributions of semi-major axes (1000 values of a sampled according to $n(a)$ between its minimum and maximum values) corresponding to isotropic power-law stellar cusps with exponents α of -1.0, -1.5, and -2.0. In the case of the Milky Way nuclear cluster the stellar density varies approximately as $n_* \propto r^{-3/2}$ (see chapter 6 and Genzel et al., 2003).

The upper panel of Figure 8.7 shows the probabilities of detecting orbits with a given e and a for the case of a $n \propto -1.5$ cusp. We only plotted the curves for orbits with $a < 100$ mpc because the plot would get extremely crowded at large semi-major axes and because the probabilities for large a are extremely low. For small a, the detection probability is large for all e, while at intermediate a, there is a bias towards less eccentric orbits. This bias turns over at large semi-major axes, when stellar accelerations can only be observed near the peri-centre of highly eccentric orbits. However, for orbits with large a, detection probabilities are extremely low.

By averaging over all semi-major axes we obtained the overall detection probability for orbits with a given eccentricity in a given isotropic cusp model. The results are plotted in the lower panel of Figure 8.7. The exact values of the probabilities depend on the modelling parameters (e.g. on the number of steps when creating the distribution of semi-major axes). However, we are only concerned with the relative probabilities. In the model with $\alpha = -2.0$ the stars are most concentrated toward the centre and therefore the overall probabilities of detecting orbits are highest. In this case, there is no significant overall detection bias for any eccentricity. At the other extreme, in case of $\alpha = -1.0$, there is a bias factor of > 2 for highly eccentric orbits compared to circular orbits. This corresponds to our expectation that the relative weight of more circular orbits should decrease with a decreasing concentration of the cluster. The case of $\alpha = -1.5$, which is closest to the case of the GC stellar cusp, shows some bias toward high eccentricities. However, this bias is modest (factor $1.5 - 2$). Basically, it affects significantly only extreme eccentricities of $e > 0.9$.

With our modelling we wanted to provide a general idea of the possible eccentricity bias involved in detecting stellar orbits around Sgr A*. As for the eccentricities of the stellar orbits found in the present work, we find that all stars have semi-major axes < 20 mpc (with the possible exception of S13). Hence, if there is a bias at all, we are rather in the regime where we are biased towards detecting orbits with low eccentricities.
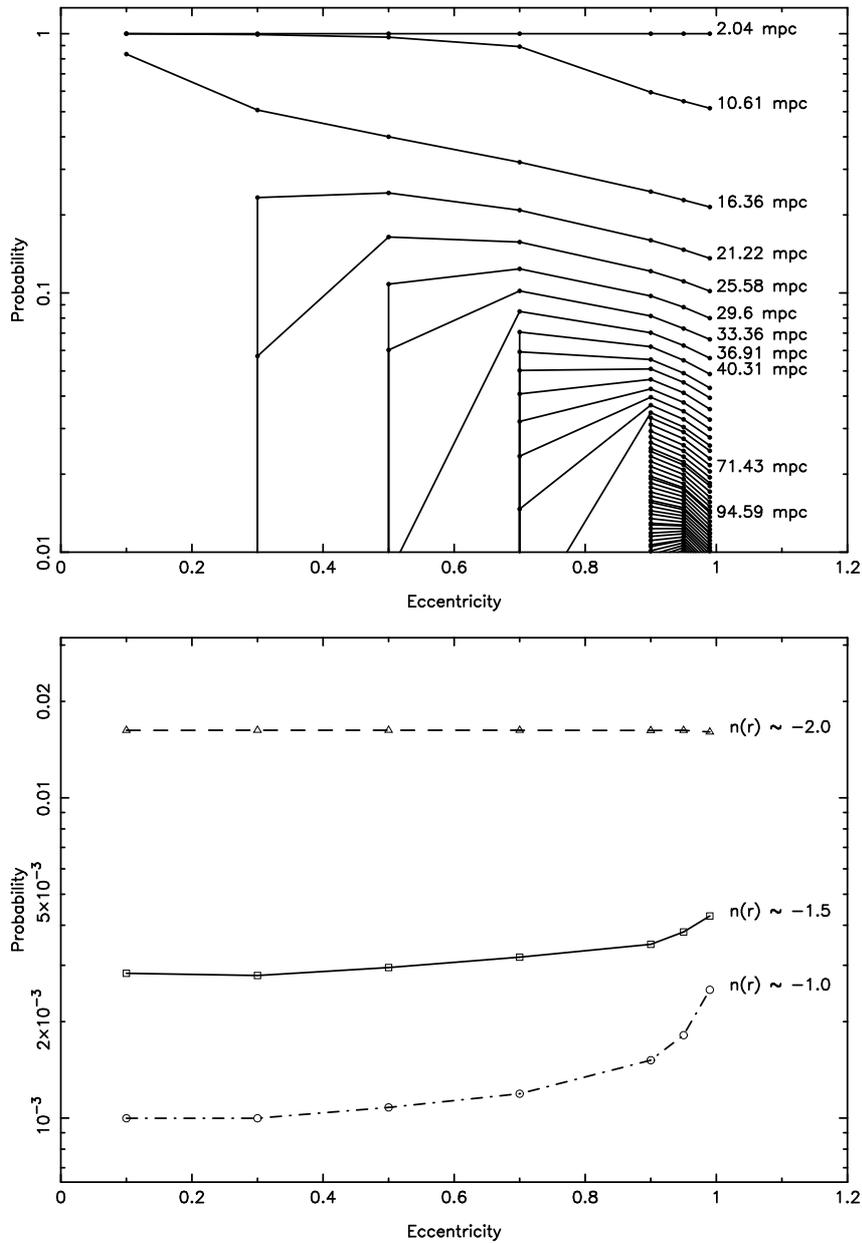
Figure 8.7: **Upper panel: Probability of detecting a Keplerian orbit with a given eccentricity** e **and semi-major axis** a**.** *The distribution of semi-major axes corresponds to the case of an isotropic stellar power-law cusp surrounding Sgr A*. A stellar density law of* $n_* \propto r^{-3/2}$ *has been assumed (chapter 6; Genzel et al., 2003). Values of the semi-major axes are given in the labels to the right of the curves. See text for explanations concerning the model leading to the respective probabilities. Curves for semi-major axes* > 100 *mpc were not plotted in order to avoid over-crowding the plot.* **Lower panel: Overall detection bias of orbits with a given eccentricity assuming a power-law stellar cusp at the centre of the Milky Way.** *The assumed exponents of the power-law cusps are plotted beside the corresponding curves. The probabilities were obtained after averaging over the detection probabilities for given distributions of semi-major axes such as shown in the upper panel. The overall low probabilities result from the fact that the overwhelming majority of the stars have large semi-major axes.*

Chapter 9

The Nature of Sagittarius A*

As exposed in the previous chapters, the continued observations of the central stellar cluster of the Milky Way have accumulated a wealth of information on the gravitational potential near the non-thermal radio source and black hole candidate Sgr A*. Sgr A* appears to be located at the dynamical centre of the nuclear stellar cluster and to be associated with a dark mass of the order 3 to 4×10^6 $M_\odot$. We will summarise the results of our NIR observations of stellar dynamics in this chapter and combine them with the results of earlier or parallel works (e.g. other works on stellar dynamics, radio and X-ray observations of Sgr A*). We will find that the accumulated evidence leaves hardly any room for doubt on the nature of Sgr A*: It is most likely a supermassive black hole of $3.6 \pm 0.3 \times 10^6$ $M_\odot$, located at the dynamical centre of the Milky Way.

9.1 The Enclosed Dark Mass in the Central Parsec

As we have showed in chapters 7 and 8, the analysis of the stellar dynamics in the central arc-second (or roughly 40 mpc) around Sgr A* provides clear evidence for the presence of 3 to 4 million solar masses of dark mass at the centre of the cluster. The observation of individual orbits sets strong limits on the volume in which this mass must be located : When passing through the peri-centre of its orbit the star S2 was at a mere 0.55 mpc or about 15.6 light hours distance from Sgr A*. Moreover, its orbit tells us that the radio source Sgr A* and the focus of the orbit are coincident (within an uncertainty of just a few milli-arc-seconds). This conclusion is even valid if one drops the assumption of Keplerian orbits (N. Mouawad, priv. comm., 2003, paper in preparation).

Figure 9.1 summarises a great number of measurements of the dynamical mass in the centre of the Milky Way, from early gas dynamical observations to recent observations of stellar orbits. It is based on the well known plot of enclosed mass vs. distance, introduced by Genzel & Townes (1987) (for more recent versions of this plot see also e.g. Genzel et al., 1996; Genzel et al., 2000; Schoedel et al., 2002, 2003). As can be seen in Figure 9.1, the different estimates based on stellar velocity dispersion (in part using the same or similar data) agree within their uncertainties but the variations show the sensitivity to the input assumptions. In contrast, the orbital technique is much simpler and less affected by the assumptions.

The plot shows that the gravitational potential is dominated by a point mass from distances of 0.5 pc down to less than a light day from Sgr A*. Fitting a model composed of a point mass plus the visible stellar cluster with a core radius of 0.46 pc and a power-law slope of $\alpha = 1.7$ to the data gives a value of $3.35 \pm 0.15 \times 10^6 M_\odot$ for the central point mass. In principle, one could replace the central point mass by a very compact, extended dark mass component. If we choose a Plummer model (which has the advantage of being fully integrable) for the density

distribution, $\rho(r)$, of such a hypothetical cluster,

$$\rho(r) \propto \frac{1}{(1 + \frac{r^2}{R^2})^{-5/2}}, \tag{9.1}$$

where r is the three-dimensional and R the projected distance from Sgr A*, then we obtain a required central density of $1.6 \times 10^{18} \text{M}_\odot \text{ pc}^3$.

The mass of Sgr A* can also be constrained via its proper motion measured by radio astronomical observations. Reid et al. (2003a) find an upper limit of 8 kms^{-1} for the intrinsic proper motion of Sgr A*. Following their argument, we can apply equipartition of momentum to the case that the black hole is perturbed by close passages of stars. For S2, with a mass of $\sim$ 15 M$_\odot$ and a velocity of $\sim$ 7000kms^{-1} at peri-centre, we find a lower mass limit of 13×10^3 M$_\odot$ for Sgr A*. Dorband, Hemsendorf & Merritt (2003) model the Brownian motion that a supermassive black hole would have embedded in the stellar cluster at the centre of the Milky Way. From their equation (73) and with the above proper motion constraint, we calculate a minimum mass of 7.5×10^3 M$_\odot$ for Sgr A*. Carrying the argument a bit further, we can interprete the upper limits on the size of Sgr A* at millimetre wavelengths as its half mass diameter. Assuming a half mass radius of $r_h \leq 0.1$mas (Doeleman et al., 2001; Rogers et al., 1994; Melia & Falcke, 2001) we obtain with the above mass estimates

$$\rho_{SgrA*} \geq \frac{7.5 \times 10^3 \text{M}_\odot/2}{(4\pi/3)r_h^3} > 3 \times 10^{19} \text{M}_\odot\text{pc}^{-3} \tag{9.2}$$

The upper limit on the proper motion of Sgr A* relative to the surrounding star cluster thus gives the overall highest mass density constraint.

9.2 Models for Sagittarius A*

Several models for the nature of Sgr A* have been suggested. The availability of mass measurements from several pc down to less than a light day as well as radio, X-ray and NIR (see next section) observations of Sgr A* can be used to choose the most probable one. We will discuss the proposed models in the following subsections.

9.2.1 Dark Cluster

One working hypothesis is that the bulk of the mass associated with Sgr A* is in the form of a dense cluster of dark astrophysical objects, such as neutron stars or white dwarfs. If we assume a Plummer model cluster of such objects instead of a central point mass, then the current data demand that its central density must exceed $1.6 \times 10^{18} \text{M}_\odot\text{pc}^{-3}$ as shown in Figure 9.1. The lifetime of such a cluster is limited due to evaporation processes to $\ll 10^5$ years (Maoz, 1998). Comparing this short time span to the life time of our galaxy makes such a configuration appear extremely unlikely.

9.2.2 Fermion Ball or Boson Star

A ball of massive, degenerate fermions, such as neutrinos, has been suggested for explaining the concentration of dark mass seen at the GC (e.g. see Tsiklauri & Viollier, 1998; Munyaneza & Viollier, 2002; Bilić et al., 2003). The self-gravity of a ball of degenerate fermions can be balanced by the degeneracy pressure of the fermions due to the Pauli principle. In this case, the relation between the mass M and the radius R of a fermion ball, composed of fermions with mass m and degeneracy g, can be described by the non-relativistic Lane-Emden equation ('ld' in the equation below means light days):

$$R = \left[\frac{91.869\hbar^6}{m^8 G^3} \left(\frac{2}{g} \right)^2 \frac{1}{M} \right]^{1/3} = 3610.66 \quad \text{ld} \left(\frac{15\text{keV}}{mc^2} \right)^{8/3} \left(\frac{2}{g} \right)^{2/3} \left(\frac{M_\odot}{M} \right)^{1/3} \tag{9.3}$$
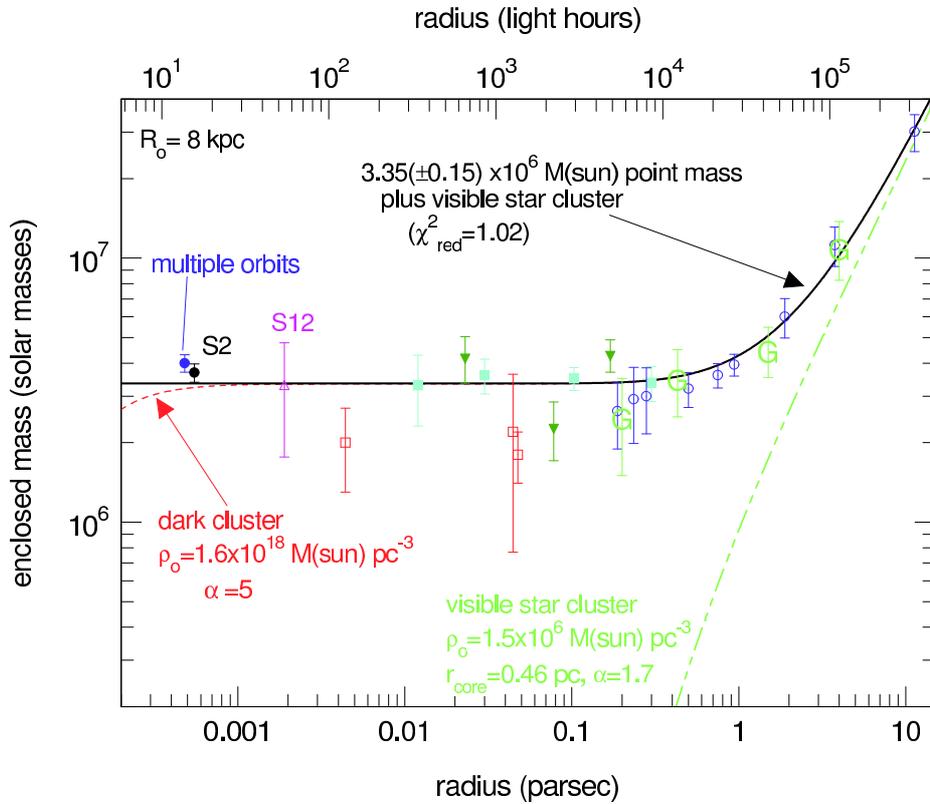
Figure 9.1: **Mass distribution in the galactic centre.** *Enclosed mass vs. distance from Sgr A* in the GC, assuming a distance of 8 kpc (Reid, 1993). The circles at the shortest projected distances denote the masses derived from a fit of multiple orbits by Ghez et al. (2003, astro-ph/0306130) and from the orbits of S2 and S12 (this work). Filled down pointing triangles denote Leonard-Merritt projected mass estimators from the present work (at 0.025 pc) and from a new NTT proper motion data set by Ott (2003), separating late and early type stars, and correcting for the volume bias determined from Monte Carlo modelling of theoretical clusters and assuming a central density profile with a power-law slope of $\alpha = 1.4$ (Genzel et al., 2003). An open down-pointing triangle denotes the Bahcall-Tremaine mass estimate obtained from Keck proper motions (Ghez et al. 1998; we multiplied their error bar by a factor of 2 in order to take possible systematic errors into account). Filled rectangles are mass estimates from a parameterised Jeans-equation model, including effects of anisotropy and differentiating between late and early type stars (Genzel et al., 2000). Open circles are mass estimates from a parameterised Jeans-equation model of the radial velocities of late type stars, assuming isotropy (Genzel et al., 1996). Open rectangles denote mass estimates from a non-parametric, maximum likelihood model, assuming isotropy and combining late and early type stars (Chakrabarty & Saha, 2001). Letter "G" points denote mass estimates obtained from Doppler motions of gas (Genzel & Townes, 1987). The straight continuous curve is the overall best fit model to all data. It is the sum of a $3.35 \pm 0.15 \times 10^6 \, M_\odot$ point mass, plus a stellar cluster of central density $1.5 \times 10^6 M_\odot pc^{-3}$, core radius 0.46 pc and power-law index $\alpha = 1.7$. The grey long dash-short dash curve shows the same stellar cluster separately, but for an infinitely small core. The dashed curve is the sum of the visible cluster, plus a Plummer model of a hypothetical very compact dark cluster of central density $1.9 \times 10^{18} M_\odot pc^{-3}$. For a colour version of this Figure see Appendix B.*

In the case of the GC, the orbit of S2 tells us $M = 3.6 \times 10^6$ M$_\odot$ and $R = 0.00055$ pc= 0.655 ld. Therefore, we obtain as a minimum fermion mass 48 keV for $g = 4$ and 57 keV for $g = 2$.

The maximum mass of a degenerate fermion ball is given by the Oppenheimer-Volkoff limit

$$M_{OV} = 0.38322 \frac{M_{Pl}^3}{m^2} \left(\frac{2}{g}\right)^{1/2} = 2.7821 \times 10^9 \quad \text{M}_\odot \left(\frac{15 \quad \text{keV}}{mc^2}\right)^2 \left(\frac{2}{g}\right)^{1/2}, \quad (9.4)$$

where $M_{Pl} = (\hbar c/G)^{1/2} = 1.2210 \times 10^{19}$ GeV is the Planck mass. For a given fermion mass m all objects heavier than M_{OV} must be black holes. In case of the GC, the Oppenheimer-Volkoff limit gives us maximum fermion masses of 351 keV for $g = 4$ and 417 keV for $g = 2$.

This means that in the case of the concentration of dark mass seen at the centre of the Milky Way, the minimum required fermion mass is 48 keV, while the maximum allowed mass is 417 keV. The most massive central dark object currently known is located at the centre of M87 (Kormendy, 2003), with a mass of $> 3 \times 10^9$ M$_\odot$. In this case, the maximum mass derived from the Oppenheimer-Volkoff limit is 14 keV. Hence, we can definitely exclude that all the known dark mass concentrations in the centres of galaxies can be explained by a single fermion ball model. This means we are left with a model, where smaller concentrations of dark matter could be accounted for by fermion balls, whereas larger objects must be black holes. The fermion balls could, for example, be composed of sterile neutrinos (Bilić et al., 2003). However, if we take the mass density for Sgr A* derived from the size constraints of radio interferometry (see above), we obtain a minimum allowed fermion mass of 311 keV, which is very close to the maximal allowed fermion mass.

One major difficulty of the neutrino ball model is that baryonic accretion by the mass concentration cannot be avoided, which should again lead to the formation of a black hole. Also, if there is a seed black hole inside a fermion ball, the latter might be absorbed by the black hole within time scales that are short compared to the Hubble time.

Observations of X-ray flares (Baganoff et al., 2001) and NIR flares (Genzel et al., 2003) show that Sgr A* must be a very compact object: The variability time scales point to a size of less than ten Schwarzschild radii of a 3.6×10^6 M$_\odot$ million solar mass black hole. This corresponds to 3.4^{-6} pc. This is two orders of magnitude smaller than the radius of a corresponding neutrino ball, R_{NB} when assuming a neutrino mass of 48 keV ($R_{NB} = 5.5 \times 10^{-4}$ pc). Hence, the flares from Sgr A* suggest that it must be significantly more compact than the hypothetical neutrino ball.

Experiments in the near future will provide strong constraints on the accretion and emission mechanism of Sgr A*. Since accretion onto a fermion ball and onto a black hole can be distinguished by the steepness of the potential well, such observation should be able to decide between the two models.

A model similar to the degenerate fermion ball is the boson star model (see e.g. Torres, Capozziello, & Lambiase, 2000). Such an object could consist, for example, of Higgs particles and would indeed be almost as compact as a black hole. The main problem with this model is that it would be hard to understand how the bosons could reach such a compact configuration in the first hand and then avoid the collapse to a black hole through baryonic accretion.

We conclude that the fermion ball or boson star models are unlikely explanations for the dark mass concentration at the centre of the Milky Way.

9.2.3 Supermassive Black Hole

The supermassive black hole model has been suggested for Sgr A* soon after its discovery. The existence of supermassive black holes was originally postulated to explain the extreme energy output at all wavelengths and the short term time variability of the emission of quasars and AGN. In the case of the Milky Way, Sgr A* can be regarded as an example of a quiescent

galaxy nucleus. A supermassive black hole model fulfils all of our observational constraints: It is a stable and extremely compact configuration and provides the steep gravitational potential needed for explaining the radio emission of Sgr A* (Melia & Coker, 1999) as well as the small spatial scales needed for the variability of the X-ray and NIR flares (see later in this chapter) on minute time scales. The lower mass limit to Sgr A*, inferred from radio interferometric limits on its proper motion relative to the surrounding star cluster, requires that the compact ($R \leq 1$ AU) radio source Sgr A* must have a minimum mass of several thousand solar masses. This adds considerable weight to the black hole hypothesis.

As for a tight (< 10 light hours separation) binary black hole with similar masses of its two components, it would coalesce by gravitational radiation within a few hundred years (B.F. Schutz 2003, private communication). A binary black hole of larger separation should lead to the preferential ejection or destruction of stars on radial orbits and thus to a depletion of such orbits and tangential anisotropy of the stellar cluster (Gebhardt et al., 2003). This is not observed in the GC (see chapter 7).

We conclude that the most likely explanation for the dark mass at the GC is the presence of a single, supermassive black hole, located at the dynamical centre of the stellar cluster (concerning the last point, see also Reid et al., 2003; Reid et al., 2003a; Ghez et al., 2003a). The radio, X-ray, and NIR source Sgr A* then can be interpreted as the manifestation of matter accreted onto or ejected from the vicinity of this black hole (for an overview of accretion/jet emission models see Melia & Falcke, 2001). Our conclusion provides strong support for the standard paradigm that supermassive black holes reside in the nuclei of almost all galaxies.

Chapter 10

NIR emission from Sgr A*

Ever since the start of NIR observations of the GC one of the primary goals was to observe a counterpart of Sgr A* a these wavelengths and examine its properties. However, contrary to AGN, Sgr A* is remarkably faint at wavelengths beyond sub-mm radiation. Due to its faintness in the NIR and the extreme crowding of stellar sources in the central arc-second of the cluster, no counterpart of Sgr A* could be reliably identified in the NIR regime during the high-resolution NIR observational campaigns started in the early 1990s. This situation finally changed in 2003, when both the MPE and UCLA groups reported detection of a variable source at the location of Sgr A* at wavelengths of 2.2 and 1.7μm (MPE) as well as at 3.8μm (MPE and UCLA). While NIR observations of the GC were previously mainly dedicated to confirming the black hole nature of Sgr A* via stellar dynamics, the properties of this supermassive black hole and its emission and accretion mechanisms can now be studied directly at NIR wavelengths.

10.1 Observations

During H-band (1.66μm) observations of the GC with NACO at the VLT on May 9, 2003 (UT), a flaring source was detected at the position of Sgr A* (Figure 10.1). The position of the flare was offset a mere -1.4 ± 3.0 mas in R.A. and -0.2 ± 3.0 in Dec. from the dynamical position of Sgr A* as it was determined from the orbit of the star S2. It lasted for about 30 min and its rise and decay can be well fitted by an exponential with a time scale of 5 min. Since the light crossing time of a 3.6 million solar mass black hole is 35 s, this rapid variability corresponds to a spatial scale of less than 10 Schwarzschild radii of such an object.

Subsequent observations with NACO/VLT in June 2003 and an examination of earlier VLT data with respect to variability of Sgr A* produced further observations of Sgr A* flares, at wavelengths of 3.8, 2.2, and 1.7μm. The strength and duration of the flares and their astrometric positions are listed in Table 10.1. The light curves of the flares are shown in Figure 10.2. The photometry of the flares was measured on the individual images with exposure times ranging between 20.0 and 60.0 s (see Table 4.2). The images were LR deconvolved and beam restored. The flux of Sgr A* and its error were measured relative to the known magnitudes of nearby stars (taken from the Ott 2003 list) by using circular apertures of different sizes. The positions of the flares and their uncertainties were measured relative to the position of stars from the Ott 2003 list on linear and LR deconvolved sum images. The same procedure was used for measuring the quiescent flux and position of Sgr A*.

10.1.1 Properties of the NIR source Sgr A*

In the past decade, only upper limits for the NIR flux of Sgr A* could be determined and putative detections (e.g. Genzel et al., 1997) could not be reproduced. The observation of a
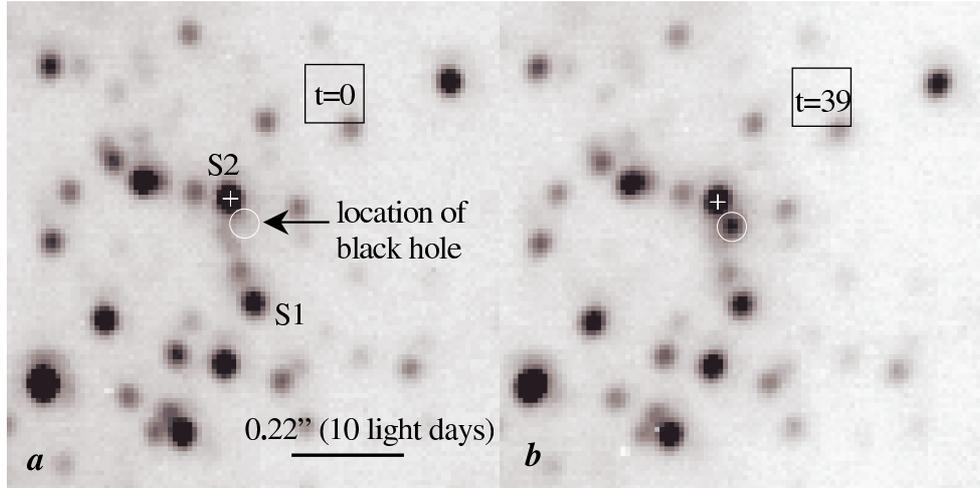
Figure 10.1: **Detection of NIR emission from Sgr A*.** *The images show raw AO images (60 s total exposure time) of an area* $\sim 1'' \times 1''$ *around Sgr A*, observed on May 9, 2003 UT. The left image was taken at the beginning of the observations, the right image about 40 min later. The flaring source is easily detected in the right image. Its position is offset* -1.4 ± 3.0 *mas in R.A. and* -0.2 ± 3.0 *in Dec. from the dynamical position of Sgr A* as it was determined from the orbit of the star S2. The star S2 is marked by a cross, the position of Sgr A* is indicated by a white circle. This Figure corresponds to Figure 1 in Genzel et al. (2003a).*

Band	Date	ΔRA	ΔDec	Duration	Variability
	[UT]	[mas]	[mas]	[min]	
L'	2002.66	0(30)	0(30)	≥ 15	0.7
H	2003.353	-1.4(3.0)	-0.2(3.0)	30	4.7
K_S	2003.455	-2.5(4)	3.4(4)	80	3.1
K_S	2003.457	-6.4(4)	2.5(4)	85	3.2

Table 10.1: **List of Sgr A* flares.** *The offsets in right ascension and declination refer to the astrometric position of Sgr A* as it was inferred from the focus of the orbit of the star S2. The duration of the flares refers to the full width at zero maximum, the variability factor to the ratio between the excess emission to the 'quiescent' emission.*

NIR source at the position of Sgr A* was particularly difficult since about 1999 because stars such as S2 and S14 approached Sgr A* to projected distances $< 50 - 100$ mas (for comparison, the diffraction limited beam FWHM at the NTT in the K-band is 130mas). Scḧodel et al. (2003) examined ten years of SHARP/NTT data and found no evidence for a varying and/or stationary source at the position of Sgr A*, when taking into account possible time scales of hours to days. They constrained the peak magnitude of possible flares on shorter time scales to less than $K = 13.5$.

The flares recently detected with NACO/VLT in 2003 fulfil all these constraints; additionally, a 'quiescent' NIR source at the position if Sgr A* could be detected as well (Genzel et al., 2003a). In summary, the properties of the NIR flares of Sgr A* are:

- **Brightness:** Peak brightnesses of the flares in K-band of about $K = 15.0$, comparable to the brightness of the star S1 near Sgr A*.
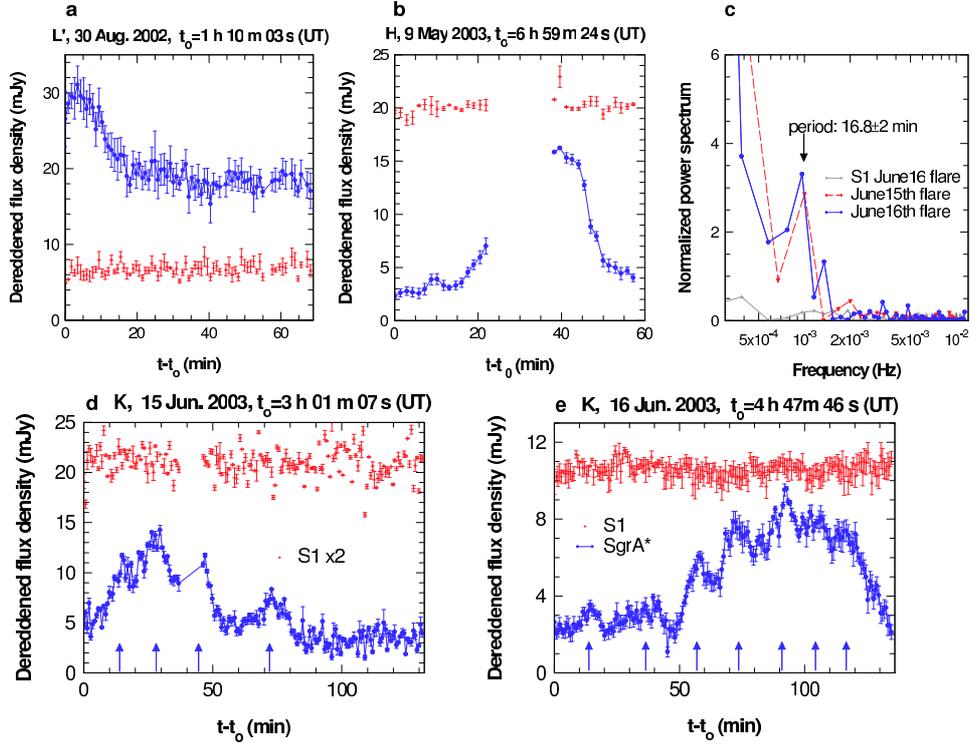
Figure 10.2: **Light curves of Sgr A* NIR flares.** *Light curves of the Sgr A* NIR flares in 2002 and 2003, observed with NACO/VLT. The L-band flare on August 30, 2002, was only partially covered by observations. Gaps in the time series of the H-band flare on May 10, 2003, and of the K-band flare on June 15, 2003, are due to sky observations and instrument failure, respectively. For comparison, the steady emission of the star S1 near Sgr A* is shown in all the plots (light grey data points). Arrows in the plots of the two K-band flares indicate substructure peaks of the flares. Both K-band flares show very similar quasi-periodicity, although the second flare was observed more than 24 h after the first one and must thus have been an unrelated event. The upper right panel shows the normalised power spectrum of the two K-band flares. Both of them show a significant peak at a frequency corresponding to time scales of 16.8 ± 2.0 min. In both cases, the power spectrum of S1 does not show such a frequency. This Figure corresponds to Figure 2 in Genzel et al. (2003a). For a colour version of this Figure see Appendix B.*

- **Duration:** A duration of the flares of ≤ 85 min.

- **Time scales:** Short rise-and-fall time scale of the flares, of the order 5 min.

- **Position:** The position of the flares is within a few milli-arc-seconds of the dynamical position of the dark mass as inferred from the orbit of S2 (see Table 10.1). The position of the quiescent source has a larger uncertainty, of the order 10 mas (mainly because of its faintness and confusion with stellar sources), but is still consistent with the dynamical position of the black hole.

- **Intrinsic quasi-periodicity of the flares:** The two K-band flares, which were completely covered by observations, display a characteristic quasi-periodic substructure, with a period of 16.8 ± 2.0 min (see plot of power spectrum in Figure 10.2). The

observed 'quiescent' flux was also variable. There are some indications of quasi-periodicity of the quiescent state of Sgr A*, with periods between 20 and 30 min, but this evidence is still ambiguous.

It is highly improbable that the observed variability was due to a stellar source because of the extremely short time scales of the flares, and because of the astrometric positions of the flares, that were always within < 10 mas of Sgr A* at the different epochs: A star close to Sgr A* would have moved by $\sim 20 - 50$ mas during the time interval covered by the four flares (compare with the orbit of S2); a star at greater distances from Sgr A* would have an extremely low probability of being located so close in projection to Sgr A*. The estimated flaring rate is very high: We found 4 flares within a total of 25 hours of observations. Assuming Poisson statistics, we estimate 2 to 6 flares per day. This high frequency and the complex temporal substructure of the light curves rule out the possibility that the flares were related to micro-lensing of cusp stars by the black hole (Alexander & Sternberg, 1999).

As for the relation between the NIR flares and variability at other wavelengths, the durations, rise-and-decay times, and band luminosities of X-ray flares are similar (see e.g. Baganoff et al., 2001 and Figure 10.3). The NIR flare rate, however, was almost twice as high as the X-ray flare rate during Chandra monitoring in 2002 (1.2 ± 0.4 flares per day; Baganoff, 2003a). At the moment, it is not clear whether this points to a physically distinct nature of the two kinds of flares or whether this was related to an overall change of the variability of Sgr A* at different epochs. Simultaneous observations are needed to determine the relation between the X-ray and NIR flares. The millimetre/sub-millimetre radiation from Sgr A* was found to be variable on time scales of several days to a few hundred days (Zhao et al., 2003; Miyazaki et al., 2003), but not on shorter time scales, with the exception of a one hour, 30% amplitude event seen in March 2000 at a wavelength of 2 mm (Miyazaki et al., 2003).

10.2   Sgr A* Flares: Individual Accretion Events?

Figure 10.3 summarises the radio to X-ray spectral energy distribution (SED) of the emission from Sgr A* for both quiescent and flaring states. The quiescent infrared flux densities lie approximately on the extrapolation of the millimetre/sub-millimetre synchrotron emission to high energies, in accordance with a standard power-law synchrotron SED (Liu & Melia, 2001; Markoff et al., 2001; Yuan et al., 2002, 2003). However, models with only a thermal population of electrons (Liu & Melia, 2001; Yuan et al., 2002) under-predict the infrared emission. Models with an additional power-law component of energetic ($\gamma_e = E_e/m_e c^2 \geq 10^{2.5}$), non-thermal electrons (Yuan et al., 2003) come closer to, but still under-predict the observed NIR flux densities.

The NIR flares may arise from synchrotron emission as well, if turbulence, magnetic reconnection or shocks effectively accelerate significant fractions of the electron population to energies with $\gamma_e \geq 10^3$. In that case, the increased emission is due to an acceleration event, similar to solar flares. Models with suitably up-scaled fractions of very energetic electrons may account for the luminosities/fluxes of the infrared flares and of the quiescent emission.

Although we do not have simultaneous observations of the NIR flares at different wavelengths, our data may suggest that the flares have a bluer colour compared to the quiescent emission (Figure 10.3). If the blue colour should prove to be true, an alternative model is needed to explain the nature of the NIR flares. In that case, the NIR radiation may be thermal bremsstrahlung or blackbody radiation from a component of moderately hot gas (temperatures in excess of a few times 10^3 K). The flares would then be associated to individual accretion events of very dense gas, with a total energy release of $\geq 10^{39.5}$ erg. Assuming a radiation efficiency of the order 10%, such as expected in a thin disk, this would correspond to a rest mass of a few times 10^{19} g, comparable to that of a comet or a small asteroid. The observed radio/sub-millimetre radiation in this model would come from a jet or else the optical thickness
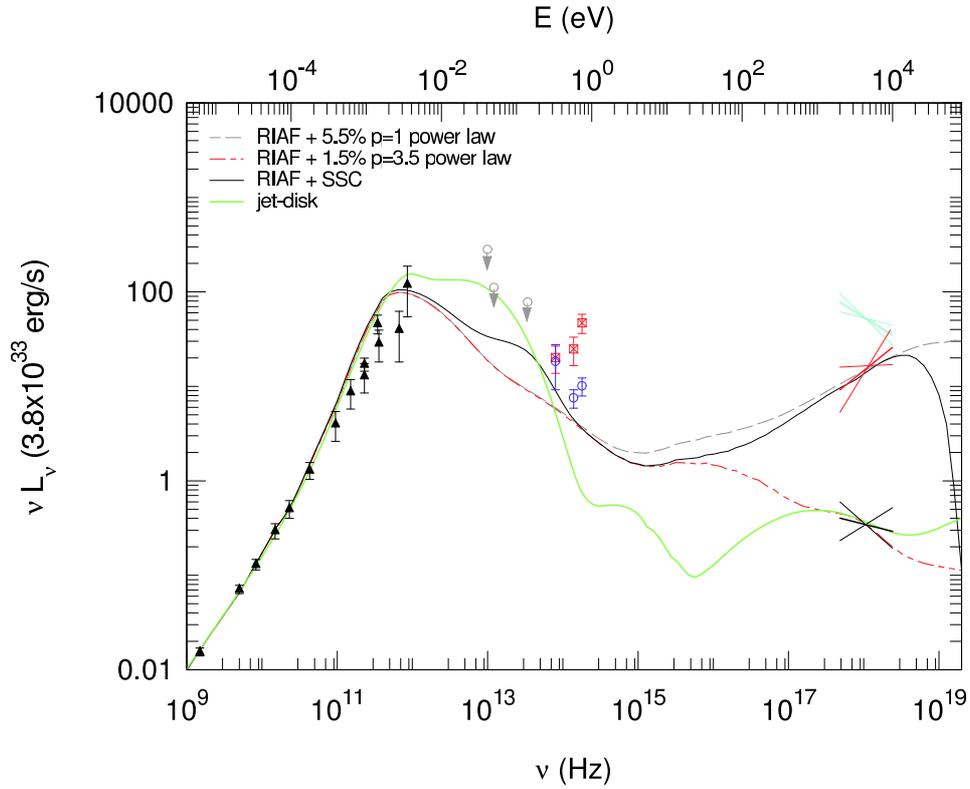
Figure 10.3: **Spectral energy distribution of the emission from Sgr A*.** *This plot shows the extinction and absorption corrected luminosities νL_ν (energy emitted per logarithmic energy interval), with the observed flux density $S_\nu = L_\nu/4\pi D^2$, where $D = 7.94$ pc is the GC distance. All error bars are $\pm 1\sigma$ and include statistical and systematic errors. Black triangles denote the radio spectrum of Sgr A* (Markoff et al., 2001; Zhao et al., 2003). Open grey circles mark various infrared upper limits from literature (Markoff et al., 2001). The three X-ray data ranges are (from bottom to top) the quiescent state as determined with Chandra (black; Baganoff et al., 2003), the autumn 2000 Chandra flare (red; Baganoff et al., 2001), and the autumn 2002 flare observed by XMM (light blue; Porquet et al., 2003). Open red squares with crosses mark the de-reddened peak emission (minus quiescent emission) of the four NIR flares, listed in Table 10.1. Open blue circles mark the de-reddened H, K, and L luminosities of the quiescent state, derived from the local background subtracted flux density of the point source at the position at Sgr A*,thus eliminating the contribution from extended, diffuse light due to the stellar cusp around Sgr A*. The thick green solid curve is the jet-starved disk model by Yuan et al. (2002). The red long dash-short dash curve is a radiative inefficient accretion flow (RIAF) model of the quiescent emission, where in addition to the thermal electron population of Yuan et al. (2002) 1.5% of the electrons have a non-thermal power-law energy spectrum of exponent $p = -3.5$ (Yuan, Quataert, & Narayan, 2003, astro-ph/0304125). The black thin solid curve is a RIAF model of the flares with 5.5% of the electrons in a power-law of $p = -1$ (Yuan, Quataert, & Narayan, 2003, astro-ph/0304125). The long-dash thick curve is a RIAF flare model of the flares with a synchrotron-self Compton component (Yuan, Quataert, & Narayan, 2003, astro-ph/0304125). This Figure corresponds to Figure 3 in Genzel et al. (2003a). For a colour version of this Figure see Appendix B.*

for these wavelengths would have to be very high. Polarisation measurements and simultane-ous multi-wavelength observations will be required for distinguishing between the possible models. In any case, the properties of the observed flares (location within a few milli-arc-seconds of Sgr A*, temporal substructure) are serious difficulties for models that involve large scale structures, such as rapid shock cooling of a large-scale jet or the passage of stars through a cold accretion disk (Nayakshin et al., 2003).

10.3   A Spin Measurement of the Black Hole?

The Schwarzschild radius (R_S) of a $3.6 \times 10^6 \, M_\odot$ black hole is just 35 s across. The short rise-and-decay times of the NIR flares thus are consistent with their origin in a region not larger than 10 R_S, i.e. in the innermost accretion zone. The quasi-periodicity that was observed in the two K-band flares could not be observed in the other flares due to lack of complete coverage. However, the fact that the two flares observed in K-band happened more than 24 h apart but show the same periodicity within the errors of the analysis, strongly suggests that the periodicity may be a repeatedly occurring feature. As for possible frequencies in the accretion zone of the supermassive black hole, acoustic waves in a thin disk (Nowak et al., 1997), Lense-Thirring or orbital node precession are too slow for explaining the short modulation of the flares (Bardeen et al., 1972).

Therefore, the most likely interpretation of the 17-min periodicity is the relativistic mod-ulation of the emission of gas orbiting in a prograde disk just outside the last stable orbit (LSO) of a spinning (Kerr) black hole. The LSO period of a non-spinning black hole of $3.6 \times 10^6 \, M_\odot$ is 27 min. However, the LSO has a smaller radius for a spinning black hole. From the observed period of 17 min we determine a spin parameter $a = J/(GM_{BH})/c = 0.52(\pm 0.1, \pm 0.08, \pm 0.08)$, where G is the gravitational constant, M_{BH} the mass of the black hole, J its spin, and c the speed of light. The errors in brackets include the influence of the un-certainties of M_{BH}, the flare modulation frequency, and the distance to the GC. The observed spin parameter corresponds to half the maximum value for a Kerr black hole.

Recent numerical simulations of the accretion of gas in disks around Kerr black holes indicate that a (prograde) disk analysis is appropriate to first order even for the hot accretion flow at the GC (De Villiers et al., 2003). De Villiers et al. (2003) also show that the gas radiates most efficiently just outside the last stable orbit. This means that the measured spin parameter can be considered a lower limit. Lense-Thirring precession and viscous (magnetic) torques will force the accreting gas into the equatorial plane of the black hole (Bardeen & Pettersen, 1975).

H- and K-band time series of the quiescent emission from Sgr A* observed with NACO/VLT in 2003 indicate that the quiescent emission might have an intrinsic period be-tween 25 and 30 min (Genzel et al., 2003a). However, more observations are needed to assess the significance of this feature.

Should follow-up observations confirm the observed periodicities, then observations of Sgr A* will open the field for direct measurements of the physical properties of the supermas-sive black hole in the centre of the Milky Way.

Chapter 11

Summary

The centre of the Milky Way presents one of the most rewarding astronomical targets because it represents the closest galaxy nucleus accessible to observations. Its central non-thermal radio source Sgr A* has been considered a possible counterpart of a supermassive black hole since its discovery in the early 1970s. Sgr A* and the central parsec with its extremely dense stellar cluster can be considered as an exemplary model of a quiescent galaxy nucleus. In the present work we have presented high-resolution near-infrared observations of the nuclear star cluster that were obtained at the diffraction limit of 4-8 m-class telescopes.

In this thesis we could successfully build up on earlier work on stellar dynamics near Sgr A* that had brought already substantial evidence that Sgr A* was indeed a supermassive black hole (Genzel et al., 1996, 1997; Ghez et al., 1998; Genzel et al., 2000; Ghez et al., 2000; Eckart et al., 2002). We determined unique Keplerian orbits for several individual stars around Sgr A*. The orbit of the star S2 allowed three fundamental measurements (Schödel et al., 2002, 2003; Eisenhauer et al., 2003): a) The mass density of the enclosed dark mass largely excludes any alternative explanations for the nature of this mass, but a black hole; b) The position of the dynamical centre of the orbit is coincident with the non-thermal radio source Sgr A*; c) The orbit of S2 allowed, for the first time, for a direct measurement of the distance to the GC.

The NIR imaging data acquired with the new NIR camera and adaptive optics system CONICA/NAOS at the ESO 8 m-class VLT on Paranal, Chile allowed additional fundamental observations due to its high sensitivity, large field-of-view, and its exceptional ability to exploit the resolution of an 8m-class telescope: We could show that the density distribution of the stars is centred on the black hole, where it displays a density excess, the theoretically predicted 'cusp'. The stellar population in this cusp has distinctive features that distinguish it from the overall large scale cluster. Finally, the new instrumentation made it possible, for the first time, to detect NIR quiescent and flaring emission from Sgr A*. This provides crucial constraints on the emission mechanisms. Most importantly, the intrinsic quasi-periodicity of the flares appears to allow setting a lower limit on the spin of the black hole, a fundamental parameter of such objects that was so far not accessible to direct observations.

We summarise the main results of this thesis in detail in the paragraphs below.

Astrometry   The large FOV and the superb optical characteristics of the combined NIR camera and adaptive optics system NACO at the ESO 8 m VLT enabled us to establish an accurate astrometric reference system for NIR observations of the nuclear star cluster (Chapter 5). For this purpose, we used the positions and proper motions of seven SiO maser stars, which had been measured to a high accuracy with radio interferometric observations (Reid et al., 2003). Through matching the radio and the NIR positions of these stars and estimating the various uncertainties involved in this procedure, we could reach an accuracy of < 10 milli-arc-seconds for the position of Sgr A* on NIR images of the nuclear stellar cluster. Also, we estimated an accuracy of the order 10 mas for the astrometric positions of stars within $10''$ of

Sgr A*. Establishing an exact astrometric reference frame is the indispensable fundament for identifying a possible near-infrared counterpart of Sgr A*, for analysing the proper motions and orbits of the stars in the central gravitational potential, and for detecting possible lensed images of background stars by the black hole.

Central star cluster The adaptive optics (AO) system NAOS can lock the AO onto the bright (K∼ 6.5) supergiant IRS 7, just about $6''$ north of Sgr A*, thanks to its unique NIR wavefront sensor. This allowed obtaining images at the diffraction limit of the 8 m-class VLT with detector integration times from several seconds up to several minutes. Therefore with NACO/VLT it was possible to obtain images with 40-100 mas FWHM resolution (at H-, K-, and L-bands) that were two to three magnitudes deeper than any previous observations of the GC stellar cluster. With these new data, we could analyse the luminosity function and number density distribution of the stars in the central 0.5 pc around Sgr A*. For such an analysis it was important to be able to include the faint stellar component because the stellar luminosity in the central 0.5 pc is dominated completely by about two dozen bright stars. Therefore, the luminosity distribution does not accurately represent the overall structure of the cluster.

The number surface density of the stars keeps increasing to the very centre of the cluster. The radial profile of the overall cluster can be described well by a broken power-law with an exponent $\alpha = 2.0 \pm 0.1$ at distances $R \geq 10''$ and $\alpha = 1.4 \pm 0.1$ at $R < 10''$ from Sgr A*. The finding of a stellar density excess, a so-called *cusp*, agrees well with theoretical expectations of stellar systems around supermassive black holes. The density peak lies within $\leq 0.25''$ of Sgr A*, contrary to the peak of the luminosity distribution, which is offset by about $2''$ to the east due to about a dozen bright stars that dominate the luminosity of the cluster. At distances $\leq 0.1''$ from Sgr A* the star cluster reaches densities exceeding a few times 10^8 M$_\odot$ pc^{-3}.

The overall composition of the cluster can be described well by an old (~ 10 Gyr) stellar cluster of solar metalicity with an excess of bright stars that is evidence for an admixture of stars created in recent episodes of star formation. The existence of a cusp containing stars that are tightly bound to the central black hole and reaching extreme number densities raises the expectation that a peculiar stellar population might be present near Sgr A*. Indeed, when analysing the luminosity function of the cluster, we found that the cusp lacks horizontal branch/red clump stars. Since these stars should have masses lower than one solar mass, they might have been driven out of the cluster centre through mass segregation. Also, their envelopes might have been destroyed by stellar collisions in the dense cusp environment. There is also a distinct population of potential O/B-type stars present in the cusp, at distances < 40 mpc from Sgr A*. The origin of these stars cannot be explained conclusively by any current model. One of the currently discussed hypotheses is that these stars might be merger products that were created in the dense stellar cusp, similar to blue stragglers in globular clusters.

Proper motions A central aspect of this work was the determination of accurate proper motions in the prominent cluster of stars within a projected radius of about $1''$ (or 39 mpc) from Sgr A* (the so-called "Sgr A* cluster") . For this purpose, we re-analysed SHARP/NTT NIR speckle imaging data from the period 1992 to 2001. Through a meticulous selection of the best speckle imaging frames from each epoch and a combination of various deconvolution methods, we created deep (K≤ 16) images of the nuclear cluster for every epoch. We combined these data with public GC science demonstration data from the Gemini North telescope and with NACO/VLT GC observations from 2002/2003 and determined the proper motions of 46 stars within $1.2''$ of Sgr A*. Independently, we determined proper motions for 55 stars within a projected distance of $1.2''$ from Sgr A*, using just NACO/VLT imaging data from five different epochs in 2002 to 2003.

With the measured projected stellar velocities, we estimated an enclosed dark mass of $3.4 \pm 0.4 \times 10^6$ M$_\odot$ (1992 to 2002 data set) and $4.0 \pm 0.8 \times 10^6$ M$_\odot$ (2002 to 2003 data set), respectively. This is higher than previously published statistical mass estimates. We believe

that the reason is that earlier works did not include a sufficient number of high velocity stars in the dense (and therefore highly confused) cusp, while our new proper motion analyses are more complete due to longer time lines, improved image analysis, and better instrumentation.

In both of our data sets we found evidence on the 2 to 3σ-level that the central cluster is radially anisotropic. This comes as a surprise because one would expect the dense nuclear cluster to be dynamically relaxed and therefore isotropic. Perhaps the anisotropy can provide an important clue to the formation of the cusp and the existence of potentially young, short-lived stars there.

Stellar orbits around Sgr A* In our proper motion sample, we identified six stars that showed significant acceleration during the covered time interval. We successfully fitted Keplerian orbits to their trajectories. All six stars (with possibly one exception) have semi-major axes < 20 mpc and are tightly bound to the central dark mass, as it is expected in a steep stellar cusp. The distribution of the eccentricities of the orbits agrees with an isotropic cluster. We found no clear sign of radial anisotropy. However, the number of stars with determined orbits is still too small for an accurate statistical analysis.

Five of the six stars with significant acceleration had passed through the peri-centre of their orbit during (or shortly before, in the case of S8) the observed period. Acceleration can be observed most easily near peri-centre, where it is largest. Since this can introduce a bias in the properties of the detected stellar orbits, we examined the probability of detecting stellar accelerations for orbits with different eccentricities in isotropic clusters with density distributions according to a power-law of the form $n \propto r^{-\alpha}$. The bias is negligible in clusters with $\alpha = -2.0$, but significant for $\alpha = -1.0$, where highly eccentric orbits will be preferentially detected. In the case of $\alpha = -1.5$, which is close to the slope of the GC cusp, we found that there is a bias to detect orbits with eccentricities > 0.9. However, the bias factor is remains smaller than two. As for the six orbits analysed in chapter 8, they should not be biased toward high eccentricities because of their small semi-major axes.

The star S2 has the best determined orbit that allows – when spectroscopic measurements of the line-of-sight velocity of S2 are included – to determine simultaneously the mass, location, and distance of the central dark object. The focus of the orbit is located within a few milli-arcseconds of the nominal radio position of Sgr A*, adding considerable weight to the assumption that Sgr A* is the manifestation of a supermassive black hole. The distance to Sgr A* as determined from the orbit of S2 is 7.9 ± 0.4 kpc. This is the first direct determination of the distance to the GC. Through the calibration of bright or variable stars, the distance to the GC is an important rung in the cosmic distance ladder. With our measurement we could confirm the canonic value of 8.0 ± 0.5 kpc and thus the correctness of this fundamental distance.

With a period of 15.56 years and a semi-major axis of 4.63 mpc, the enclosed mass within the orbit of S2, as calculated from Kepler's 3rd law, must be $3.6 \pm 0.3(0.6) \times 10^6 \, \mathrm{M_\odot}$ (the error estimate in brackets includes the uncertainty in the distance). This mass agrees very well with the mass inferred from the proper motion data. However, the orbit of S2 provides the additional constraint that this mass must be enclosed within the peri-centre distance of 0.55 ± 0.03 mpc.

The nature of Sgr A* The question that is certainly of highest interest when studying the GC, is the nature of the non-thermal radio, X-ray, and infrared source Sgr A* and whether it is indeed the manifestation of a supermassive black hole. While earlier observations of gas and stellar dynamics in the central parsec of the Milky Way, as well as radio interferometric and X-ray observations of Sgr A* had already accumulated considerable evidence that it was probably such an object, the determination of stellar orbits within the framework of this thesis could provide a fundamental step forward because it constrained the dark mass to a volume with a radius of about $2/3$ of a light day.

A dense cluster of dark astrophysical objects as explanation for the concentration of dark mass can be excluded because it would have a life time of less than 10^5 years. Hence it would

be highly unlikely to observe such a configuration at the present time.

As for a ball of massive, degenerate fermions, such as neutrinos, our observations require a neutrino mass between 48 and 417 keV if such an object should explain the gravitational potential in the nuclear cluster. The high minimum neutrino mass excludes that all dark matter concentrations seen at the centres of galaxies can be explained by a single neutrino ball model because the heaviest such objects (e.g. at the centre of M87) would exceed the Oppenheimer-Volkoff limit. An additional difficulty for the neutrino ball model is that such an object should eventually collapse to a black hole because of baryonic accretion. The same dilemma concerns the highly speculative boson star model.

A supermassive black hole, on the other hand, would be a stable configuration and fits all the observations. The case for the black hole becomes even stronger if we assume that the size of the radio source Sgr A*, as measured by interferometry, sets a limit on the intrinsic size of this object. In that case, the upper and lower limits for the mass of the neutrino in a hypothetical neutrino ball would be 311 and 417 keV, i.e. very close to each other. The lower mass limits determined from the upper limits on the proper motion of the radio source Sgr A* in combination with the velocities of a few times 10^3 kms^{-1} of the surrounding stars, require this object to have a minimum mass of several thousand solar masses. We conclude that the GC now represents the strongest known case for the existence of supermassive black holes.

NIR flares from Sgr A* and a possible spin measurement of the black hole   The search for a NIR counterpart of Sgr A* during the past decade did not provide any conclusive results. When observing the GC with NACO at the VLT in spring of 2003, however, we discovered a powerful (factor of six above quiescent level) NIR flare from Sgr A*. Through subsequent observations and analysis of earlier NACO/VLT data we identified variability of Sgr A* at NIR wavelengths from 1.7 to 3.8μm. The position of the flares within less than 10 mas of Sgr A* and their observation at this position at five different epochs are strong evidence for an association of these flares with Sgr A*. The rise-and-fall time scales of a few minutes suggest that the emission was produced within less than 10 Schwarzschild radii of a 3.6×10^6 M$_\odot$ black hole. Apart from the flares, we could also identify a quiescent source at the position of Sgr A* in 2003 NACO/VLT imaging data. Both the quiescent and the flaring state of Sgr A* showed intrinsic time variability.

The NIR regime is critical for constraining models of accretion onto and emission from Sgr A*. While the quiescent photometric data are in fairly good agreement with current models, the photometry of the flares suggests that these events might have a blue colour. However, this possibility has to be checked by future multi-wavelength observations. In that case the flares could represent individual accretion events.

The most striking feature of the flares was their intrinsic variability. In two independent events we found a quasi-periodicity of about 17 min. This short time scale can be explained best by Doppler boosting of the emission of matter near the last stable orbit of a spinning (Kerr) black hole. Should future observations confirm this periodicity of the flares, then this signifies the first measurement of the spin of a black hole, making fundamental physical properties of these objects for the first time accessible to direct observation.

Appendix A

A.1 The Spherically Symmetric Power-Law Cusp

For convenience, we present here a self contained summary of some properties of the distribution function (DF) of a spherically symmetric system, and apply them to a power-law cusp and Keplerian orbits.

A.1.1 Isotropic Velocity Field

The DF $f(\varepsilon)$ of a system with an isotropic velocity field is a function of the specific energy only, $\varepsilon \equiv -v^2/2 + \psi(r)$, where $\psi \equiv -\phi$ and ϕ is the gravitational potential (f has units of $x^{-3}v^{-3}$; $f(\varepsilon) = 0$ for $\varepsilon \leq 0$). The space density distribution, $n(r) \equiv \int f(\varepsilon)\mathrm{d}^3v$ (in units of x^{-3}), is

$$n(r) = 4\pi \int_0^{\sqrt{2\psi(r)}} f(\varepsilon)v^2\mathrm{d}v = 4\pi \int_0^{\psi(\mathrm{r})} f(\varepsilon)\sqrt{2(\psi - \varepsilon)}d\varepsilon \,, \tag{A.1}$$

where the last step is made with the variable transformation $\mathrm{d}\varepsilon = -v\mathrm{d}v$, and $v = \sqrt{2(\psi - \varepsilon)}$.

For a power-law DF, $f(\varepsilon) = A\varepsilon^p$,

$$n(r) = (2\pi)^{3/2}\frac{\Gamma(1+p)}{\Gamma(5/2+p)}A\psi(r)^{3/2+p}\,. \tag{A.2}$$

Very near the black hole the orbits are Keplerian to a good approximation, $\psi = Gm/r$, and therefore $n(r) \propto r^{-3/2-p}$.

The distribution of specific energy is $n(\varepsilon) \equiv \int f(\varepsilon')\delta(\varepsilon' - \varepsilon)\mathrm{d}^3x\mathrm{d}^3v$ (in units of v^{-2}), where δ is the Dirac delta function (in units of the inverse of its argument). Using the property $\delta(h(x)) = \delta(x - x_0)/|\mathrm{d}h/\mathrm{d}x|$, where $h(x_0) = 0$, and performing first the integration over velocities, one obtains for Keplerian orbits ($a = Gm/2\varepsilon$)

$$\begin{aligned}
n(\varepsilon) &= (4\pi)^2 f(\varepsilon)\sqrt{Gm}\int_0^{2a}\sqrt{2/r - 1/a}r^2\mathrm{d}r \\
&= \sqrt{2}\pi^3(Gm)^3 f(\varepsilon)\varepsilon^{-5/2} \\
&= 2^{3-p}\pi^3(Gm)^{1/2+p}Aa^{5/2-p}\,. \tag{A.3}
\end{aligned}$$

The distribution of semi-major axes, $n(a)$ (in units of x^{-1}) is therefore

$$n(a) = |d\varepsilon/da|\, n(\varepsilon) = 2^{2-p}\pi^3(Gm)^{3/2+p}Aa^{1/2-p}\,. \tag{A.4}$$

The distribution of eccentricities in a spherically symmetric distribution of Keplerian orbits with an isotropic velocity field is derived below (Eq. A.8).

A.1.2 Anisotropic Velocity Field

In the general spherically symmetric case, the DF $f(\varepsilon, L)$ depends on both the specific energy $\varepsilon = -v_r^2/2 - L^2/2r^2 + \Psi$ and the magnitude of the specific angular momentum, $L^2 = (rv_t)^2$, where v_r and v_t are the radial and transverse components of the velocity relative to the radius vector.

In cylindrical coordinates $\mathrm{d}^3 v = 2\pi v_t\, \mathrm{d}v_t\, \mathrm{d}v_r$, and so substituting $v_t\, \mathrm{d}v_t = L\mathrm{d}L/r^2$, $\mathrm{d}v_r = -\mathrm{d}\varepsilon/v_r$ with an extra factor of 2 to account for both contributions from $\pm v_r$ to $\mathrm{d}\varepsilon$, one obtains

$$\mathrm{d}^3 v = 4\pi L\, \mathrm{d}L\, \mathrm{d}\varepsilon\,/r^2\, |v_r(\varepsilon, L, r)|\ . \tag{A.5}$$

The distribution of specific energy and angular momentum, $n(\varepsilon, L)$ (in units of $x^{-1}v^{-3}$) is obtained by integrating $f(\varepsilon, L)\, 4\pi r^2 \mathrm{d}r\, \mathrm{d}^3 v/\mathrm{d}\varepsilon \mathrm{d}L$ over the range (r_-, r_+) that is accessible with ε and L,

$$
\begin{aligned}
n(\varepsilon, L) &= 16\pi^2 L f(\varepsilon, L) \int_{r_-}^{r_+} \frac{\mathrm{d}r}{|v_r(\varepsilon, L, r)|} \\
&= 8\pi^2 L f(\varepsilon, L) T_r(\varepsilon, L) ,
\end{aligned}
\tag{A.6}
$$

where T_r is the radial period and the integral expresses the contribution from each $\mathrm{d}r$ segment of the orbit, weighted by the time spent there.

For Keplerian orbits $\varepsilon = GM/2a$, $L^2 = GMa(1 - e^2)$ and $T_r = P(\varepsilon) = \pi GM/\sqrt{2\varepsilon^3}$, and so $2L\, \mathrm{d}L = -(GM)^2/(2\varepsilon)e\, \mathrm{d}e$. It then follows from Eq. (A.6) that the distribution of specific energy and eccentricity (in units of v^{-2}) is (cf Cohn & Kulsrud 1978)

$$n(\varepsilon, e) = \left[2\sqrt{2}\pi^3 (GM)^3 f(\varepsilon, L)\varepsilon^{-5/2} \right] e , \tag{A.7}$$

It then follows that for Keplerian orbits with *isotropic* velocities the distribution of eccentricities $n(e)$ (dimensionless) is (see Binney & Tremaine 1987, p. 282, problem 4-22)

$$n(e) = \left[2\sqrt{2}\pi^3 (GM)^3 \int f(\varepsilon)\varepsilon^{-5/2}\, \mathrm{d}\varepsilon \right] e \propto e . \tag{A.8}$$

Appendix B

B.1 Colour Figures
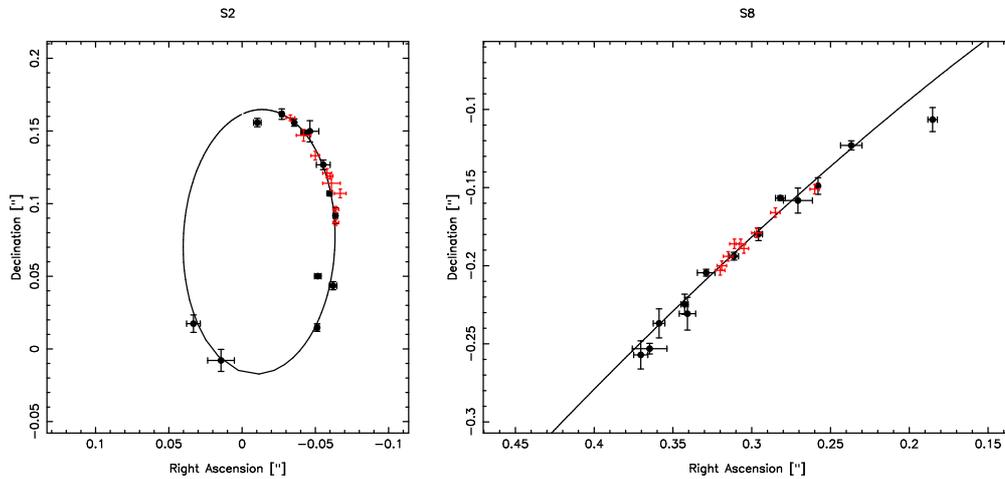
Figure B.1: **Comparison between SHARP/NTT and Keck positions**. *A comparison between positions of the stars S2 and S8 as measured in this work and by Ghez et al. (2000). SHARP/NTT positions are marked by filled black circles with error bars, Keck positions just by their error bars (in red). An offset of 40 mas W and 9 mas N (derived form the difference in position of S2 for the 1995 epoch) was applied to the Keck data in order to take into account the astrometric offset between the data sets. Straight lines mark the orbits fitted to the position of S2 and S8 (see chapter 8).*

Appendix
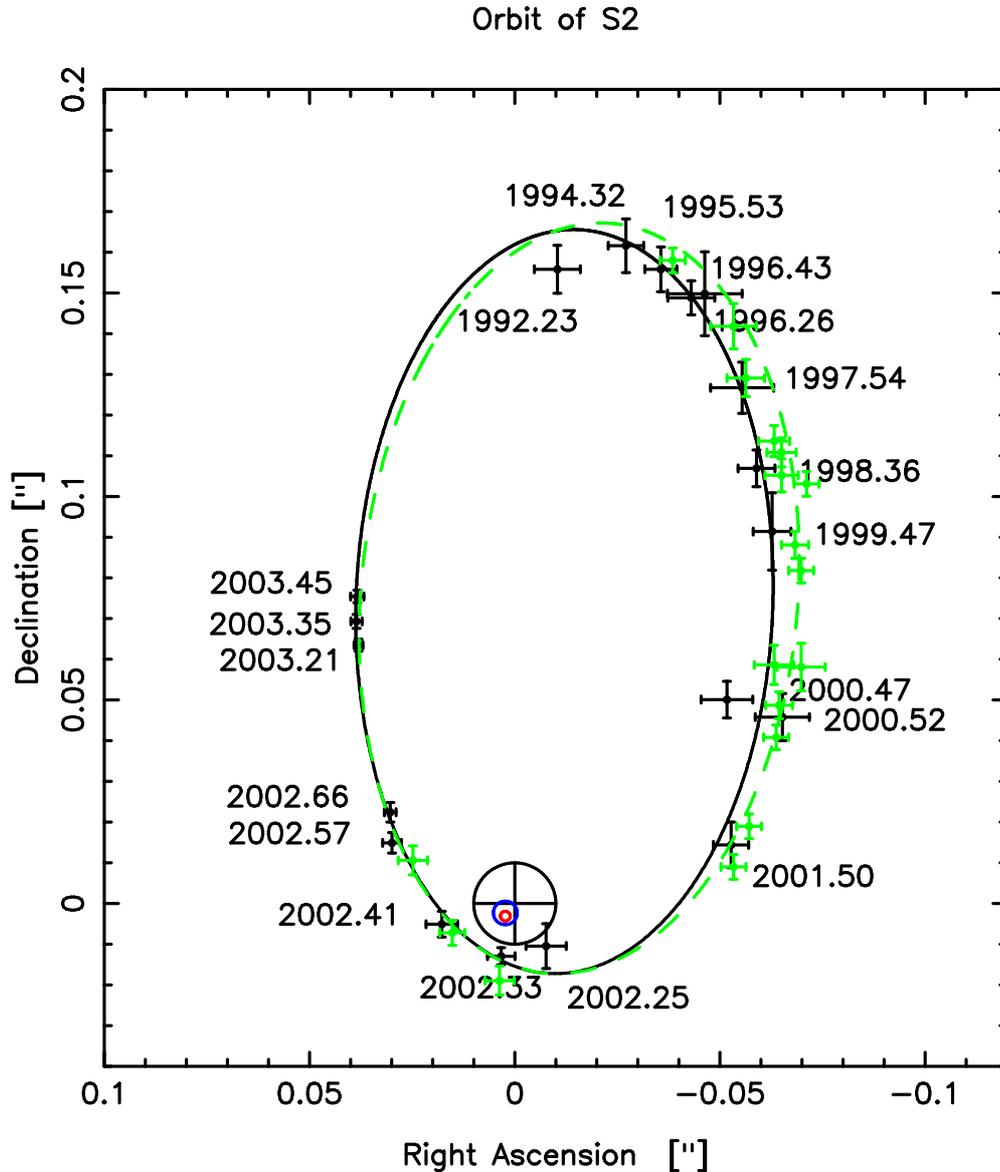
Figure B.2: **Comparison of the Orbit of the Star S2 around Sgr A* as Measured by two Independent Groups.** *Black: Best-fit orbit and measured time-dependent positions of the star S2 as determined in this work. The positions are marked by the crosses of their errors bars. All positions are given relative to the radio position of Sgr A*, which is marked by a cross and a 10 mas error circle. The small red circle inside the radio error circle is the 1σ error circle of the focus of the orbit as determined by the Keplerian fit. Green: Orbit of S2 as determined by Ghez et al. (astro-ph/0306130). The blue circle around the red circle is the corresponding focus of the orbit, with its uncertainty of 1.5 mas combined with the uncertainty of aligning the two orbits . The orbits were aligned by taking the difference between the S2 positions for 2002.3 as they result from the orbital parameters of this work and of Ghez et al. (astro-ph/0306130). The uncertainties were added quadratically. The measured positions by Ghez et al. (green crosses) were taken from Ghez et al. (2003) and shifted by the offset of the orbital focus given in that paper to the focus of the orbit determined in this work. We did not include the 2003 position of astro-ph/0306130 because it could not be extracted with sufficient accuracy. from the corresponding plot.*
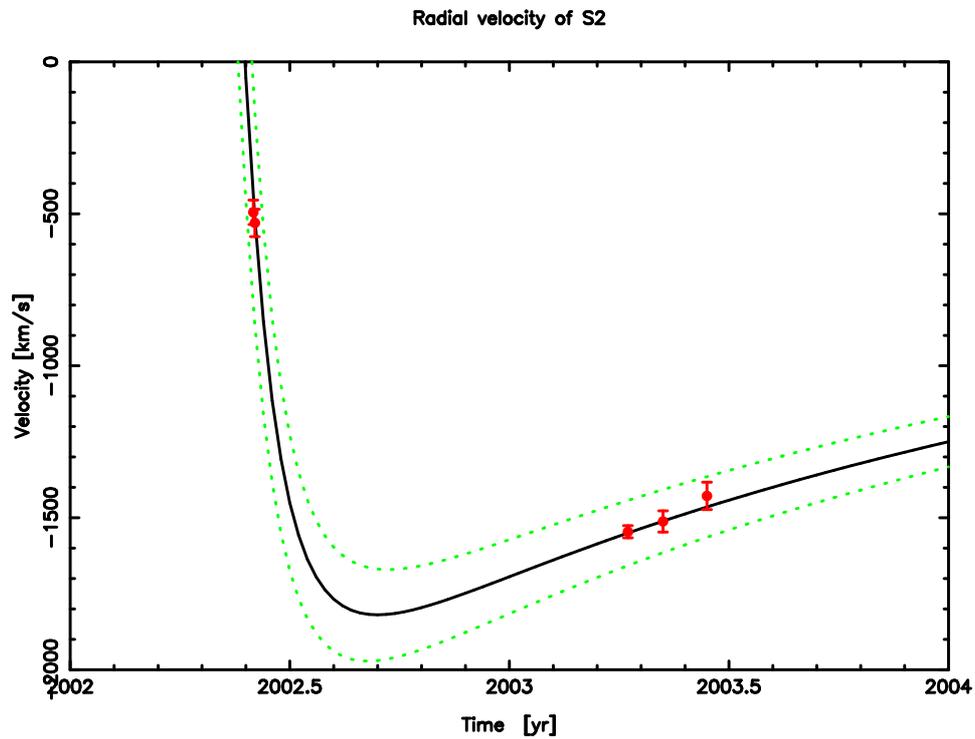
Figure B.3: **Line of sight velocity of S2 along its orbit.** *Black line: Time-dependent line-of-sight velocity of S2, calculated from the best-fit orbit. Dotted green lines: Uncertainty of calculated line-of-sight velocity. Measured line of sight velocities are indicated by red filled circles and their error bars. Measurements in 2002 taken from Ghez et al. (2003), from 2003 from Eisenhauer et al. (2003). For a description of the various measurements of the line-of-sight velocity, see Eisenhauer et al. (2003).*
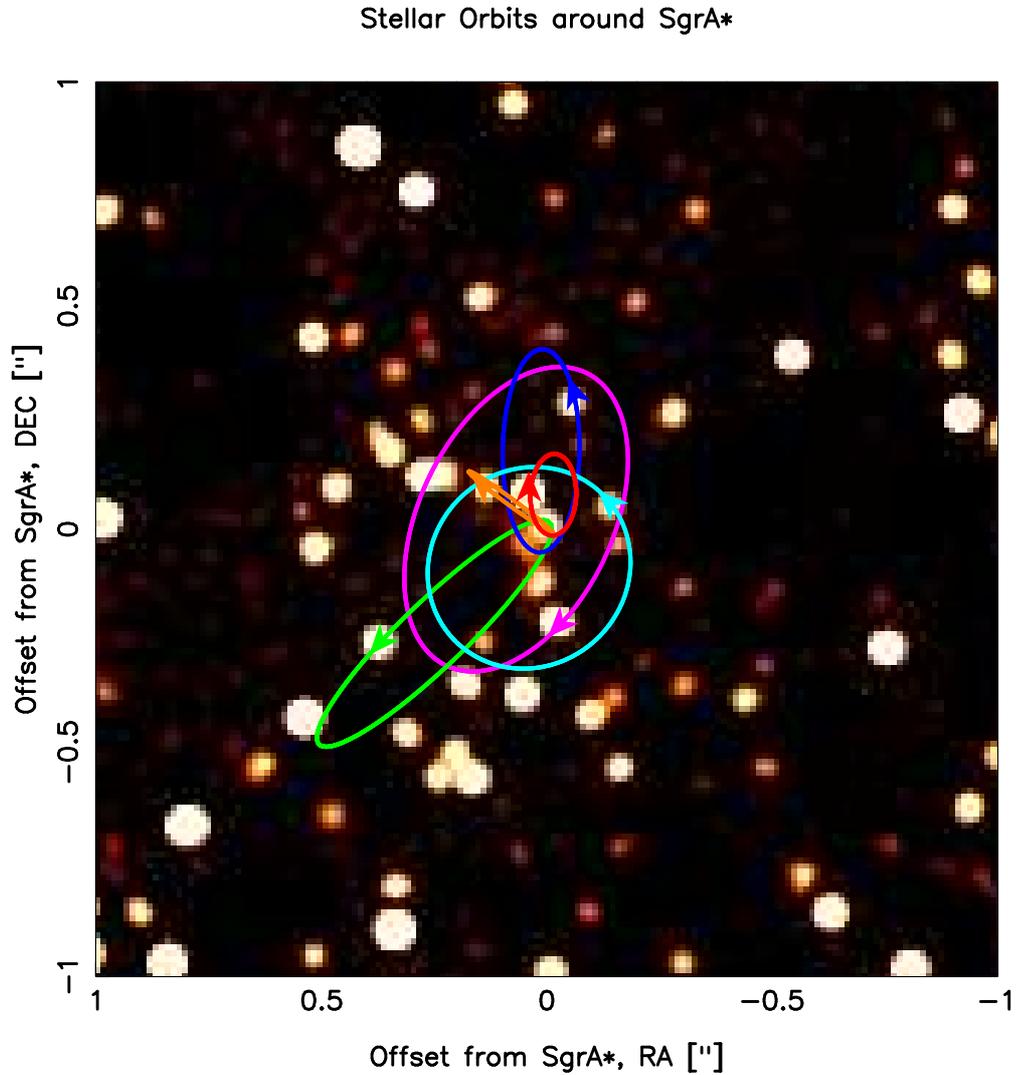
Figure B.4: **Orbits of stars around Sgr A*.** *Lucy-Richardson deconvolved and beam-restored high-resolution (FWHM∼ 60 milliarcseconds) near-infrared (2.2μm) image of the central $1'' \times 1''$ of the nuclear stellar cluster. The image was obtained with CONICA/NAOS at the ESO VLT in June 2003. On this image Sgr A* can be seen in its flaring state as a point source at the origin of the coordinate system. The Keplerian orbits of six stars, as they were determined by a decade of continued observations, are over-plotted onto the image. Arrows indicate the locations of the respective stars and their direction of motion.*
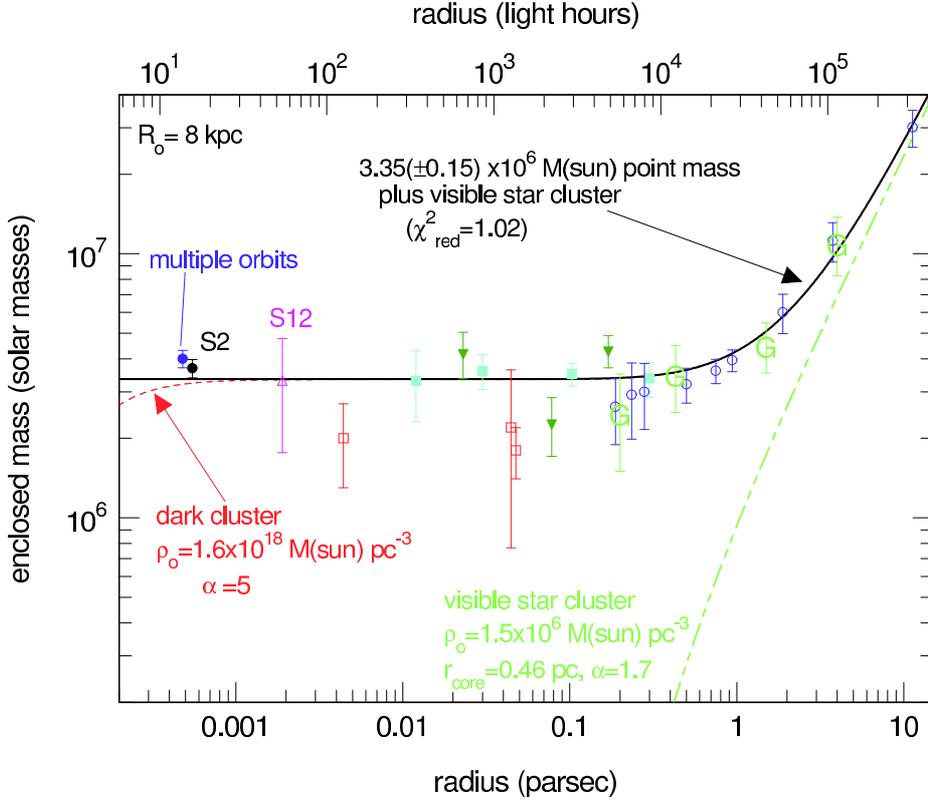
Figure B.5: **Mass distribution in the galactic centre.** *Enclosed mass vs. distance from Sgr A* in the GC, assuming a distance of 8 kpc (Reid, 1993). The circles at the shortest projected distances denote the masses derived from a fit of multiple orbits by Ghez et al. (2003, astro-ph/0306130) and from the orbits of S2 and S12 (this work). Filled down pointing triangles denote Leonard-Merritt projected mass estimators from the present work (at 0.025 pc) and from a new NTT proper motion data set by Ott (2003), separating late and early type stars, and correcting for the volume bias determined from Monte Carlo modelling of theoretical clusters and assuming a central density profile with a power-law slope of $\alpha = 1.4$ (Genzel et al., 2003). An open down-pointing triangle denotes the Bahcall-Tremaine mass estimate obtained from Keck proper motions (Ghez et al. 1998; we multiplied their error bar by a factor of 2 in order to take possible systematic errors into account). Filled rectangles are mass estimates from a parameterised Jeans-equation model, including effects of anisotropy and differentiating between late and early type stars (Genzel et al., 2000). Open circles are mass estimates from a parameterised Jeans-equation model of the radial velocities of late type stars, assuming isotropy (Genzel et al., 1996). Open rectangles denote mass estimates from a non-parametric, maximum likelihood model, assuming isotropy and combining late and early type stars (Chakrabarty & Saha, 2001). Letter "G" points denote mass estimates obtained from Doppler motions of gas (Genzel & Townes, 1987). The straight continuous curve is the overall best fit model to all data. It is the sum of a $3.35 \pm 0.15 \times 10^6 M_\odot$ point mass, plus a stellar cluster of central density $1.5 \times 10^6 M_\odot pc^{-3}$, core radius 0.46 pc and power-law index $\alpha = 1.7$. The grey long dash-short dash curve shows the same stellar cluster separately, but for an infinitely small core. The dashed curve is the sum of the visible cluster, plus a Plummer model of a hypothetical very compact dark cluster of central density $1.9 \times 10^{18} M_\odot pc^{-3}$.*

Figure B.6: **Light curves of Sgr A* NIR flares.** *Light curves of the Sgr A* NIR flares in 2002 and 2003, observed with NACO/VLT (blue). The L-band flare on August 30, 2002, was only partially covered by observations. Gaps in the time series of the H-band flare on May 10, 2003, and of the K-band flare on June 15, 2003, are due to sky observations and instrument failure, respectively. For comparison, the steady emission of the star S1 near Sgr A* is shown in all the plots (red data points). Arrows in the plots of the two K-band flares indicate substructure peaks of the flares. Both K-band flares show very similar quasi-periodicity, although the second flare was observed more than 24 h after the first one and must thus have been an unrelated event. The upper right panel shows the normalised power spectrum of the two K-band flares. Both of them show a significant peak at a frequency corresponding to time scales of* 16.8 ± 2.0 *min. In both cases, the power spectrum of S1 does not show such a frequency. This Figure corresponds to Figure 2 in Genzel et al. (2003a).*
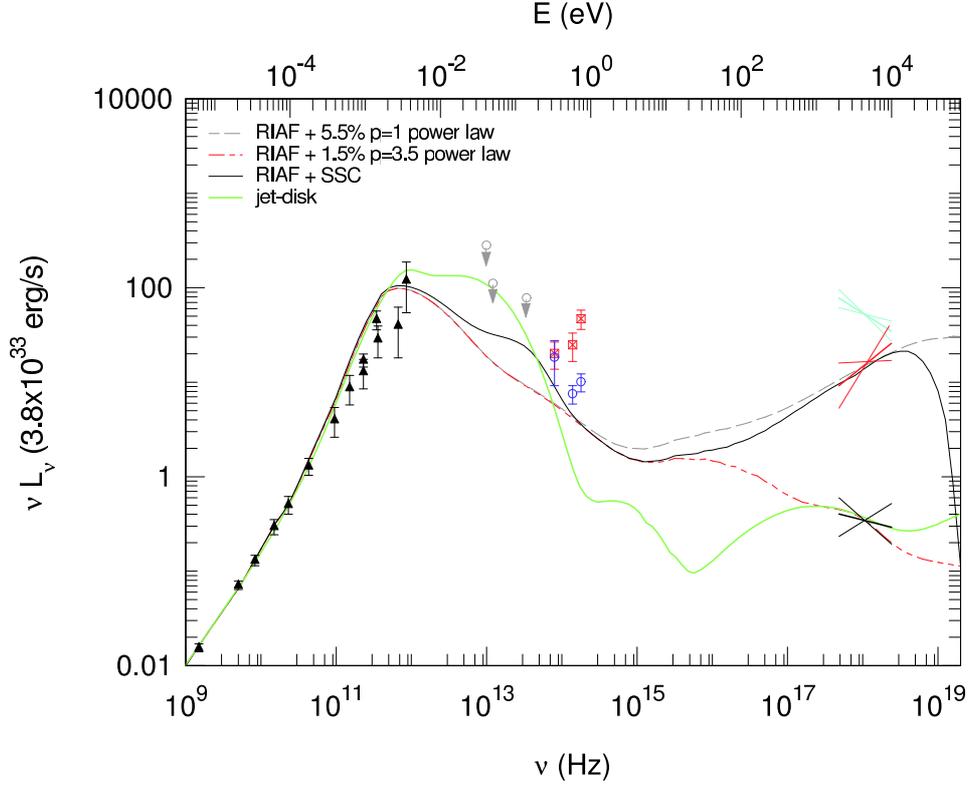
Figure B.7: **Spectral energy distribution of the emission from Sgr A*.** *This plot shows the extinction and absorption corrected luminosities νL_ν (energy emitted per logarithmic energy interval), with the observed flux density $S_\nu = L_\nu/4\pi D^2$, where $D = 7.94$ pc is the GC distance. All error bars are $\pm 1\sigma$ and include statistical and systematic errors. Black triangles denote the radio spectrum of Sgr A* (Markoff et al., 2001; Zhao et al., 2003). Open grey circles mark various infrared upper limits from literature (Markoff et al., 2001). The three X-ray data ranges are (from bottom to top) the quiescent state as determined with Chandra (black; Baganoff et al., 2003), the autumn 2000 Chandra flare (red; Baganoff et al., 2001), and the autumn 2002 flare observed by XMM (light blue; Porquet et al., 2003). Open red squares with crosses mark the de-reddened peak emission (minus quiescent emission) of the four NIR flares, listed in Table 10.1. Open blue circles mark the de-reddened H, K, and L luminosities of the quiescent state, derived from the local background subtracted flux density of the point source at the position at Sgr A*,thus eliminating the contribution from extended, diffuse light due to the stellar cusp around Sgr A*. The thick green solid curve is the jet-starved disk model by Yuan et al. (2002). The red long dash-short dash curve is a radiative inefficient accretion flow (RIAF) model of the quiescent emission, where in addition to the thermal electron population of Yuan et al. (2002) 1.5% of the electrons have a non-thermal power-law energy spectrum of exponent $p = -3.5$ (Yuan, Quataert, & Narayan, 2003, astro-ph/0304125). The black thin solid curve is a RIAF model of the flares with 5.5% of the electrons in a power-law of $p = -1$ (Yuan, Quataert, & Narayan, 2003, astro-ph/0304125). The long-dash thick curve is a RIAF flare model of the flares with a synchrotron-self Compton component (Yuan, Quataert, & Narayan, 2003, astro-ph/0304125). This Figure corresponds to Figure 3 in Genzel et al. (2003a).*

Bibliography

Aitken, D.K., Greaves, J., Chrysostomou, A., Jenness, T., Holland, W., Hough, J.H., Pierce-Price, D., & Richer, J. 2000, Ap.J., 534, L173

Alexander, T. 2002, in The Galactic Black Hole, eds. H. Falcke & F. W. Hehl, (Institute of Physics), ch. 9

Alexander, T. 2001, Ap.J., 553, L149

Alexander, T. 1999, Ap.J., 527, 835

Alexander, T., & Sternberg, A., 1999, Ap.J., 520, 137

Allen D.A., & Sanders, R.H. 1986, Nature, 319, 191

Allen, D.A., Hyland, A.R., & Hillier, D.J. 1990, MNRAS, 244, 706

Backer, D.C., & Sramek, R.A. 1999, Ap.J., 524, 805

Baganoff, F.K., Bautz, M.W., Brandt, W.N., Chartas, G., Feigelson, E.D., Garmire, G.P., Maeda, Y., Morris, M., Ricker, G.R., Townsley, L.K., & Walter, F. 2001, Nature, 413, 349

Baganoff, F. K., Maeda, Y., Morris, M., Bautz, M. W., Brandt, W. N., Cui, W., Doty, J. P., Feigelson, E. D., Garmire, G. P., Pravdo, S. H., Ricker, G. R., & Townsley, L. K. 2003, Ap.J., 591, 891

Baganoff, F.K. 2003, HEAD 35

Bahcall, J.N., & Tremaine, S. 1981, Ap.J., 244, 805

Bahcall, J.N., & Wolf, R.A. 1976, Ap.J., 209, 214

Bahcall, J.N., & Wolf, R.A. 1977, Ap.J., 216, 883

Balick, B., & Brown, R.L. 1974, Ap.J., 194, 265

Bardeen, J.M., Press, W.M., & Teukolsky, S.A. 1972, Ap.J., 178, 347

Bardeen, J.M., & Pettersen, J.A. 1975, 105, L65

Becklin, E.E., & Neugebauer, G. 1968, Ap.J., 151, 145

Bilić, N., Tupper, G.B., & Viollier, R.D. 2003, astro-ph/0310172

Binney, J., & Tremaine, S. 1987, Galactic Dynamics (Princeton: Princeton Univ. Press)

Blum, R.D., Sellgren, K., & DePoy, D.L. 1996, Ap.J., 470, 864

Blum, R.D., Sellgren, K. & DePoy, D.L. 1996, AJ, 112, 1988

Bower, G.C., Wright, M.C.H., Falcke, H., Backer, D.C. 2003, Ap.J., 588, 331

Brown, R.L. 1982, Ap.J., 262, 110

Catchpole, R.M., Whitelock, P.A., Glass, I.S. 1990, MNRAS, 247, 479

Chakrabarty, D., & Saha, P. 2001, AJ, 122, 232

Chatterjee, P., Hernquist, L., & Loeb, A. 2002, Ap.J., 572, 381

Davidge, T.J., Simons, D.A., Rigaut, F., Doyon, R. & Crampton, D. 1997, AJ, 114, 2586

De Villiers, J.-P., Hawley, J.F., & Krolik, J.H. 2003, submitted to Ap.J., astro-ph/0307260.

Doeleman, S. S., Shen, Z.-Q., Rogers, A. E. E., Bower, G. C., Wright, M. C. H., Zhao, J. H.,
    Backer, D. C., Crowley, J. W., Freund, R. W., Ho, P. T. P., Lo, K. Y., & Woody, D. P. 2001,
    Astron.J., 121, 2610

Dorband, E. N., Hemsendorf, M., & Merritt, D. 2003, J. Computational Phys., 185, 484

Diolaiti, E., Bedinelli, O., Bonaccini, D. Close, L., Currie, D., and Parmeggiani, G. 2000, A&
    A Supplement Series, vol. 147 (no. 2), Editions de Physique, p335

Eckart, A., Genzel, R., Krabbe, A., Hofmann, R., van der Werf, P.P., & Drapatz, S. 1992,
    Nature, 335, 526

Eckart, A., Genzel, R., Hofmann, R., Sams, B.J., Tacconi-Garman, L.E., & Cruzalebes, P.
    1994, in Genzel, R., Harris, A.I., eds., NATO ASI series, The Nuclei of Normal Galaxies,
    Kluwer, Dordrecht, p.305

Eckart, A., Genzel, R., Hofmann, R., Sams, B.J., & Tacconi-Gaarman, L.E. 1995, Ap.J., 445,
    L23

Eckart, A., & Genzel, R. 1996, Nature, 383, 415

Eckart, A., & Genzel, R. 1997, MNRAS, 284, 576

Eckart, A., Ott, T.,**?**& Genzel, R. 1999, A&A, 352, L22

Eckart, A., Genzel, R., Ott, T., & Sch¨odel, R. 2002, MNRAS, 331, 917

Eisenhauer, F., Sch¨odel, R., Genzel, R., Ott, T., Tecza, M., Abuter, R., Eckart, A., & Alexander,
    A. 2003, Ap.J., 597, L121

Figer, D.F., Becklin, E.E., McLean, I.S., Gilbert, A.M., Graham, J.R., Larkin, J.E., Levenson,
    N.A., Teplitz, H.I., Wilcox, M.K., & Morris, M. 2000, Ap.J., 533, L49

Figer, D.F. 2003, in Proc.IAU 212, San Francisco: Astronomical Society of the Pacific, p.487

Gebhardt, K., Richstone, D., Tremaine, S., Lauer, T. R., Bender, R., et al. 2003, Ap.J., 583, 92

Genzel, R., & Townes, C.H. 1987, Ann.Rev.Astron.Astrophys., 25, 377

Genzel, R., Hollenbach, D., & Townes, C.H. 1994, Rep. Prog. Phys., 57, 417

Genzel, R., Thatte, N., Krabbe, A., Kroker, H., & Tacconi-Garman, L. E. 1996, Ap.J., 472,
    153

Genzel, R., Eckart, A., Ott, T., & Eisenhauer, F., 1997, MNRAS, 291, 219

Genzel, R., Pichon, C., Eckart, A., Gerhard, O. E., & Ott, T. 2000, MNRAS, 317, 348

Genzel, R. 2001, in Dynamics of Star Clusters and the Milky Way, ASP Conf. Ser. 228, eds. S. Deiters, B. Fuchs, R. Spurzem, A. Just, & R. Wielen, Astr. Soc. of the Pacific: San Francisco, 291

Genzel, R., Sch ̈odel, R., Ott, T., Eisenhauer, F., Hofmann, R., Lehnert, M., Eckart, A., Alexander, T., Sternberg, A., Lenzen, R., Clénet, Y., Lacombe, F., Rouan, D., Renzini, A., & Tacconi-Garman, L. E. 2003, Ap.J., 594, 812

Genzel, R., Sch ̈odel, R., Ott, T., Eckart, A., Alexander, T., Lacombe, F., Rouan, D., & Aschenbach, B. 2003a, Nature, 425, 934

Gerhard, O. 2001, Ap.J., 546, L39

Gezari, S., Ghez, A.M., Becklin, E.E., Larkin, J., McLean, I.S., & Morris, M. 2002, Ap.J., 576, 790

Ghez, A., Klein, B. L., Morris, M., & Becklin, E. E. 1998, Ap.J., 509, 678

Ghez, A.M., Morris, M., Becklin, E. E., Tanner, A., & Kremenek, T. 2000, Nature, 407, 349

Ghez, A., Duchêne, G., Matthews, K., Hornstein, S.D., Tanner, A., Larkin, J., Morris, M., Becklin, E. E., Salim, S., Kremenek, K., Thompson, D., Soifer, B.T., Neugebauer, G., & McLean, I. 2003, Ap.J., 586, L127.

Ghez, A.M., Salim, S., Hornstein, A., Tanner, A., Morris, M., Becklin, E.E., & Duchêne, G. 2003a, astro-ph/0306130

Gwinn, C.R., Danen, R.M., Middleditch, J., Ozernoy, L.M., & Tran, T.K. 1991, Ap.J., 381, L43

Haller, J.W., Rieke, M.J., Tamblyn, P., Close, L., & Melia, F. 1996, Ap.J., 456, 194

Hofmann, R., Brandl, B., Eckart, A., Eisenhauer, F., Tacconi-Garman, L. E., in Proc. SPIE 1995, 2475, 192

Hornstein, S. D., Ghez, A. M., Tanner, A., Morris, M., Becklin, E. E., Wizinowich, P. 2002, Ap.J., 577, L9

Jeffries, S. M., & Christou, J. C. 1993, Ap.J., 415, 862

Kim, S., & Morris, M. 2003, Ap.J., 597, 312

Kormendy, J. 2001, RevMexAA, 10, 69

Kormendy, J. 2003, astro-ph/0306353

Krabbe, A., Genzel, R., Eckart, A., Najarro, F., Lutz, D., Cameron, F., Kroker, H., Tacconi-Garman, L.E., Thatte, N., Weitzel, L., Drapatz, S., Geballe, T., Sternberg, A., & Kudritzki, R. 1995, 447, L95

Krichbaum, T. P., Graham, D. A., Witzel, A., Greve, A., Wink, J. E., Grewing, M., Colomer, F., de Vicente, P., Gomez-Gonzalez, J., Baudry, A., Zensus, J. A. 1998, Astron. Astrophys., 335, 106

Lebofsky, M.J. & Rieke, G.H. 1987, in The Galactic Center, AIP 155, ed. D.Backer, Amer.Inst.Phys: New York, 79

Lenzen, R., Hofmann, R., Bizenberger, P., & Tusche, A. 1998, in Proc. SPIE IR Astr. Instr. (ed. A.M. Fowler), 3354, 606

Leonard, P.J.T., & Merritt, D. 1989, Ap.J., 339, 195

Levin, Y., & Beloborodov, A.M. 2003, Ap.J., 590, L33

Liu, S. & Melia, F. 2001, Ap.J., 561, L77

Liu, S. & Melia, F. 2002, Ap.J., 566, L77

Lo, K.Y., Shen, Z.-Q., Zhao, J.-H., & Ho, P.T.P. 1998, Ap.J., 508, L61

Lucy, L.B. 1974, AJ, 19, 745

Lynden-Bell, D.,& Rees, M.J. 1971 MNRAS, 152, 61

Maoz, E. 1998, Ap.J., 494, L181

Markoff, S., Falcke, H., Yuan, F., Biermann, P.L. 2001, Astronomy and Astrophysics, 379, L13

Melia, F., & Coker, R. 1999, Ap.J., 511, 750

Melia, F., & Falcke, H. 2001, Ann.Rev.Astron.Astrophys., 39, 309

Menten, K.M., Reid, M., Eckart, A., & Genzel, R. 1997, Ap.J., 475, L111

Montenbruck, O., & Pfleger, T. 2002, Astronomy on the Personal Computer (Berlin: Springer Verlag)

Morris, M., & Serabyn, E. 1996, Annu. Rev. Astron. Astrophys. 1996, 34, 645

Mouawad, N., Eckart, A., Pfalzner, S., Straubmeier, C., Spurzem, R., Genzel, R., Ott, T., & Schödel, R., Astron. Nachr., Vol. 324, No. S1 (2003), Special Supplement "The central 300 parsecs of the Milky Way", Eds. A. Cotera, H. Falcke, T. R. Geballe, S. Markoff

Munyaneza, F. & Viollier R.D. 2002, Ap.J., 564, 274

Murphy, B.W., Cohn, H.N., & Durisen, R.H. 1991, Ap.J., 370, 60

Miyazaki, A., Tstsumi, T., & Tsuboi, M. 2003, Astron. Nachr., 324, 3

Najarro, F., Hillier, D.J., Kudritzki, R.P., Krabbe, A., Genzel, R., Lutz, D., Drapatz, S., Geballe, T.R. 1994, A&A, 285, 573

Najarro, F., Krabbe, A., Genzel, R., Lutz, D., Kudritzki, R.P., & Hillier, D.J. 1997, A&A, 325, 700

Nayakshin, S., Cuadra, J., & Sunyaev, R. 2003, A&A, in press, astro-ph/0304126

Nowak, M.A., Wagoner, R.V., Begelman, M.C., & Lehr, D.E. 1997, Ap.J., 477, L91

Ott, T., Eckart, A., & Genzel, R. 1999, Ap.J., 523, 248

Ott, T. 2003, Ph.D. Thesis, Ludwig-Maximilians-Universität, München

Porquet, D., Predehl, P., Aschenbach, B., Grosso, N., Goldwurm, A., Goldoni, P., Warwick, R. S., & Decourchelle, A. 2003, A&A, 407, L17

Portegies Zwart, S.F., McMillan, S.L.W., & Gerhard, O. 2003, Ap.J., 593, 352

Press, W.H., Flannery, B.P., Teukolsky, S.A., & Vetterling, W.T. 1993, Numerical Recipes in C: The Art of Scientific Computing (Cambridge: Cambridge University Press)

Raab, W. 2002, Ph.D. Thesis, Ludwig-Maximilians-Universität, München

Reid, M. 1993, AnnRevAA, 31, 345

Reid, M., Readhead, A.C.S., Vermeulen R.C., & Treuhaft, R.N. 1999, Ap.J., 524, 816

Reid, M. J., Menten, K. M., Genzel, R., Ott, T., Schödel, R., & Eckart, A. 2003, Ap.J., 587, 208

Reid, M. J., Menten, K. M., Genzel, R., Ott, T., Schödel, R., & Brunthaler, A. 2003a, Astron. Nachr., 324, No. S1, 3

Rieke, G.H., Rieke, M.J. & Paul, A.E. 1989, Ap.J., 336, 752

Rogers, Alan E. E., Doeleman, S., Wright, M.C.H., Bower, G.C., Backer, D.C., Padin, S., Philips, J.A., Emerson, D.T., Greenhill, L., Moran, J.M., Kellermann, K.I. 1994, Ap.J., 434, L59

Rousset G. 1998, in Proc. SPIE Adapt. Opt. Tech. (eds. D. Bonaccini & R.K. Tyson), 3353, 508

Rubilar, G.F., & Eckart, A. 2001, A&A, 374, 95

Salim, S., & Gould, A. 1999, Ap.J., 523, 633

Schödel, R., Ott, T., Genzel, R., Hofmann, R., Lehnert, M., Eckart, A., Mouawad, N., Alexander, T., Reid, M. J., Lenzen, R., Hartung, M., Lacombe, F., Rouan, D., Gendron, E., Rousset, G., Lagrange, A.-M., Brandner, W., Ageorges, N., Lidman, C., Moorwood, A. F. M., Spyromilio, J., Hubin, N., & Menten, K. M. 2002, Nature, 419, 694

Schödel, R., Ott, T., Genzel, R., Eckart, A., Mouawad, N., & Alexander, T. 2003, Ap.J., 596, 1015

Scoville, N.Z., Stolovy, S.R., Rieke, M., Christopher, M., **?**& Yusef-Zadeh, F. 2003, Ap.J., 594, 294

Sellgren, k., McGinn, M.T., Becklin, E.E., & Hall, D.N.B. 1990, Ap.J., 359, 112

Serabyn, E., & Lacy, J.H. 1985, Ap.J., 293, 445

Serabyn, E. 1988, Ap.J., 326, 171

Tanner, A., Ghez, A.M., Morris, M., Becklin, E.E., Cotera, A., Ressler, M., Wernr, M., & Wizinowich, P. 2002, Ap.J., 575, 860

Tiede, G. P., Frogel, J. A., & Terndrup, D. M., 1995, AJ, 110, 2788

Torres, D.F., Capozziello, S., Lambiase, G. 2000, Phys. Rev. D, 63, id.104012

Tsiklauri, D., & Viollier, R.D. 1998, Ap.J., 500, 591

Young, P. 1980, Ap.J., 242, 1232

Yuan, F., Markoff, S., & Falcke, H. 2002, A&A, 383, 854

Yuan, F., Quataert, E., & Narayan, R. 2003, 98, 301

Zhao, J.-H., Young, K. H., Herrnstein, R. M., Ho, P. T. P., Tsutsumi, T., Lo, K. Y., Goss, W. M., & Bower, G. C. 2003, Ap.J., 586, L29

Zoccali, M., Renzini, A., Ortolani, S., Greggio, L., Saviane, I., Cassisi, S., Rejkuba, M., Barbuy, B., Rich, R. M., & Bica, E. 2003, A&A, 399, 931

List of Figures

List of Tables

127

Table of Abbreviations

AO	Adaptive Optics
DF	Distribution Function
ESO	European Southern Observatories
FOV	Field-of-View
FWHM	Full Width at Half Maximum
GC	Galactic Centre
HB	Horizontal Branch
IBD	Iterative Blind Deconvolution
KLF	K-band Luminosity Function
LR	Lucy-Richardson
ML	Maximum Likelihood
NACO	CONICA/NAOS
NIR	Near Infrared
PSF	Point Spread Function
RC	Red Clump
RIAF	Radiatively Inefficient Accretion Flow
SED	Spectral Energy Distribution
Sgr A*	Sagittarius A*
SSA	Simple Shift-and-Add
WFS	Wave Front Sensor

Danksagung

An dieser Stelle möchte ich mich aufrichtig bei meinem Doktorvater Herrn Prof. Dr. Reinhard Genzel bedanken, der mir die Gelegenheit gab, meine Promotionsarbeit auf einem solch spannenden und bedeutsamem Forschungsgebiet in einer wissenschaftlich fruchtbaren Umgeung anzufertigen. Ich möchte mich bei ihm bedanken, dass seine Tür jederzeit offen stand und er mich mit seinen Ideen und Ratschlägen inspirierte.

Bedanken möchte ich mich ferner herzlichst bei:

Herrn Dr. Wolfgang Baumjohann und Herrn Dr. Rudolf Treumann für ihren Rat und ihre Unterstützung bei der Wahl einer geeigneten Promotionsstelle.

Herrn Dr. Thomas Ott, der mich in der schwierigen Anfangszeit intensiv betreute und mich in die Datenreduktion und Beobachtung einführte und mir stets mit Rat und Tat zur Seite stand.

Herrn Prof. Dr. Andreas Eckart, der mich seit dem Beginn meiner Arbeit als eine Quelle von Kreativität und Rat begleitete und mich das Beobachten und die höheren Weihen der Bildverarbeitung lehrte.

Herrn Dr. William Vacca für viele hilfreiche Diskussionen und Ideen und dafür, dass er mir beigebracht hat, wie man Funktionen fittet.

Meinen Freunden und Kollegen aus der Infrarotgruppe des MPE, welche mich durch Freud und Leid des Doktorandendaseins begleitet haben.

Meinen Eltern und meinen Geschwistern, die mich stets unterstützten und förderten und ohne die ich es nie so weit gebracht hätte.

Und, last not least, meinen Freunden und Geschwistern, durch die mein Leben erst richtig Freude und Spaß macht.

Lebenslauf

Name	Schödel
Vorname	Rainer
Geburtsdatum	8. Oktober 1971
Geburtsort	Burghausen, Deutschland
Familienstand	ledig
Staatsangehörigkeit	deutsch

Schulausbildung

1978 – 1982	Hanns-Kammerer-Schule, Burghausen
1982 – 1989	Kurfürst-Maximilian-Gymnasium, Burghausen
1989 – 1990	Prague High School, Prague, Oklahoma, USA
1990 – 1992	Kurfürst-Maximilian-Gymnasium, Burghausen
Juli 1992	Abitur
1992 – 1993	Zivildienst an der Städtischen Poliklinik, München

Hochschulausbildung

1993 – 1996	Studiengang Geophysik an der Ludwig-Maximilians-Universität, München
1996 – 1997	Studiengang Physik an der Universidad de Sevilla, Sevilla, Spanien
1997 – 2000	Studiengang Geophysik an der Ludwig-Maximilians-Universität, München
1999 – 2000	Diplomarbeit am Max-Planck-Institut für extraterrestrische Physik, Garching: *Ereignisse hoher Flusstranferrate im Schweif der Erdmagnetosphäre*
2000 – 2000	Projektbezogene Mitarbeit im Cluster-Datenzentrum am Max-Planck-Institut für extraterrestrische Physik, Garching
2000 – 2003	Doktorarbeit am Max-Planck-Institut für extraterrestrische Physik, Garching: *High-Resolution Near-Infrared Imaging Observations of the Galactic Centre Stellar Cluster*
seit 2003	Wissenschaftlicher Mitarbeiter am I.Physikalischen Institut der Universität zu Köln

Rainer Schödel